MEDITERRANEAN UNIVERSITY OF REGGIO CALABRIA
UNIVERSITY OF MESSINA
DEPARTMENT OF ENGINEERING
DOCTORAL PROGRAM IN
"INGEGNERIA CIVILE, AMBIENTALE E DELLA SICUREZZA"

Curriculum:

SCIENZE E TECNOLOGIE, MATERIALI, ENERGIA E SISTEMI COMPLESSI PER IL CALCOLO DISTRIBUITO E LE RETI

MICROWAVE RADARS FOR SHORT-RANGE APPLICATIONS: FROM THE TRANSISTOR CHARACTERIZATION TO THE SYSTEM DEVELOPMENT

Doctoral Dissertation of:

Emanuele Cardillo

Supervisor:

Prof. Alina Caddemi

The Chair of the Doctoral Program:

Prof. Felice Arena

2016/2017 – XXX Cycle

Contents

Acknowledgements

I would like to express my sincere gratitude to my advisor Prof. Alina Caddemi, for giving me the opportunity of working in the Microwave Electronic laboratory, for her motivation, knowledge and experience not only in the microwave field but in the side activities too.

A special thank is due to Dr. Giuseppe Salvo and Prof. Giovanni Crupi for their help and stimulating discussions, as well as to Prof. Salvatore Patanè for his fundamental contribution in the experimental part of this work concerning the optoelectronic setup.

Last but not least, I would like to thank my family for supporting me throughout my Ph.D. course and for following me in my adventures.

Introduction

The microwave engineering history was likely born with the electromagnetic theory formulated in 1873 by James Clerk Maxwell, whereas one of its first major applications, the radar, was deeply studied and developed during the World War II. During the last decades, the microwave engineering has made a great leap forward due to the increasing number of applications, e.g. satellite communications, wireless and communication systems, radars, environmental remote sensing, cooking of food and medical systems.

The work of this Ph.D. course has been developed within the framework of the research activities of the Microwave Electronics (ELEMIC) laboratory of the University of Messina. As a consequence, the topics treated in this thesis have in common the analysis, design, realization and test of low-noise, high sensitivity microwave components and circuits. The central idea has been that of carrying out a multilayer analysis of a microwave short-range radar. First of all, the radar has been analyzed from a system-level point of view. As well as the main radar applications, technologies and circuital topologies, the research activity has been focused on the improvement of the digital signal processing techniques and on the prototyping and testing methods. In addition, a special application of the radar prototype has been developed with the purpose of enhancing the life quality of visually impaired people.

Thereafter, the problem of noise in radar receivers has been considered and, an in-depth investigation on the noise in microwave transistors has been carried out. GaAs- and GaN- based devices have been characterized not only without optical illumination conditions but also under the special condition of the light exposure. A microwave low-noise amplifier has been designed, realized and tested. Its behavior has been analyzed under light exposure too, for different wavelengths and radiation power levels. Finally, the problem of filtering in microwave receivers has been dealt with and a microwave filter with an extra wide bandwidth has been designed, realized and tested.

The present thesis is organized into three Chapters. In Chapter 1, the micro radar for short-range applications is described along with design and test details. Chapter 2 provides a deep investigation of noise in radar receivers and in Chapter 3 microwave planar filters are analyzed. Finally, the conclusions are drawn and some directions for feasible research developments are proposed.

1 Micro-radars for short-range applications

This Chapter briefly reviews the main radar technologies and architectures. Thereafter, the design, simulation, realization and test of the proposed micro-radar are reported. Moreover, a novel approach for the minimization of crosstalk between the radar transmitter and receiver and a special application in the social context are presented.

1.1 Radar basics and technologies

During the last decades, radar systems have made a great leap forward, tremendously evolving their functions. Although the RADAR acronym "Radio Detection And Ranging" suggests applications in the field of the target detection and distance computing, modern radars are technologically advanced devices able of tracking, identifying and imaging targets in a limitless number of applications from civilian to military, from short to long range and with dimensions of targets from millimeters to tens of meters. A radar is essentially a system that transmits electromagnetic waves toward an area of interest and eventually receives the signals (echoes) reflected from objects (targets) for acquiring information about them. A typical radar schematic is reported in Fig. 1.1. It can be simpler or more complicated but, basically, it must include a transmitter, one or multiple antennas, a receiver and a signal processing section. The transmitter is responsible for generating the electromagnetic signal, whereas the antenna is the transducer that permits the propagation in the atmosphere and vice versa. In some cases, a circulator can be used for providing the connection between the transmitter and the antenna during the transmission time and between the antenna and the receiver during the receiving time. Moreover, it shields the very sensitive components of the receiver from the transmitted signal, thus improving the isolation. If a unique antenna is used for detecting the signal, the radar configuration is monostatic, otherwise it is bistatic. The target, possibly together with other objects, reradiates the induced electromagnetic field in the space. The unwanted unintentional and intentional reflected signals are called clutter and jamming, respectively. The captured signal is then amplified by a low-noise amplifier, converted into an intermediate frequency (IF) and, after an analog-to-digital conversion, finally processed [1].

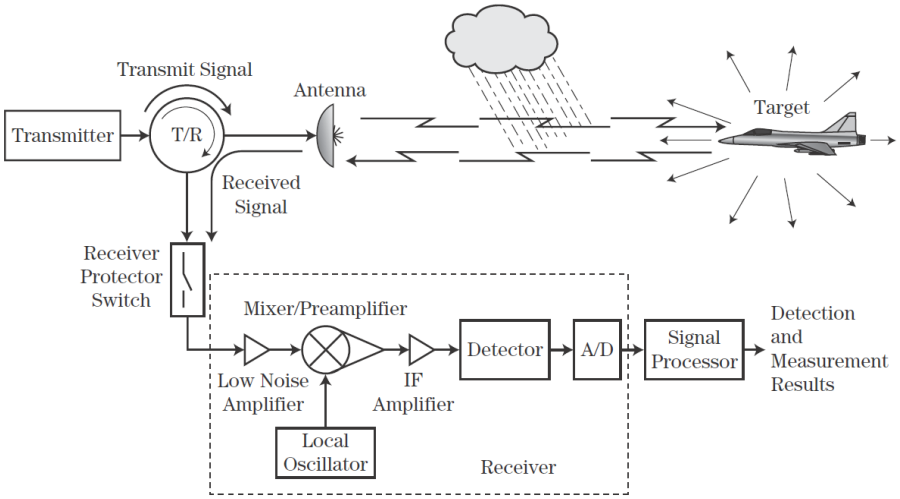

Fig. 1.1: Typical radar schematic [1].

A fundamental radar figure of merit is the maximum detectable range. It depends on several factors, e.g. the radar mode of operation, its characteristic parameters and the properties of the target. The last ones are usually accounted by the radar cross section (RCS) parameter, i.e. a measure of power scattered in a given spatial direction when the target is illuminated by the transmitted signal.

The relationship modelling the amount of received power (P_r) as a function of system specifications and target features is reported in eq. (1.1):

$$P_r = \frac{P_t G_t G_r \lambda^2 \sigma}{(4\pi)^3 R^4 L_s} \tag{1.1}$$

where:

P_t is the peak transmitted power (W);

G_t is the transmitting antenna gain;

G_r is the receiving antenna gain;

λ is the wavelength of the transmitter signal (m);

σ is the radar cross section of the target (m^2);

R is the distance from the radar to the target (m);

L_s is the sum of transmitting, atmospheric, receiving and signal processing losses;

The receiver thermal noise (P_n) is given by eq. (1.2):

$$P_n = kT_0FB \tag{1.2}$$

where:

k is the Boltzmann's constant in watt-per-seconds/Kelvin;

T_0 is the standard temperature in Kelvin;

F is the noise factor;

B is the receiver bandwidth in Hertz;

The minimum detectable signal (MDS) for obtaining the required signal-to-noise ratio (SNR) is given by eq. (1.3):

$$MDS = P_n \cdot SNR = kT_0FB \cdot SNR \tag{1.3}$$

where SNR is the signal-to-noise ratio.

Solving Eq. 1.1 for determining P_r and replacing it with the MDS, it is possible to obtain the maximum detectable range, R_{max}, as shown in eq. (1.4):

$$R_{max} = \frac{P_t\, G_t\, G_r\, \lambda^2\, \sigma}{(4\pi)^3\, L_s\, SNR\, k\, T_0\, F\, B} \tag{1.4}$$

1.1.1 Pulsed and continuous wave radars

Radars can be classified into two categories depending on the transmitted waveform: continuous wave (CW) and pulsed radar.

The formers transmit and receive continuously the signal, usually employing a bistatic configuration.

Since it transmits without interruptions, the determination of the target range is not possible. Consequently, the CW radar is usually employed for detecting the radial velocity of a target. Actually, the range detection is possible with a CW radar by modulating the transmitted signal, as it will be explained in the next section.

If the target is moving, the frequency of the received wave will be different from the frequency of the transmitted one. This effect is commonly known as Doppler Effect and the related Doppler frequency shift f_d is given by eq. (1.5):

$$f_d = \frac{2v_r}{\lambda} \tag{1.5}$$

where v_r is the radial velocity of the target.

The radar takes advantage from the Doppler Effect, calculating the frequency shift and consequently the radial velocity by adopting a homodyne receiver. The inputs of the mixer are the signal of the local oscillator and the received echo. Therefore, the frequency of the intermediate frequency signal, after a low-pass filtering, is exactly equal to the Doppler shift. By properly selecting the main radar parameters it is possible to make feasible the analog-to-digital conversion, thus easily calculating the IF frequency.

The signal transmitted by a pulsed radar is an EM wave with a very short duration, called pulse width (τ) that can range from few nanoseconds to few milliseconds, depending on the application. Usually, during the transmission, the receiver is isolated from the transmitter in order to protect its very sensitive components. Since no echoes can be received during this time, this will affect the minimum detectable range. The pulse width plus the receiving time is called Pulse Repetition Interval (PRI), whereas the number of completed cycles per second is called Pulse Repetition Frequency (PRF). They are related according to eq. (1.6):

$$PRF = \frac{1}{PRI} \tag{1.6}$$

These quantities are illustrated in Fig. 1.2.

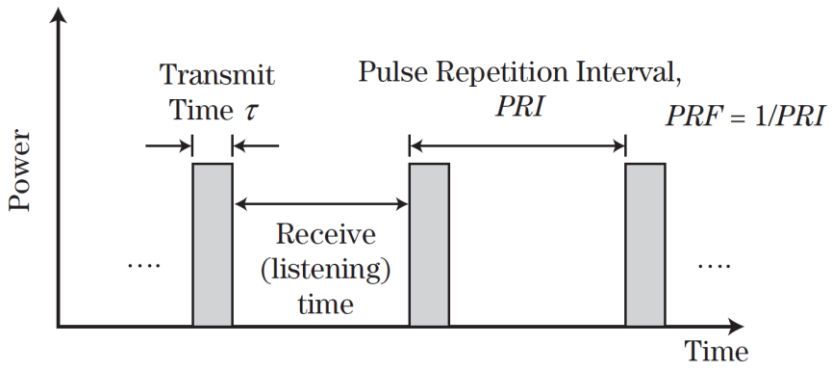

Fig. 1.2: Typical pulsed transmitted waveform [1].

By measuring the time delay (ΔT) between the transmitted and the received signal, the target range can be determined with the well-known relationship expressed in eq. (1.7):

$$R = \frac{\Delta T c}{2} \tag{1.7}$$

where c is the speed of light in vacuum.

Since the radar timing affects the minimum detectable range, it can affect the maximum detectable range in the same way. Indeed, if the pulse round-trip time is greater than the PRI, the echo will not return to the radar before of the next pulse transmission. Therefore, the received signal might be a reflection of the last pulse from a close target, or a reflection of the previous pulse from a distant target, thus resulting in a range ambiguity.

Finally, the spatial resolution δ_R of a pulsed radar can be expressed as reported in eq. (1.8):

$$\delta_R = \frac{\tau c}{2} \tag{1.8}$$

1.1.2 Frequency-modulated continuous-wave radar

For a certain number of applications, the traditional continuous wave and pulsed technologies are not suitable for resolving the target range and/or speed. For instance, the pulse round-trip time for detecting a target placed at the distance of 5 m with a pulsed radar corresponds approximately to 33 ns. Considering Eq. 1.8, the same pulse width must be employed for detecting a farther target with a spatial resolution of 5 meters. This shorter pulse duration would require an expensive and complex transceiver. In addition, shorter pulses have less energy and make the target detection more difficult.

The frequency-modulated continuous-wave radar (FMCW) is a particular radar technology that, even though based on a continuous wave technique, puts a timing mark on the EM wave, thus allowing the target range determination. In addition, the spatial resolution is managed in terms of the frequency modulation bandwidth avoiding the requirement of very short pulses. The FMCW modulation has several advantages:

- ✓ The minimum detectable range is comparable to the transmitted wavelength.
- ✓ The resolution of the range measurement is very high.
- ✓ It allows both target range and radial velocity measurement.
- ✓ The required signal processing architectures are relatively simple.
- ✓ High power pulses are not needed, thus improving safety operations.

The range delay has to be measured indirectly, computing the frequency or phase difference between the transmitted and received signal. Different modulation patterns can be employed depending from the application. Hereafter, the most used saw-tooth and triangular modulation will be analyzed in details.

A typical saw-tooth frequency shape is reported in Fig. 1.3. The time delay of the received signal results in a difference between the transmitted frequency and received one. The frequency difference is called beat frequency and it is a measure of the distance of the reflecting object. If the target is moving, the Doppler shift changes the frequency of the received signal either up or down, for motion directed towards or away from the radar, respectively.

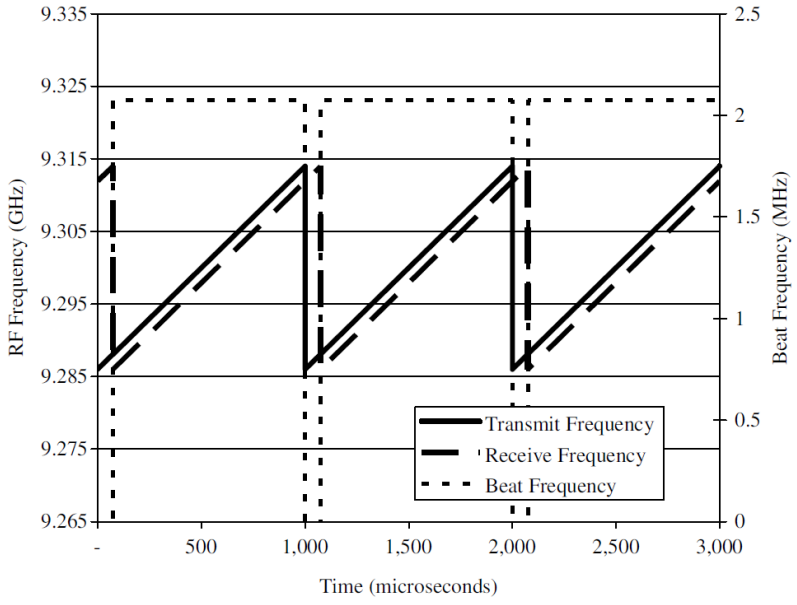

Fig. 1.3: Transmitted (solid line), received (dashed line) and beat (dotted line) frequency waveform vs time [2].

From Fig. 1.3, considering ΔF as the peak-to-peak bandwidth and T_m as the modulation period, it is easy to geometrically establish the relationship expressed in eq. (1.9):

$$\frac{f_b}{\Delta T} = \frac{\Delta F}{T_m} \tag{1.9}$$

where f_b is the beat frequency in Hertz.

By using Eq. 1.7 together with Eq. 1.9, it is possible to relate the beat frequency with the range, as shown in eq. (1.10) [2]:

$$f_b = \frac{\Delta F}{T_m}\frac{2R}{c} \tag{1.10}$$

Clearly, the receiver cannot distinguish between the beat and the Doppler frequency, thus affecting the distance calculation. Anyway, this modulation is considered to be Doppler tolerant, having a negligible influence of the Doppler frequency for several application, e.g. a maritime navigation radar [2], [3]. By considering the characteristics of both the radar and the application proposed in this thesis, the Doppler mismatch will induce very small errors, while preserving the mainlobe and sidelobe structures. Indeed the analyzed targets are almost stationary or they can move very slowly. As stated before, the target resolution can be expressed in terms of the linear frequency modulation range, as reported in eq. (1.11):

$$\delta_R = \frac{c}{2\,\Delta F} \tag{1.11}$$

Coming back to the example at the beginning of this section, for obtaining a resolution of 50 cm, $\Delta F = 300\,MHz$ is required. With a modern radar transceiver, this or even wider linear modulation bandwidths can be easily obtained.

If the separation between the difference frequency ΔF and the Doppler frequency f_d is required, the triangular modulation pattern can be used. The reflected signal is shifted due to the round-trip time. Without a Doppler shift, the frequency difference during the rising edge is the same as the difference during the falling edge.

If a Doppler shift occurs, two different frequencies appear for the rising edge and for the falling edge. Considering the upsweep f_{bUP} and downsweep f_{bDWN} beat frequencies given by eq. (1.12) and eq. (1.13), the range and velocity can be expressed as reported in eq. (1.14) and eq. (1.15), respectively [2]:

$$f_{bUP} = \frac{-\Delta F 2R}{T_m c} + \frac{2v_r}{\lambda} \tag{1.12}$$

$$f_{bDWN} = \frac{\Delta F 2R}{T_m c} + \frac{2v_r}{\lambda} \tag{1.13}$$

$$R = \frac{T_m c}{2\,\Delta F}(f_{bDWN} - f_{bUP}) \tag{1.14}$$

$$v_r = \frac{-\lambda}{4}(f_{bDWN} + f_{bUP}) \tag{1.15}$$

With a triangular-shaped waveform, after a digital signal processing, both an accurate range and velocity determination can be performed. On the other hand, if multiple targets exist, the measured frequencies cannot be uniquely associated with each target, thus leading to ghost targets. With an increased complexity of the transmitter and of the signal processing section, this issue can be overcome by measuring cycles with different slopes.

1.2 Radar subsystems

For an in-depth analysis of the radar subsystems, a more detailed block diagram of a radar is reported in Fig. 1.4. The figure is referred to a pulsed radar, but the following considerations about the main blocks can be considered general.

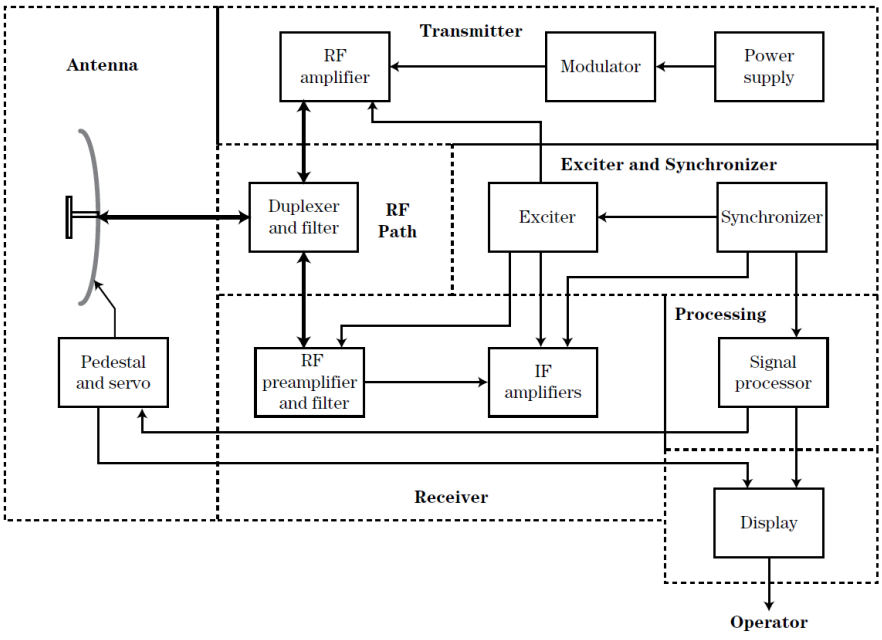

Fig. 1.4: Block diagram of typical pulsed radar [2].

1.2.1 Radar transmitter

The radar transmitter is the subsystem that generates the electromagnetic waves required for illuminating the target. The transmitter's configuration varies depending on the specific application in terms of transmitted signal pattern, power level, timing and technology. Radars can be classified in coherent and non-coherent. The former needs to employ a very stable oscillator for having a well-known phase of the transmitted signal. On the other hand, the latter configuration is less complicated from both hardware and signal processing requirement and consequently much cheaper to implement. Another important choice involves the RF source selection, with two main options based on vacuum tubes or on solid-state devices.

The general trend is to replace the vacuum tube-based RF sources with solid-state devices because of the potentially higher performance, reliability, maintenance costs and smaller dimensions of the last ones. Obviously, there are many applications where solid-state devices cannot compete with vacuum tube devices in terms of output power, efficiency and cost, e.g. when hundreds of kilowatts of average power are required. Finally, modern radars require the modulation of the RF signal, e.g. for FMCW or pulse compression techniques, together with a proper selection of a suitable power supply [4].

1.2.2 Radar antennas

The antenna is the transducer that launches the propagation in the surrounding environment and vice versa. It has a great impact on the radar performance, i.e. only target within the antenna field of view can be detected. The antenna effects on the radar performance are quite clear by observing eq. (1.4) in which the gain terms have a great influence. In Fig. 1.5, the radiation or directivity pattern of an antenna together with some related parameters are shown. One of the most important figure of merit is the 3 dB beamwidth, i.e. the angle between the two -3 dB points on the two sides of the main beam. Moreover, two fundamental parameters are the directivity and the gain. The former is a dimensionless parameter defined as the ratio of the radiation intensity at the main beam peak divided by the radiation intensity of a lossless isotropic antenna with the same radiated power. The latter is defined as the ratio of the radiation intensity at the main beam peak divided by the radiation intensity of a lossless isotropic antenna with the same input power, i.e. the maximum directivity multiplied by the antenna efficiency.

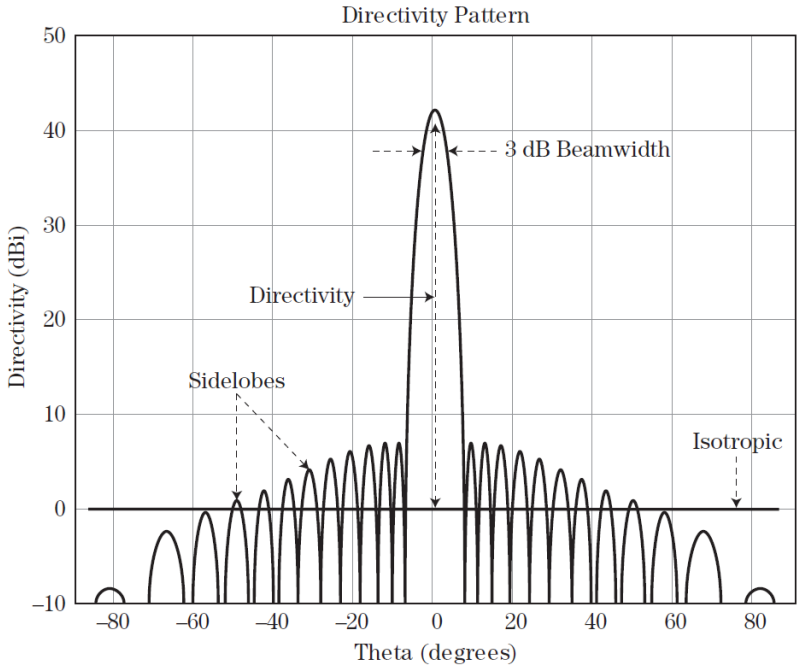

Fig. 1.5: Radiation pattern of an antenna [1].

The last parameter visible in Fig. 15 is the sidelobe level. The average sidelobe level is a very important parameter since strong sidelobes can increase the number of false alarms, for example due to clutter or jamming. The peak sidelobes are usually expressed in dBi (dB relative to an isotropic antenna).

1.2.3 Radar receiver

The echo, after the antenna detection, passes through the receiver section in order to achieve the desired information about the target. One of the receiver features is the capability of protecting its internal sensitive components from the relatively high power of the transmitter. Depending on the technologies, this task can be accomplished by a duplexer, e.g. a circulator eventually with a series protecting switch to disconnect the receiver during the transmission time. Afterwards, an amplification stage is required for increasing the received signal strength together with a low level of noise, which is accomplished by using a low-noise amplifier (LNA).

In addition, a RF preselection is often required for minimizing the exposure to spurious signals, by filtering or eliminating the interferences.

Usually, radars need to convert the received signal into a lower intermediate frequency for detecting or processing the information. The down-conversion process can be accomplished directly with a single stage or with multiple steps, e.g. double down-conversion process. Since for a single down-conversion stage the local oscillator (LO) frequency must be quite close to the high frequency received signal, spurious frequency can appear into the IF signal. Typically, these are due to small differences between the transmitted and the LO frequency or to the appearance of the image frequencies. With the first downconversion stage, the unwanted converted components are further separated from the RF, making it easier to filter them out. Finally, the analog-to-digital conversion is usually performed to perform a digital signal processing.

In designing a radar system, particular attention should be paid to the receiver dynamic range, namely the minimum and maximum signals that the receiver can correctly process. The lower limit is fixed by the noise floor, whereas the upper one is limited by the third-order intermodulation level of the amplifiers and mixers. Since a radar designer has to carefully select each receiver stage, different guides are available in scientific literature [5], [6]. For targeting a suitable dynamic range, two main tools are typically used: the sensitivity time control and the gain control. The former consists of decreasing the sensitivity of the radar for short-range echoes, the latter manually or automatically sets the gain of the receiver for enabling the detection of smaller targets. The last section in a radar receiver, preceding the signal processing stage, is the analog-to-digital data conversion block.

Modern radars employ different receiver configurations: crystal video, superregenerative, homodyne and superheterodyne receiver are the most famous [1]. In the radar system proposed in this thesis, a homodyne receiver has been used whose general schematic is reported in Fig. 1.6. The mixer local oscillator input is represented by a small portion of the transmitted signal. The circulator purpose is to either couple the transmitted signal with the antenna while isolating the receiver, and to couple the received signal with the receiver while isolating the transmitter. The mixer output, after being filtered and amplified, usually already contains the required information about the target.

Another local oscillator is not necessary, thus making this type of receiver simpler to realize and able of providing a coherent signal processing. It is often used for CW and FMCW radars.

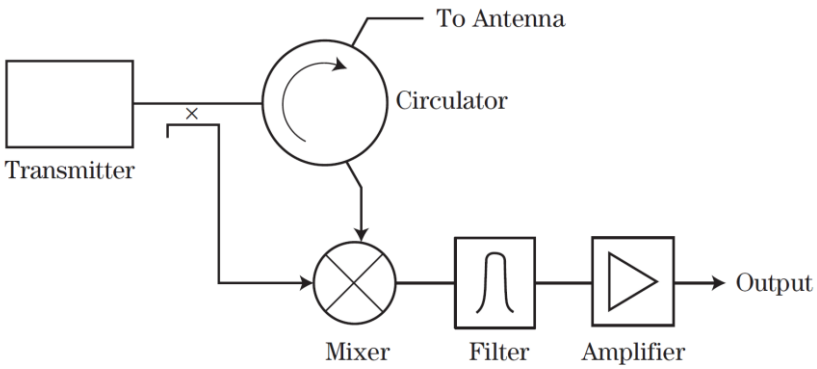

Fig. 1.6: Homodyne receiver schematic [1].

1.3 Threshold for targets detection

The first task of a radar is the target detection that consists in determining if an echo is composed only by an interference or by an interference plus a target. The main criterion for radar detection algorithms usually is the Neyman-Pearson criterion [7]. It is based on two hypotheses:

- ✓ The analyzed signal is only an interference, null hypothesis (H_0).
- ✓ The analyzed signal is an interference plus a target echo (H_1).

Since the combined target plus interference signal is a random process, two probability density functions (PDFs) are required, as reported in eq. (1.16) and eq. (1.17):

$$p_y(y|H_0) = PDF of\ y\ (target\ not\ present) \tag{1.16}$$

$$p_y(y|H_1) = PDF of\ y\ (target\ present) \tag{1.17}$$

The Neyman-Pearson criterion, after fixing the probability of false alarm P_{FA}, is aimed at maximizing the probability of detection P_D, for a given SNR. After reception of the echo, a threshold is computed and the echo level is compared with it. If the signal is beyond the threshold, it is assumed to be the target plus interference, otherwise it is assumed to be the interference only. The verb “assumed” is meaningful because it implies that the decision can

be wrong, leading to a false alarm. Since usually the higher the value of P_D, the higher the value of P_{FA}, a radar designer have to choose the maximum value of P_{FA} that can be tolerated. The decision rule has been synthetized in the likelihood ratio test (LRT), as shown in eq. (1.18) [8]:

$$\Lambda(\mathrm{y}) \underset{H_0}{\overset{H_1}{\gtrless}} T_\Lambda \tag{1.18}$$

where T_Λ is the unknown threshold value, Λ is the likelihood ratio.

and:

$$\Lambda(\mathrm{y}) = \frac{p_y(y|H_1)}{p_y(y|H_0)} \tag{1.19}$$

The likelihood ratio is a random variable with its PDF. Usually, a model for the PDF of the detections statistic (z) under H_0 is determined with the aim of finding the threshold value T so that the probability of y exceeding T is the desired P_{FA}, as expressed in eq. (1.18) [1]:

$$P_{FA} = \int_T^{+\infty} p_z(z|H_0)dz \tag{1.18}$$

These concepts are depicted in Fig. 1.7, where the notional Gaussian PDF of the voltage y under H_0 and H_1 together with the P_{FA} and the P_D are reported.

For improving the system performance in terms of P_D, a radar designer can operate on the antenna design, on the transmitted waveform and power level and on the signal processing technique. The last possibility has been implemented in the work of this thesis and it will be shown in section 1.6.

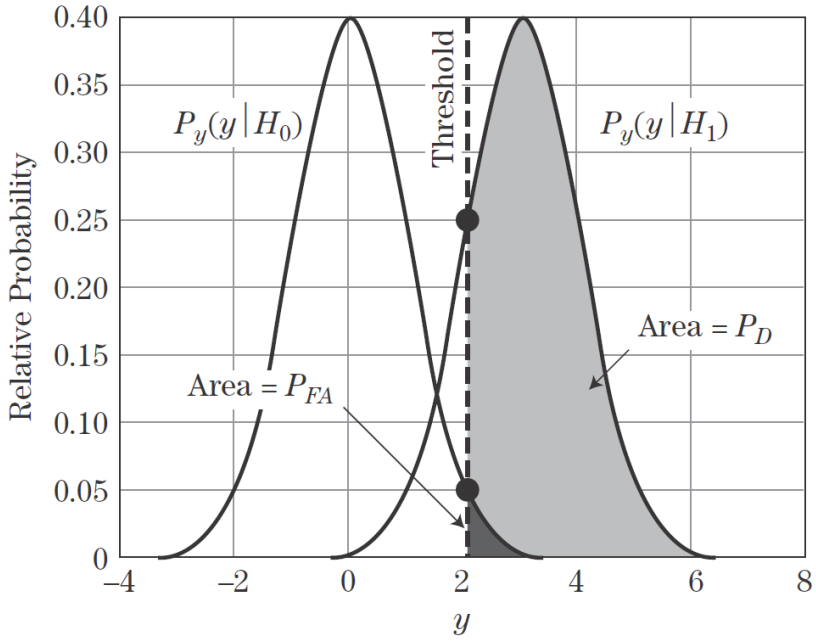

Fig. 1.7: Notional Gaussian PDF of the voltage y under H_0 (left) and H_1 (right), together with the P_{FA} (black) and the P_D (gray plus black) [1].

1.4 Micro-radar for short-range applications

In this thesis, a micro-radar for short-range applications has been designed, realized and tested. The required specifications are:

- ✓ Range resolution: 15 cm;
- ✓ Minimum detectable range: as low as possible;
- ✓ Maximum detectable range: 5 m;
- ✓ Lowest overall dimension;
- ✓ Low consumption;
- ✓ Low price.

For fulfilling these requirements, a frequency-modulated technique has been adopted. The key trade-offs mainly consist of a proper selection of the transmitted frequency, modulation bandwidth, modulation period and beat frequency. The transmitted frequency has been selected in the 24-26 GHz bandwidth, which is typically used in the anti-collision automotive radars, allowing the reduction of the system dimension. The smaller the modulation bandwidth, the

lower the amplitude and the phase noise, whereas a higher modulation bandwidth allows obtaining a finer range resolution, a lower radiated power spectral density and a higher beat frequency.

In addition, by decreasing the modulation period, the beat frequency and the unambiguous velocity and range increase.

Finally, the effects of decreasing the beat frequency are: lower ADC sample frequency; range bin (the bin is the frequency point associated with each result vector element of a FFT) filter with narrower bandwidth; higher phase noise.

A linear saw-tooth signal with a modulation bandwidth of 1.1 GHz, from 24 to 25.1 GHz, has been selected, thus obtaining a spatial resolution of 15 cm. The chirped waveform has been shaped by using a modulating saw-tooth signal with a period of 2 ms. In addition, the transmitted signal has been pulsed, thus reducing the power consumption.

With the aim of achieving both a reasonable dwell time and a limited ON state period of the transmitter, the pulse duration has been chosen equal to 10 ms. Similarly, the pulse repetition time (PRT) has been selected equal to 100 ms, thus obtaining a duty-cycle of 10% that is a good compromise for saving energy and for guaranteeing a comfortable data refresh time.

The transmitted power has been set equal to 11 dBm that allows of obtaining the required maximum range of 5 m. These performances have been obtained by realizing a cost-effective system based on commercially available components and a microwave section based on microstrip technology that allows ease of integration with the antenna section as well as the prototype realization by using in-house facilities.

1.4.1 Design and simulation

For properly analyzing the radar behavior, an equivalent system has been simulated employing the Visual System Simulator™ (VSS) software of the NI AWR Design Environment™ platform. This analysis has been performed at the beginning of this study and the employed parameters are slightly different from the previous ones (frequency bandwidth from 24.5 to 25.5 GHz, PRT of 5 ms and pulse duration of 1 ms) [9]. Anyway, it has been very useful for understanding the main radar characteristics. The schematic of the whole system is reported in Fig. 1.8.

Every target is modelled by means of two blocks. The former reproduces the delay related to the roundtrip path of the wave reflected from the target, the latter adds the white Gaussian noise of the channel and variable losses for different target distances. Typical delays for distances among 1 m and 5 m vary from 6.7 ns to 33.3 ns. The presence of leakage from the transmitter section to the receiver one is also taken into account.

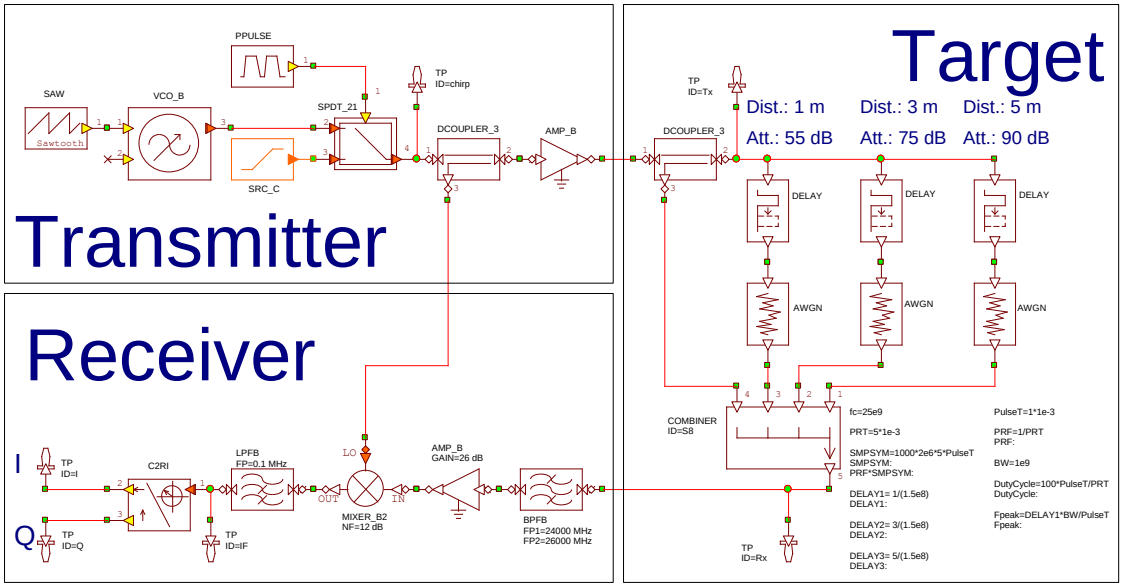

Fig. 1.8: Behavioral radar equivalent system [9].

Power and frequency of the transmitted signal are shown in Fig. 1.9.

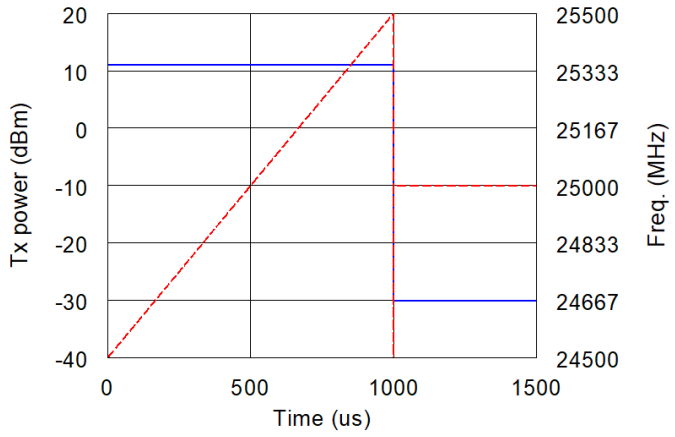

Fig. 1.9: Power (blue solid line) and frequency (red dashed line) of the transmitted signal [9].

In the receiver sections, the reflected signals are filtered, amplified and mixed with a replica of the transmitted ones, thus extracting the in-phase and quadrature components. The overall receiver single-sideband noise figure and gain are respectively 12 and 26 dB. The waveform and the spectrum of the IF signal are both reported in Fig. 1.10.

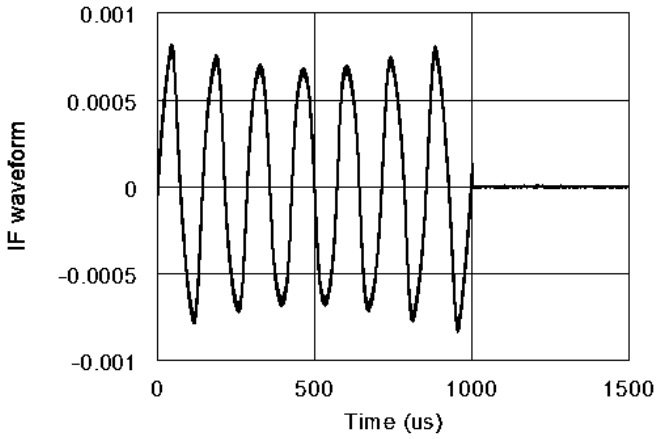

(a)

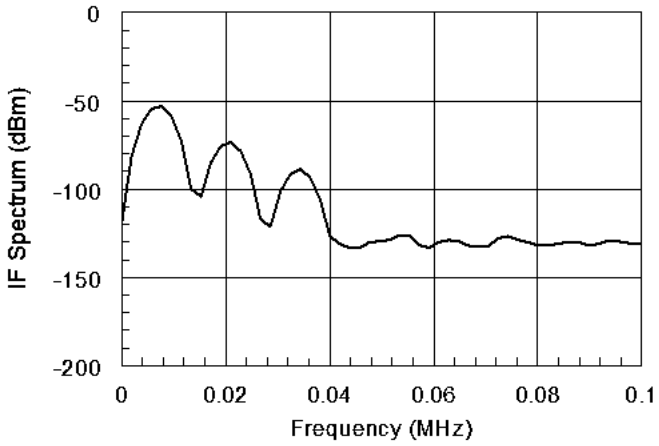

(b)

Fig. 1.10: (a) IF signal waveform and (b) spectrum [9].

The presented approach has been found to be highly flexible for various radar scenarios, by avoiding the typical restrictions due to the crosstalk noise.

1.4.2 Realization and measurements

After the preliminary simulation, the main parameters have been adjusted as described above. The radar prototype employs the BGT24MTR11 integrated circuit as leading block, a SiGe MMIC Transceiver by Infineon Technologies AG [10]. By means of its 24.0 GHz fundamental Voltage Controlled Oscillator (VCO), it can operate from 24.0 to 26.0 GHz, delivering a main RF output power of 11 dBm. The output signal is provided by a differential output. The chip is equipped with an SPI interface, thus allowing to be controlled by a Microcontroller Unit (MCU). Switchable frequency prescalers are included with output frequencies of 1.5 GHz and 23 kHz. A LNA provides low noise figure and a RC polyphase filter (PPF) is used for LO quadrature phase generation of the homodyne quadrature downconversion mixer. The MMIC is packaged in a 32 pin leadless RoHs compliant VQFN package.

The XMC4500 microcontroller by Infineon Technologies AG has been used for driving the system as well as to perform the data processing [11]. The IF signal at the output of the homodyne receiver has been digitized and a fast-Fourier transform (FFT) has been applied. Finally, the peaks exceeding the threshold have been detected and the distance has been computed with the well known equation reported in eq. (1.19):

$$R = \frac{c}{2}\frac{f_b T_m}{\Delta F} \tag{1.19}$$

The simplified scheme of the radar prototype is reported in Fig. 1.11.

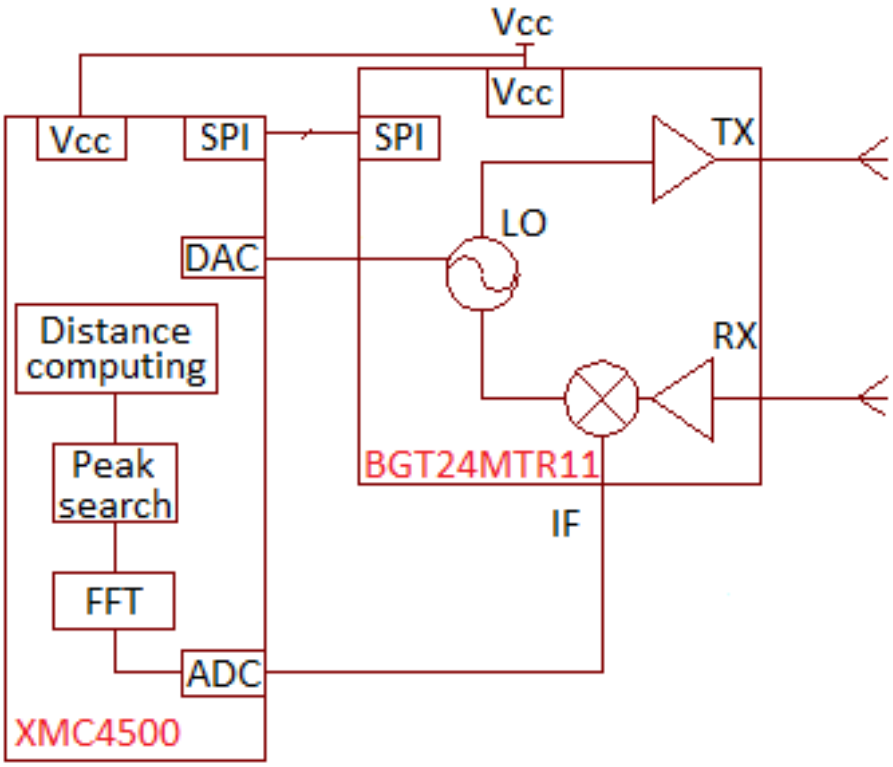

Fig. 1.11: Scheme of the radar prototype.

With the aim of having the Infineon BGT24MTR11 pins accessible, a homemade board has been developed by means of a high precision mechanical plotter (Protomat S103 Plotter), on a Rogers RO4350B substrate. The dimensions of the board are 3.4 cm x 5.2 cm. Afterwards, an Infineon XMC4500 development board has been used in order to drive the entire system and for data processing. Two detailed pictures of the system are reported in Fig. 1.12.

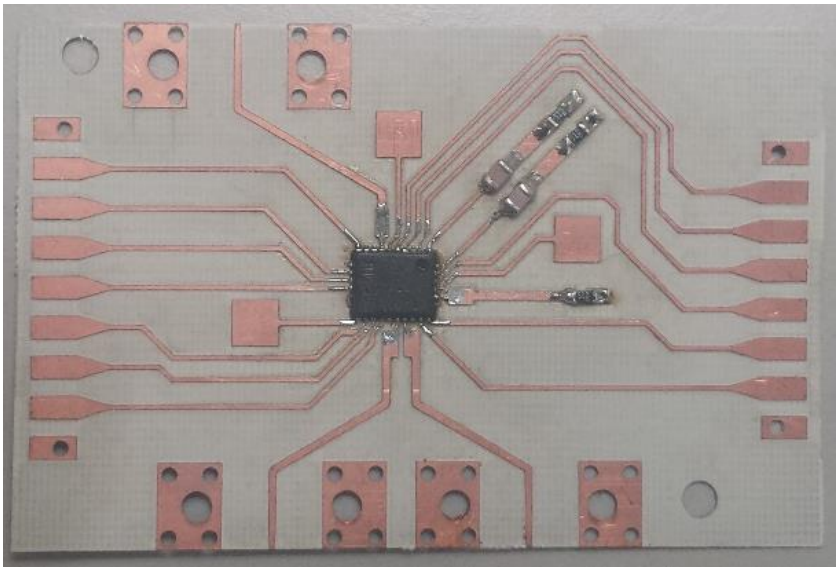

(a)

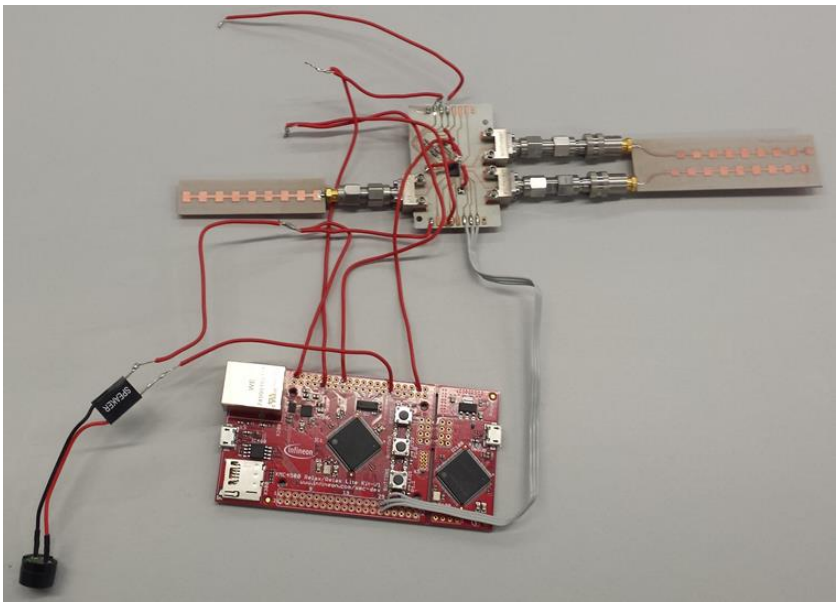

(b)

Fig. 1.12: Photos of the homemade board (a) and of the radar system (b).

For testing the system, two microwave antennas have been designed and realized in collaboration with the Department of Information Engineering, Università Politecnica delle Marche [12].

The transmitting antenna has a balanced input, whereas the receiving antenna has an unbalanced input, according to the transceiver output. More details about the antennas will be given in the last section of this chapter.

To the aim of evaluating the accuracy of the system, different tests have been performed. A metallic cylinder-shaped target (1.75 m height and 7.5 cm diameter) has been employed for performing two measurements at the distance of 1.5 m and 2.5 m. The IF data extracted from the microcontroller and the employed threshold have been reported in Fig. 1.13 for confirming the expected performance. More details about the threshold will be given in Section 1.5.

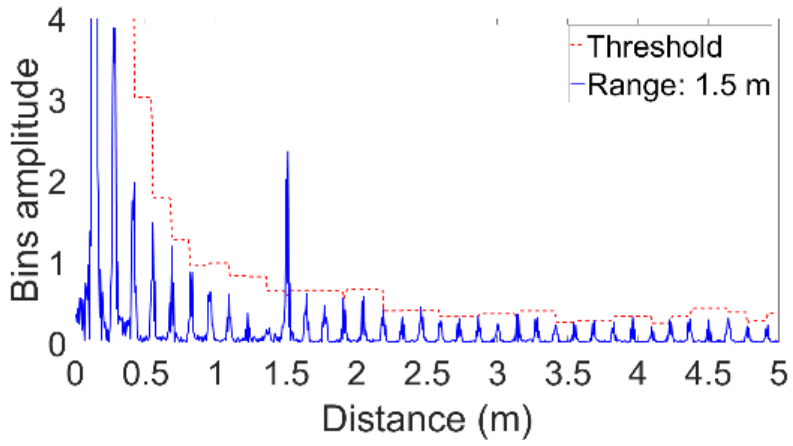

(a)

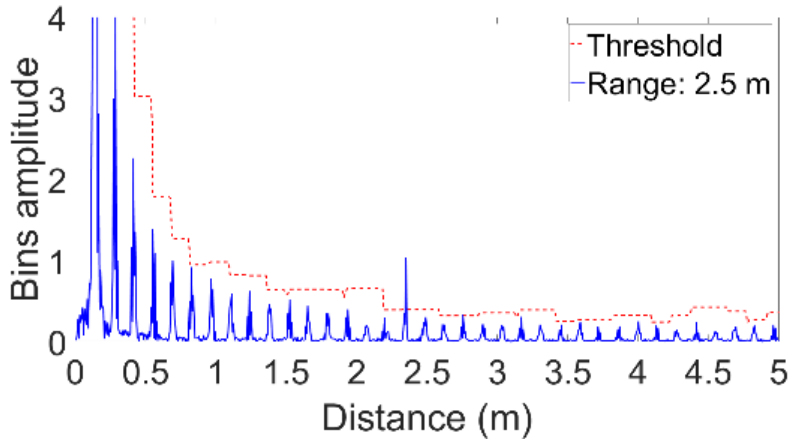

(b)

Fig. 1.13: IF signal (blue solid line) and threshold (red dashed line) for a target at (a) 1.5 m and (b) 2.5 m.

The distinctive feature of the present system is certainly the feasibility of being adapted to several short-range applications. This task can be accomplished by taking into consideration its compactness and cost-effectiveness, without affecting its performance. As a final step, a single board could be realized, thus reducing the overall dimensions.

1.4.3 Transmitter linearization

The frequency at the output of the BGT24MTR11 transmitter has been observed to be not linear with respect to the voltage-controlled oscillator's tuning voltage [13]. This leads to a distorted IF signal at the output of the homodyne receiver that worsens the resolution of the radar, as shown in Fig. 1.14 for a target placed at 1.5 m. Ideally, a single target would generate an IF frequency spectrum composed by a single line. If the transmitter is nonlinear, the transmitted signal will contain more than one frequency harmonic and the frequency difference at the output of the mixer will generate a frequency spectrum composed by more than one line.

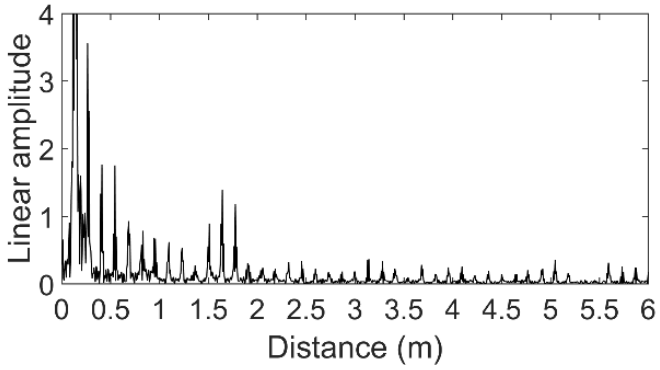

Fig. 1.14: Measured IF for a target placed at 1.5 m, without transmitter predistortion [14].

To the aim of improving the measurement accuracy, the following predistortion procedure has been implemented. The first step has been the measurement of the frequency of the transmitted signal for different tuning voltages by means of a spectrum analyzer (MXA9020A, Keysight Technologies) and an oscilloscope (TDS 2022B, Tektronix Inc.). Thereafter, the expression of the measured tuning voltage V_m, as a function of the measured frequency $Freq_m$, has been computed by using a fitting quadratic polynomial, reported in eq. (1.20):

$$V_m = 0.165 \cdot {Freq_m}^2 - 7.3791 \cdot Freq_m + 83.2749 \tag{1.20}$$

where $Freq_m$ is in GHz.

Equation (1.20) has been used for computing the tuning voltages required to achieve a frequency-linearized output, just replacing the term $Freq_m$ with a linearly-spaced set of frequencies. These values can be employed in place of the original ones by using the expression of the desired tuning voltage V_{lin}, as a function of the original measured ones. The required expression has been computed by using a fitting quadratic polynomial as shown in eq. (1.21):

$$V_{lin} = 0.3119 \cdot {V_t}^2 - 0.0801 \cdot V_t + 0.8982 \tag{1.21}$$

The above eq. (1.21) has been implemented into the microcontroller firmware for obtaining the desired output frequency whose trend vs time is illustrated in Fig. 1.15, showing evidence of the achieved relevant linearity improvements.

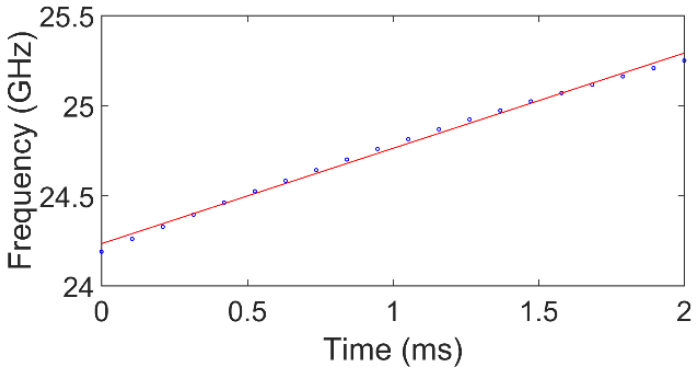

Fig. 1.15: Measured frequencies without (blue) and with (red) predistortion vs time [14].

Finally, the IF signal at the output of the homodyne receiver has been measured again with the same target placed at 1.5m. In Fig. 1.16 the IF signal is shown.

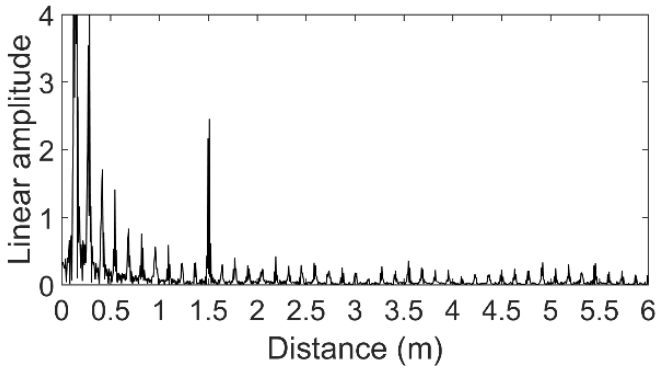

Fig. 1.16: Measured IF for a target placed at 1.5 m, with transmitter predistortion. [14].

The predistortion procedure allows the improvement of the measurement accuracy, thus enhancing the radar performance.

1.5 A novel approach for crosstalk minimization

Pointing towards high performance miniaturized circuitry, one of the main topics in a bidirectional communications system is the coexistence of a very sensitive receiver with a transmitter located in close proximity. The isolation between the components of the system has been extensively investigated by adopting either software or hardware techniques [15-18].

The adopted frequency-modulated radar architecture employs a homodyne receiver which typically is affected by crosstalk issue. This effect can severely worsen the radar performance because it overcomes the intermediate frequency beat and cannot be totally avoided. Otherwise, since it mainly appears in the lower bandwidth part of the IF signal, it could be reduced by means of two classical and well known methods. The first is based upon using a high-pass filter, the second discards the first FFT bins during the signal processing. Both these basic methods degrade the system performance, thus increasing the minimum detectable range. Some sophisticated solutions have been developed for the characterization and mitigation of crosstalk but they often employ expensive or heavy computational procedures and they are aimed at different applications [19-20].

The proposed method has been focused on the identification of the optimal threshold for detecting the target in presence of crosstalk, whose preliminary results are reported in [21]. In literature, it is common to find examples of radars employing an adaptive threshold, e.g., constant false alarm rate detectors. In these systems, the threshold is adjusted to the local interference level assuming that the noise level is homogeneous. By contrast, the present procedure takes in consideration that the cross-talk evolution is not casual. Indeed, once the radar architecture is defined, both the crosstalk and the signal at the output of the homodyne receiver decrease as the frequency increases [10]. Therefore, it is worthwhile employing a higher threshold in the low-frequency bandwidth than in the high-frequency one. For this reason, the first step of this approach has been the crosstalk mapping in absence of targets with the aim of performing a calibration of the receiver threshold. Thereafter, a suitable threshold for every sub-band has been identified according with the cross-talk level. This method aimed at overcoming the crosstalk effects offers two novel features: firstly, it does not require any alteration either in the radar mode of operation or in its hardware. Secondly, it can be employed in different radar applications because the procedure is independent of the architecture and it is not computationally heavy for the processing unit [14].

For evaluating the optimum threshold, the threshold values without any target have been collected. Although the crosstalk trend is quite steady with time, small oscillations of every IF peak have been observed. In order to take these variations in account, the threshold values have been collected over a period of 400 ms. The stored values, increased by a 10% margin, are employed to tailor the required threshold, which is shown in Fig. 1.17.

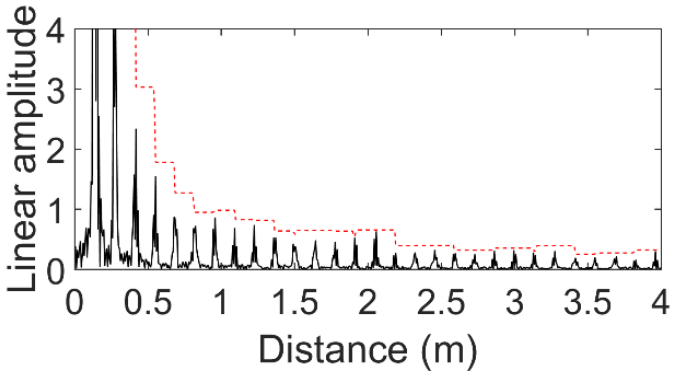

Fig. 1.17: Threshold (red) and IF signal without targets (red) [14].

In Fig. 1.18, the IF signal for a target at different distances has been reported. The system performance is very satisfactory both at shorter distances in presence of a higher crosstalk level, and at longer distances with lower echo strength. By using the proposed approach, the targets have been detected with a reduced computational effort and without discarding any bin.

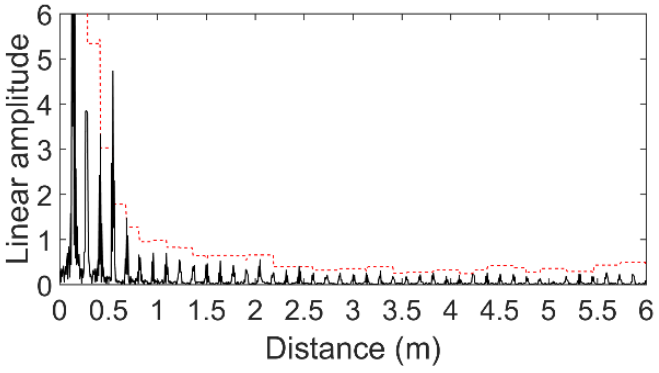

(a)

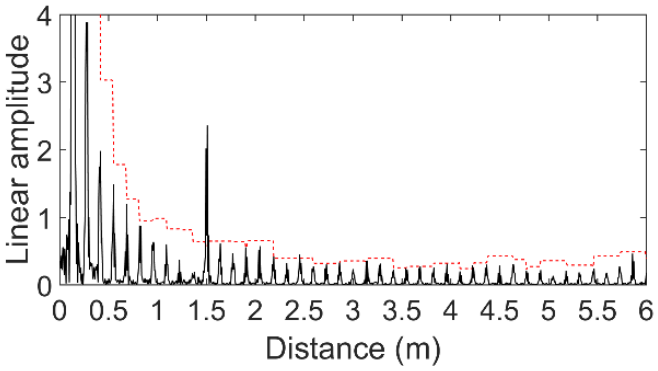

(b)

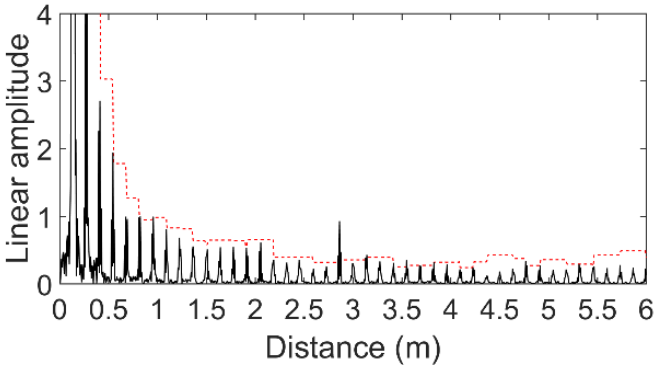

(c)

Fig. 1.18: Threshold (red) and IF signal (black): (a) target at 0.5 m, (b) 1.5 m, (c) 3 m [14].

The presented approach has been found to be highly flexible for various radar scenarios, thus avoiding the typical restrictions due to the crosstalk noise.

1.6 A special application: a microwave white cane for visually impaired people

As it is well known, people affected by blindness and visual diseases need to use special devices to overcome daily tasks, e.g. moving and navigating around unfamiliar environments. Usually, blind people walk assisted by supports ranging from the traditional white cane to more technological devices, namely Electronic Travel Aids (ETA) [22]. Such systems are mainly based on ultrasonic or optic sensors, whereas the use of the electromagnetic (EM) technologies to develop a support system for visually impaired people is a research topic currently under development [23].

It is generally agreed that neither ultrasonic nor optical ETA's satisfy all the needs of a visually impaired person. The ultrasonic ETA's exhibit a limited operating range due to problems when operating with highly reflective surfaces e.g. smooth surfaces, with a low incidence angle of the beam and when detecting small openings, e.g. a narrow door.

The optical ETA's do not suffer from similar drawbacks, but are affected by a high sensitivity to the natural ambient light or by the dependence on the optical characteristics of the target.

The most recent ETA devices employing an electromagnetic (EM) sensor have been proposed in [24, 25], both showing a 24 GHz frequency modulated continuous wave (FMCW) radar able to detect short-range targets.

In [24], the radar is shown to be successfully usable for different industrial and medical applications. One of these applications regards the possibility of augmenting the reality of visually impaired people by navigating through their daily lives. It is proposed that a radar sensor scans the environment, then the target angle and distance information are collected, evaluated and mapped into the audio space by using virtual 3D audio rendering techniques. A FMCW radar has been used in [25] with the aim of realizing a device to be mounted on a white cane. Great attention has been paid to the antenna design, but no details on the system performances nor evidence of proofs with actual end users have been reported.

In this context, our preliminary studies had previously concerned the comparison between the performances of an EM system and those of the traditional supports [26]. This type of investigation had never been presented in the literature, thus representing a pioneer research activity on the expected advantages coming from the adoption of the EM technology as an aid for visually impaired users. Briefly, such preliminary investigations demonstrated the potential for the EM technology in terms of resolution, efficiency and comfort for the user. Since the very first tests were carried out by using laboratory instrumentation, hereby the attention has been focused on the realization of a cost-effective compact radar system characterized by a suitable performance.

The main idea is to realize a device small enough to be attached onto the white cane to enhance the usefulness of a traditional and widely accepted travel aid [27, 9]. As a matter of fact, when realizing a novel support for disable people, it is important not to forget the personal considerations and impressions of end users. The positive reception of a new device within the blind community is a very critical issue. Most requirements concern aesthetics characteristics and appearance: they should be unobtrusive, unnoticeable and easy to carry [28]. For such

reasons a small and user-friendly component integrated onto the white cane, the most widely used and accepted system, has been designed in order to make the user more confident and eager to try the new technology.

As stated above, two microwave antennas have been designed, realized and characterized in collaboration with the Department of Information Engineering, Università Politecnica delle Marche.

The system works as a short-range radar and has to satisfy the following requirements, arising from the specific and innovative type of application:

1. small dimensions and reduced weight, to preserve the user's comfort and to promote the acceptability of a new device;
2. working frequency inside the free-use band for short-range radar applications as defined by the national and international regulations [29]. A resolution of about 10-20 cm is required, which implies a frequency bandwidth of about 1 GHz;
3. radiation pattern shaped as a vertical fan beam, narrow over the horizontal plane ($\leq 10°$) and wide over the vertical one (about 40°), as schematically depicted in Fig. 1.19. Over the azimuthal plane, the direction of the obstacle is detected by scanning the environment with the classical horizontal motion of the cane. This scenario has been described in Fig. 1.19a. Over the elevation plane, as shown in Fig. 1.19b, the wide beam allows even the detection of suspended obstacles, e.g. the branch of a tree;
4. observation range from 1 m to 5 m. Such limits have been arbitrarily chosen according to the end user needs. Indeed, the radar is designed to be mounted on the white cane, which efficiently works for very short distances (< 1 m). The upper limit of 5 m is a tradeoff between the need to efficiently warn the user about the presence of obstacles, and the risk of annoying him with warnings due to very far targets. The system is able of generating a maximum output power of 11 dBm. This value complies with the international regulations regarding the exposure to EM fields [30]. Accordingly, at a distance of 1 m from the antenna (a reasonable minimum distance considering the presence of the white cane) the regulation imposes a maximum E field of 6 V/m, which in this case corresponds to a maximum power of 15 dBm.

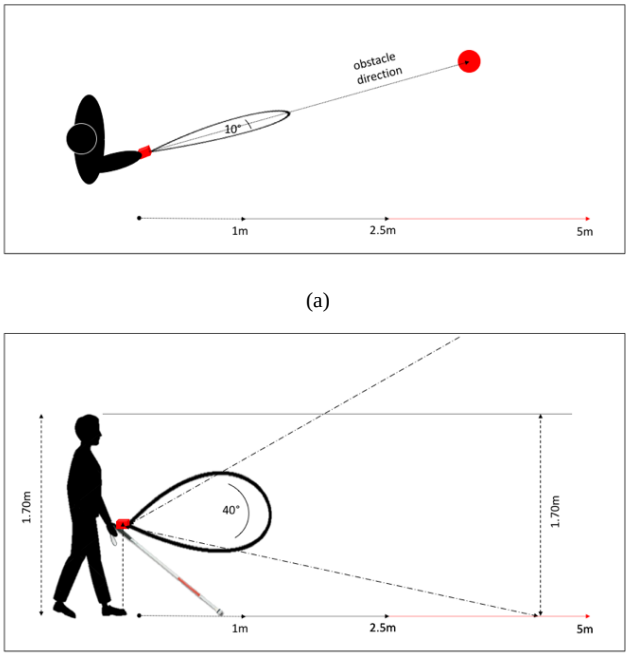

Fig. 1.19: Schematic representation of the EM beam shape due the radar mounted onto a white cane showing (a) top and (b) lateral view [12].

In Fig. 1.20, a picture of the final laboratory prototype, including the radar architecture, the two antennas and all the RF connections, is shown.

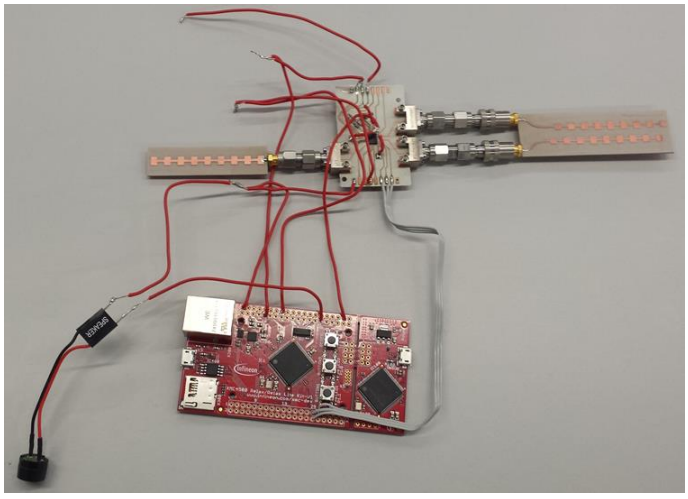

Fig. 1.20: Picture of the radar system including the prototyping board, the MCU board and the two microwave antennas [12].

In order to define the minimum detectable signal, a preliminary measurement without targets has been performed. The poor isolation between transmitter and receiver leads to the crosstalk

noise level, clearly visible in Fig. 1.21. In order to account for this noise level, and hence for the minimum detectable signal, a threshold has been set at twice the level of the crosstalk noise (in order to guarantee a guard level), as highlighted in Fig. 1.21. Each signal measured by the radar system is normalized to the maximum value of such noise and each echo larger than the noise threshold is associated to an obstacle.

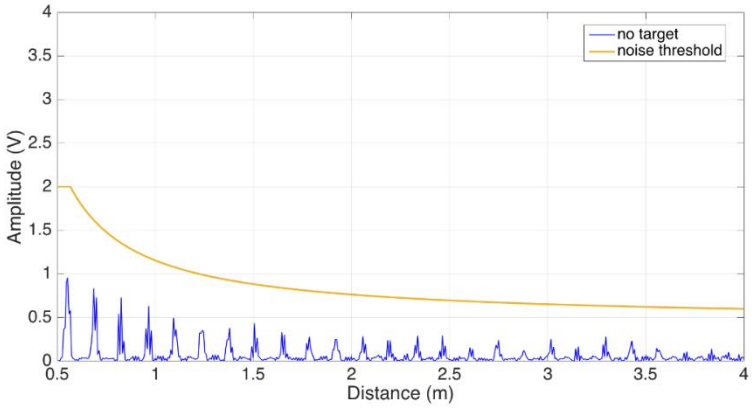

Fig. 1.21: Crosstalk noise caused by the finite isolation between the transmitter and the receiver (blue line) and threshold level (yellow line) [12].

Then, several measurements have been carried out in order to verify the system performance in a real environment, by locating the radar at the height of 1 m from the ground since this is expected to be the final position on the white cane handle.

A cylindric metallic target (1.75 m height and 7.5 cm diameter) has been placed at increasing distances from the radar, ranging from 0.5 m to 3.5 m, as shown in Fig. 1.22. Despite the design requirement, the upper limit is currently limited to 3.5 m because of two main reasons: losses in the microwave connections (around 2 dB) and missing amplification stage at the intermediate frequency in the receiver chain (it will be added to the final prototype).

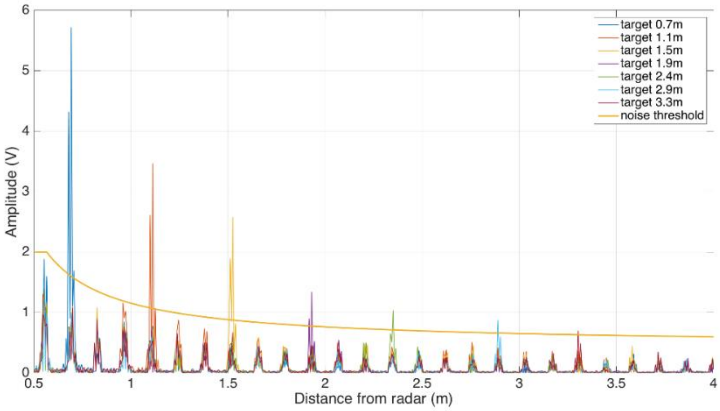

Fig. 1.22: IF signals for target distances from 0.5 to 3.5 m and threshold (yellow line). [12].

Another set of measurements has been performed for confirming the radar capability of detecting targets with a very high horizontal selectivity. The FFT data related to the IF frequency signal have been extracted from the MCU memory. In Fig. 1.23 such data are reported for different angular positions of the target over the horizontal plane, together with the corresponding value of the threshold noise. The same cylindric reflecting obstacle used in the previous tests and located at a distance of 1.5 m from the radar has been used. It is seen that the target can be correctly detected within an angular sector of +/- 3° with respect to the main lobe position, whereas it is almost undetectable at +/- 7° where the signal level is masked by the cross-talk noise. These results confirm the high spatial selectivity of the system.

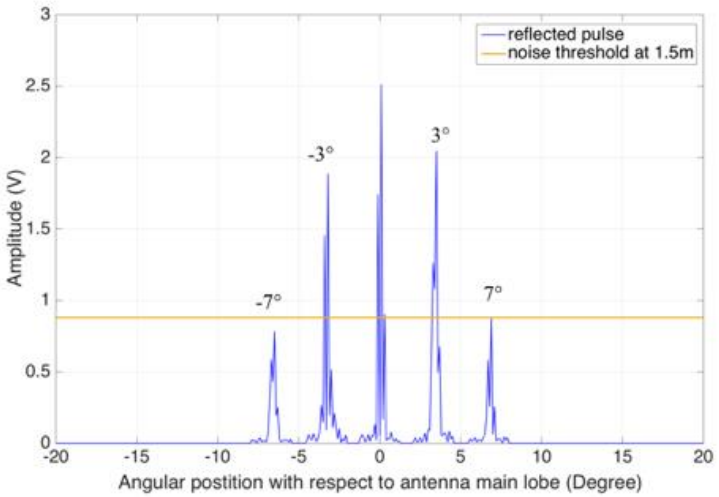

Fig. 1.23: IF amplitude for target horizontal angular position of 0°, +/-3° and +/-7° [12].

Afterwards, the capability of detecting obstacles suspended at different heights with respect to the radar has been tested. The radar has been located one meter above the ground whereas the cylindric obstacle has been moved along different vertical angular positions, according with the design requirements defined in Section II.

Indeed, since using the bare white cane typically allows detection of obstacles lying on (or close to) the ground, it is extremely important to design a device able to protect the user against collisions with obstacles located at different elevations. Once again, a very good performance of the system has been observed since the radar has proven its ability to detect the presence of a suspended obstacle, according to the aperture of the TX radiation pattern. Indeed, the vertical location of the target can be correctly detected within an angular sector of +/- 17°. The related measurement results are shown in Fig. 1.24.

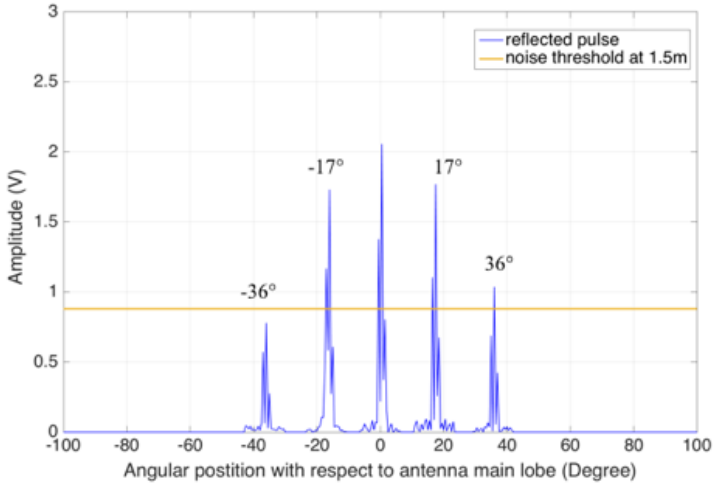

Fig. 1.24: IF signal for target vertical angular position of 0°, +/-17° and +/-36° [12].

The total beam of the radar system is due to the combination of both the TX and the RX radiation patterns. The results presented in Figs. 1.23-1.24 demonstrate that both antennas have been efficiently designed and optimized, because the requirements on azimuthal and elevation apertures are fully satisfied.

Finally, the system capability of detecting obstacles of different shapes, dimensions and materials has been tested, as a preliminary demonstration of the usefulness of such system for daily tasks. In particular, a wooden chair, a chest of drawers and a human subject have been considered. All of them, located at the distance of 1.5 m from the radar have shown to be easily

detectable, since their echoes are sensibly greater than the noise threshold, as shown in Fig. 1.25.

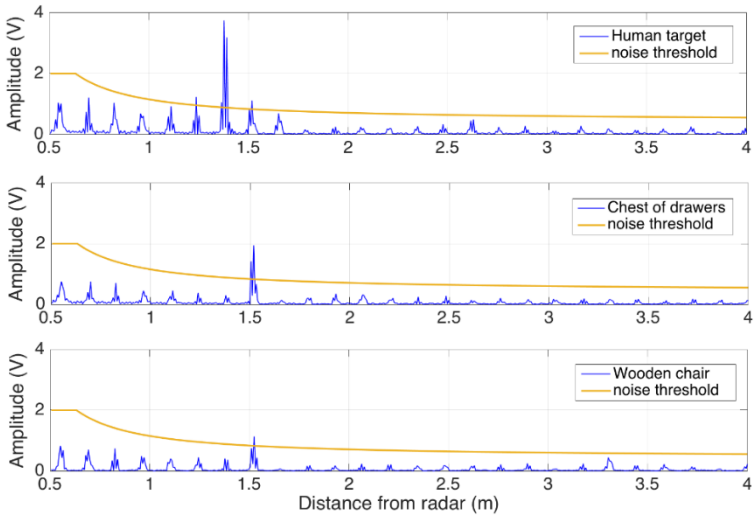

Fig. 1.25: Radar signals for different obstacles located at 1.5 m. From the top to the bottom, a human target, a chest of drawers and a wooden chair are detected [12].

In the case of the chair, the margin with respect to the noise threshold is low. In the final version of the prototype, this aspect will be taken into consideration for obtaining a better signal-to-noise ratio, thus allowing the detection of targets in a wider range.

The topics treated above have been detailed and presented in a paper submitted for publication in Sept. 2017 [12].

1.7 References

[1] M. A. Richards, J. A. Scheer, W. A. Holm, “Principles of Modern Radar: Basic principles,” SciTech Publishing, 2010.

[2] W. L. Melvin, J. A. Scheer, W. A. Holm, “Principles of Modern Radar: Radar applications,” SciTech Publishing, 2014.

[3] Caputi Jr., W.J., “Stretch: A Time-Transformation Technique,” *IEEE Trans. on Aerosp. and Electr. Sys.*, Vol. AES7, Mar. 1971.

[4] M. I. Skolnik, “Introduction to Radar systems,” 3nd ed., McGraw-Hill Co., 2002.

[5] M. I. Skolnik, “Radar Handbook,” 2nd ed., Ed., McGraw-Hill Co., 1990.

[6] Vizmuller, P., “RF Design Guide: Systems, Circuits and Equations,” Artech House, Inc., 1995.

[7] Richards, M.A., “Fundamentals of Radar Signal Processing,” McGraw-Hill, 2005.

[8] Kay, S.M., “Fundamentals of Statistical Signal Processing. Vol. II: Detection Theory,” Prentice-Hall, 1998.

[9] V. Di Mattia, G. Manfredi, A. De Leo, P. Russo, L. Scalise, G. Cerri, A. Caddemi, and E. Cardillo, “A Feasibility Study of a Compact Radar System for Autonomous Walking of Blind People,” *2016 IEEE 2nd International Forum on Research and Technologies for Society and Industry Leveraging a better tomorrow (RTSI)*, Bologna, Sept. 2016.

[10] Infineon BGT24MTR11 datasheet, Rev. 3.1, 2014.

[11] Infineon XMC4500 datasheet, V1.4 2016-01.

[12] E. Cardillo, V. Di Mattia, G. Manfredi, P. Russo, A. De Leo, A. Caddemi, and G. Cerri, “An electromagnetic sensor prototype to assist visually impaired and blind people in autonomous walking,” *IEEE Sensors J.*, Mar. 2018.

[13] Infineon App. Note AN305, User’s guide to BGT24MTR11 24 GHz Radar, rev. 1.0, 2012

[14] E. Cardillo, and A. Caddemi, “A novel approach for crosstalk minimization in FMCW radars,” *Electronics Lett.*, Sept. 2017.

[15] M. Guenach, J. Louveaux, L. Vandendorpe, P. Whiting, J. Maes, and Mi. Peeters, “On signal-to-noise ratio-assisted crosstalk channel estimation in downstream DSL systems,” *IEEE Trans. Signal Process.*, vol. 58, Apr. 2010.

[16] S. A. Bassam, M. Helaoui, and F. M. Ghannouchi, “Crossover digital predistorter for the compensation of crosstalk and nonlinearity in MIMO transmitters,” *IEEE Trans. Microw. Theory Techn.*, Vol. 57, May. 2009.

[17] N. Al-Dhahir, “Transmitter optimization for noisy ISI channels in the presence of crosstalk,” *IEEE Trans. Signal Process.*, vol. 48, Apr. 2000.

[18] A. Hjørungnes, M. L. R. de Campos, and P. S. R. Diniz, "Jointly optimized transmitter and receiver FIR MIMO filters in the presence of near-end crosstalk," *IEEE Trans. Signal Process.*, vol. 53, Apr. 2005.

[19] C. Trampuz, I. E. Lager, M. Simeoni, and L. P. Ligthart, "Experimental characterization of channel crosstalk in interleaved array antennas for FMCW radar," *Proc. 7th European Radar Conference - EuRAD*, Paris, Oct. 2010.

[20] H. Tan, and J. Hong, "Correction of transmit crosstalk in reconstruction of quad-pol data from compact polarimetry data," *IEEE Trans. Geosci. Remote Sens.*, vol. 12, May. 2015.

[21] Caddemi, and E. Cardillo, "A study on dynamic threshold for the crosstalk reduction in frequency-modulated radars," *Computing and Electromagnetics International Workshop (CEM)*, Barcelona, Jun. 2017.

[22] D. Dakopoulos and N. G. Bourbakis, "Wearable Obstacle Avoidance Electronic Travel Aids for Blind: A Survey," *IEEE Trans. on systems, man, and cybernetics—Part c: Applications and reviews*, vol. 40, Jul. 2010.

[23] V. Di Mattia, L. Scalise, V. Petrini, P. Russo, A. De Leo, E. Pallotta, A. Mancini, P. Zingaretti And G. Cerri, "Electromagnetic technology for a new class of electronic travel aids supporting the autonomous mobility of visually impaired people", Chapter Book Entitled "Visually Impaired: Assistive Technologies, Challenges And Coping Strategies" Nova Science Publishers, Inc. 2016.

[24] S. Jardak, T. Kiuru, M. Metso, P. Pursula, J. Häkli, M. Hirvonen, S. Ahmed, M. Alouini "Detection and localization of multiple short range targets using FMCW radar signal," *2016 Global Symposium on Millimeter Waves (GSMM) & ESA Workshop on Millimetre-Wave Technology and Applications*, Espoo, 2016.

[25] S. Pisa, E. Pittella, and E. Piuzzi, "Serial Patch Array Antenna for an FMCW Radar Housed in a White Cane," *International Journal of Antennas and Propagation*, vol. 2016, Article ID 9458609, 2016.

[26] L. Scalise, V. Primiani, P. Russo, D. Shauh, V. Di Mattia, A. De Leo, G. Cerri "Experimental investigation of electromagnetic obstacle detection for visually impaired

users: a comparison with ultrasonic system", *IEEE Trans. Instrum. Meas.*, vol. 61, Nov. 2012.

[27] V. Di Mattia, V. Petrini, M. Pieralisi, G. Manfredi, A. De Leo, P. Russo, L. Scalise, G. Cerri. "A K-band miniaturized antenna for safe mobility of visually impaired people," *IEEE 15th Mediterranean Microwave Symposium (MMS)*, Lecce 2015.

[28] Hersh, Marion and Johnson, Michael A., Assistive Technology for Visually Impaired and Blind People, Springer-Verlag, London 2008.

[29] Commission Implementing Regulation (EU) No 485/2011 of 18 May 2011, Official Journal of the European Union 133, 20.5.2011.

[30] D.M. 381/98, Sept. 10 1998.

2 Noise in radar receivers

This Chapter begins by describing the origin of noise and its importance in radar receivers. Thereafter, a complete analysis of noise in radar receivers is carried out starting from the basic element, the transistor, to the key component, the LNA. Moreover, both the behavior of the transistor and the LNA are deeply analyzed under light exposure since a part of the research work has been dedicated to this aspect. In addition, a low-noise amplifier has been designed, realized and tested under standard and light conditions.

2.1 Noise

As described in the previous Chapter, the receiver is a critical section of a radar system, as its basic function is to distinguish between signal and noise. The noise is critical for the radar performance because it determines the minimum signal that can be detected. The noise internally generated by a component or by an electron device is produced by the random motion of charges in the material. It can be due to different physical mechanisms, thus leading to various types of noise [1], [2]:

- *Thermal, Johnson* or *Nyquist noise,* due to thermal vibration of bound charges.
- *Shot noise,* due to random fluctuations of charge carriers in an electron tube or solid-state device.
- *Flicker or 1/f noise,* occurs in an electron tube or solid-state device and its power is inversely proportional to the frequency.
- *Plasma noise,* due to the random motion of charges in an ionized gas.
- *Quantum noise,* due to the quantized nature of charge carriers and photons.

The noise produced by a system can be characterized in terms of its noise figure. This parameter was introduced by Harald T. Friis of Bell Laboratories who defined the noise figure F of a network as a measure of the degradation in the signal-to-noise ratio (SNR) occurring between the input and the output network ports [3]. By applying a signal affected by noise to the input of a noiseless network, both the noise and the signal will be amplified or attenuated in the same way, thus the SNR will not change. In the case of a noisy network, the output noise

power will increase more than the signal power, thus reducing the SNR. For measuring this degradation, the noise figure, F is defined as in eq. (2.1):

$$F = \frac{S_i/N_i}{S_o/N_o} \geq 1 \tag{2.1}$$

where S_i and N_i are the input available signal and noise powers, respectively, whereas S_o and N_o are the output available signal and noise powers, respectively. Bearing in mind that the available noise power of a resistor at $T_0 = 290\ K$ is expressed as in eq. (2.2):

$$N_i = kT_0B \tag{2.2}$$

and considering the circuit shown in Fig. 2.1, referred to a noisy network with a gain (G), a bandwidth (B) and an equivalent noise temperature T_e, the noise figure is given by eq. (2.3):

$$F = \frac{S_i}{kT_0B}\frac{kGB(T_0 + T_e)}{GS_i} = 1 + \frac{T_e}{T_0} \geq 1 \tag{2.3}$$

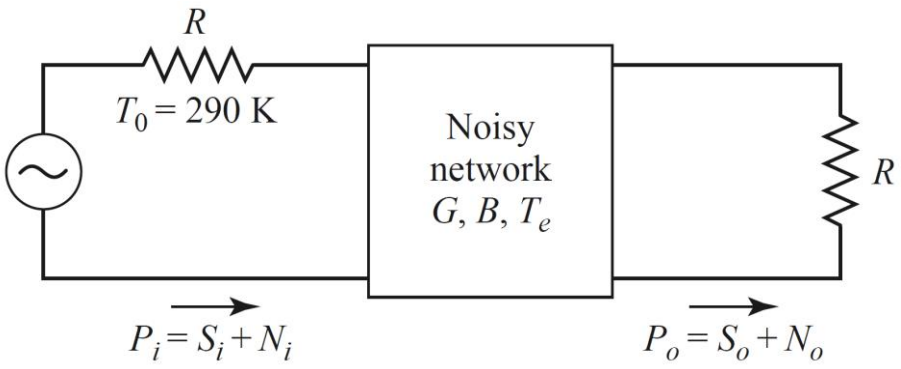

Fig. 2.1: Noisy network [1].

In a typical radar receiver, the received echo passes throughout a series of different stages, each one modifying the signal itself. Given the noise figure and the gain of each stage, it is possible to derive the overall noise figure of the system F_{sys} by using eq. (2.4):

$$F_{sys} = F_1 + \frac{F_2 - 1}{G_1} + \frac{F_3 - 1}{G_1G_2} + \cdots \tag{2.3}$$

Since F_i is the noise figure of the ì-th stage, a clear consequence of eq. (2.4) is that the overall noise figure of the system mainly depends on the first stage. For this reason, usually the LNA is employed as the first active stage of a radar receiver, to amplify the very weak received signal with a minimum additional noise. Besides, passive stages standing between the receiving antenna and the LNA are to be avoided, as much as possible, since their losses (under thermal equilibrium conditions) translate into an additional noise figure value directly added to the chain.

2.2 Noise in microwave transistors

Before analyzing in detail the LNA characteristics, it is worth having a deep insight into the LNA structure. In the following, the active device of the LNA, i.e. the transistor employed, will be analyzed with a special concern to its noise behavior.

In the previous paragraph, the analyzed network has been supposed to be matched to the characteristic impedance at both input and output ports. On the contrary, the typical situation of a microwave transistor within a microwave amplifier is that of a deeply mismatched device, leading to a substantial difference in complexity when compared with the noise performance of a matched one. The noisy network in Fig. 2.1 can be transformed into the network in Fig. 2.2, in which $\overline{|i_s|^2}$ is the mean squared value of the noise current due to the noise source, Y_S is the source admittance, e_n and i_n are the noise sources to be treated as stochastic signals, correlated by means of a complex correlation coefficient.

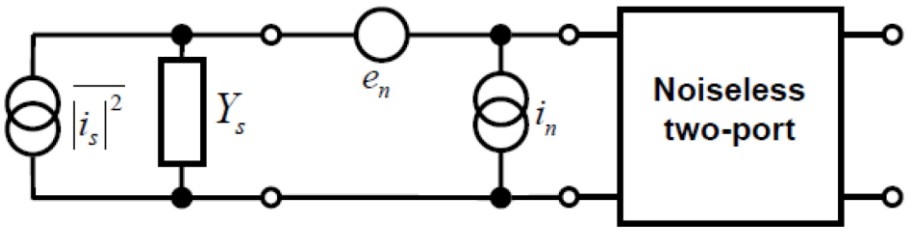

Fig. 2.2: Black-box representation of a noisy network.

As it can be easily demonstrated, the noise figure can be computed by using the expression reported in eq. (2.4), [4]:

$$F = \frac{\overline{|\imath_{tot}|^2}}{\overline{|\imath_s|^2}} \tag{2.4}$$

where $\overline{|\imath_{tot}|^2}$ is the mean squared value of the noise current evaluated at the output of the network with short-circuited terminals.

In real transistors the noise sources are generally correlated, thus a value of source impedance for creating the condition of minimum noise figure exists for each frequency. This concept is essential for understanding the noise parameters. Although these physical noise generators produce noise in both the forward and reverse directions, transistors have gain in one direction, but losses in the other. As a result, the magnitude and phase change in each direction. If there is correlation between the noise sources, then there will be some value of source impedance (Γ_{opt} in eq. (2.5)) that provides the right amount of magnitude and phase shift to cause maximum cancellation, which results in a minimum noise figure.

Finally, it is possible to extract the well-known expression of eq. (2.5) [4]:

$$F = F_{min} + 4\frac{R_n}{Z_0}\frac{\left|\Gamma_s - \Gamma_{opt}\right|^2}{\left|1 - \Gamma_{opt}\right|^2(1 - |\Gamma_s|^2)} \tag{2.5}$$

where:

F_{min} is the minimum noise figure, occurring when $\Gamma_s = \Gamma_{opt}$.

R_n is the noise resistance and represents how fast F degrades as Γ_s moves away from Γ_{opt}.

Z_0 is the characteristic impedance, usually 50 Ω.

Γ_s is the source reflection coefficient.

Γ_{opt} is the optimum noise reflection coefficient, i.e. the value of Γ_s that allows to obtain the minimum noise figure.

The so-called four noise parameters (N-parameters) are F_{min}, magnitude and phase of Γ_{opt}, and R_n [5]. Their knowledge is of basic importance when designing a low-noise amplifier based on highly mismatched devices. They are usually furnished by the manufacturer in the data sheet of the transistor or they can be experimentally determined. A LNA design involves a trade-off between gain, noise figure, VSWR and frequency behavior. The noise parameters strongly depends on the frequency and operating conditions and they can be represented graphically in

different forms [6]. By using a 3-D parabolic-like surface, the role played by each noise parameter can be better understood. A Matlab® script has been used for representing the parabolic-like surface changing different parameters. In Fig. 2.3, a noise surface at a fixed frequency for different values of R_n has been represented, showing that the aperture of the surface decreases as its values increase.

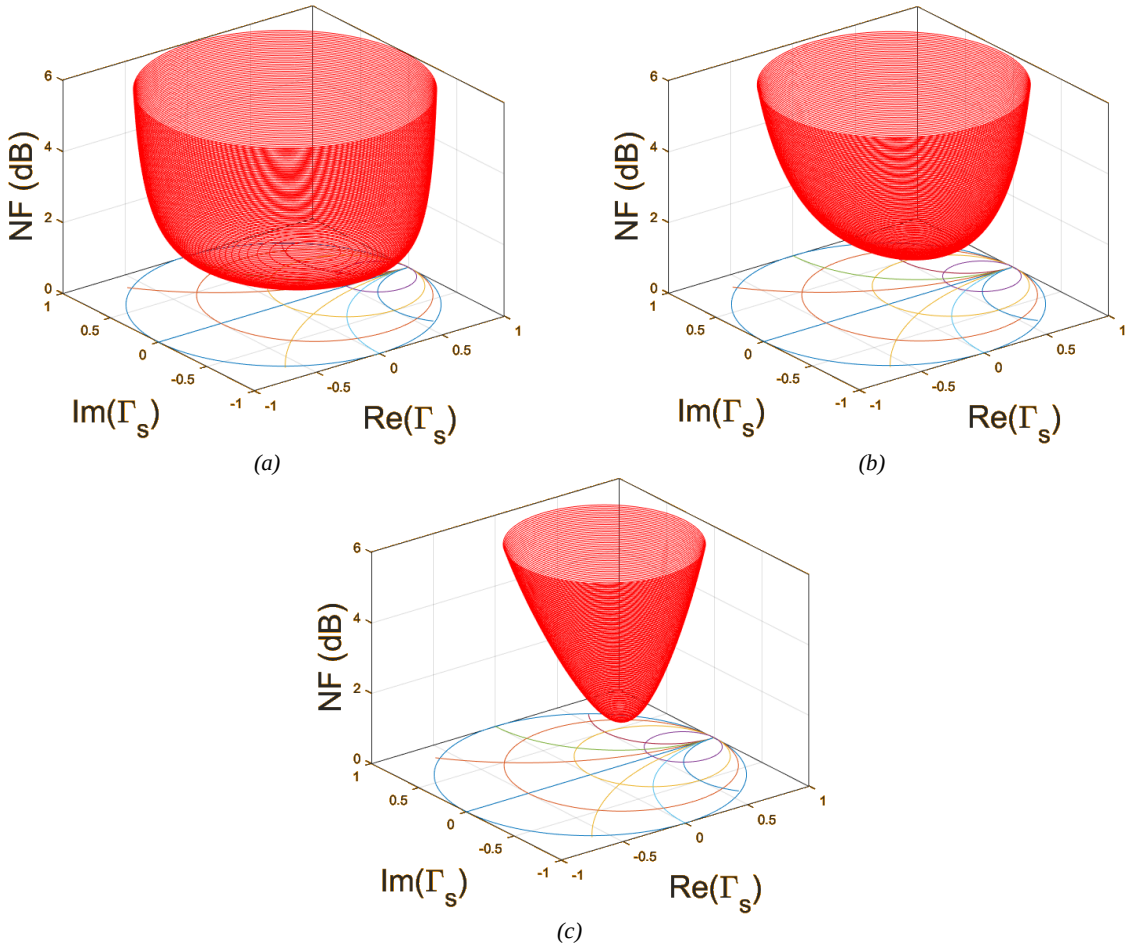

Fig. 2.3: Noise surface for different values of R_n: (a) 5 Ω, (b) 20 Ω, (c) 80 Ω.

In Fig. 2.4, a noise surface at a fixed frequency for different values of F_{min} has been represented. The minimum height increases together with the F_{min} values.

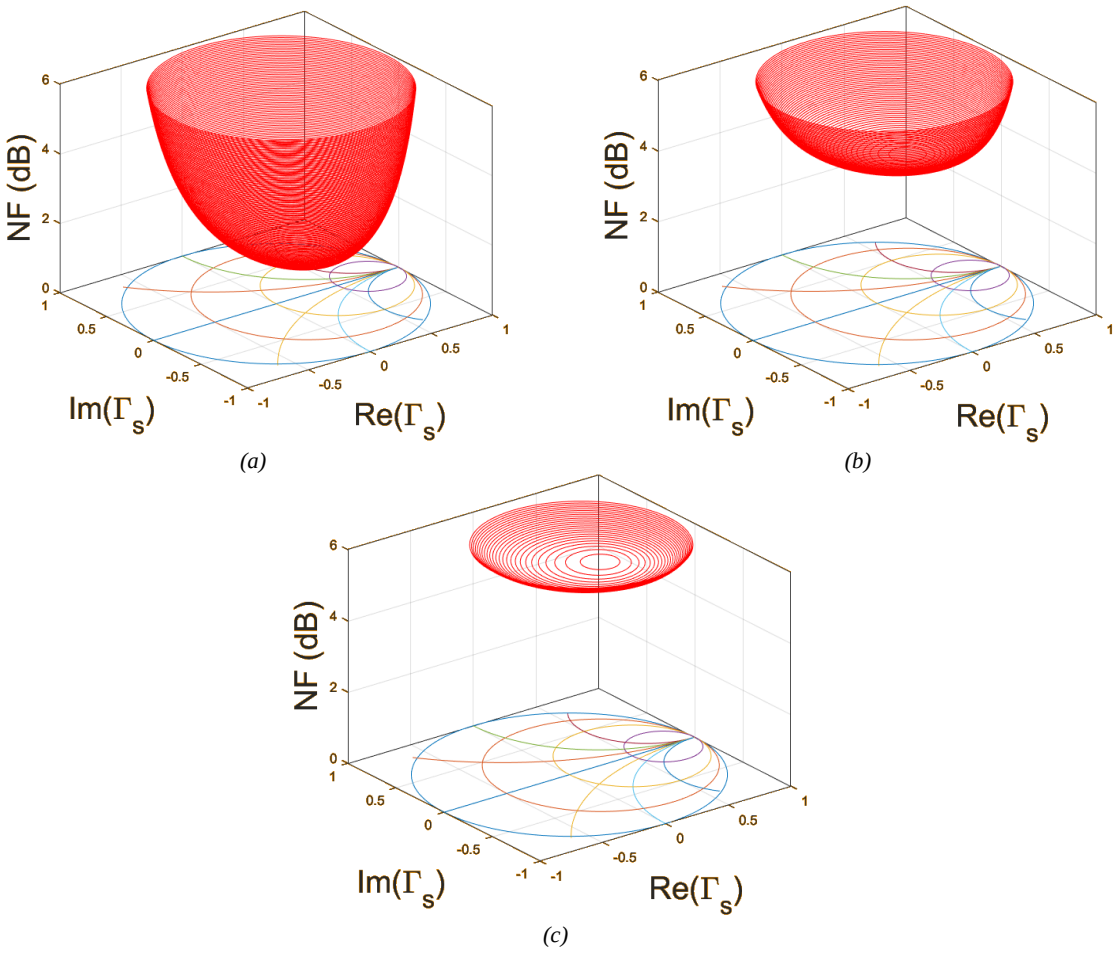

Fig. 2.4: Noise surface for different values of F_{min}: (a) 1 dB, (b) 2 dB, (c) 3 dB.

The procedure for extracting the noise parameters is very complex, in terms of both data processing and hardware set-up, and time-consuming as well. The noise figure of the device under test's (DUT) is masked by the contribution of the measurement chain and the overall accuracy is affected by several factors. The two mainly used measurement techniques are the Y-factor (hot/cold source) and the cold source (direct noise), but the former is predominant especially in commercial systems.

The Y-factor method essentially uses a calibrated noise source that can be turned on and off. A noise figure meter measures the output power in these two states. This amount of extra noise between the on (hot) and off (cold) state is called excess noise ratio (ENR). Typical ENR values vary from 5 dB to 15 dB. After the noise power measurement, the noise figure of the entire system can be computed following the steps reported from eq. (2.6) to eq. (2.9):

$$P_{out,hot} = kBG_a(T_{hot} + T_e) \tag{2.6}$$

$$P_{out,cold} = kBG_a(T_{cold} + T_e) \tag{2.7}$$

where:

$P_{out,hot}$ and $P_{out,cold}$ are the measured output powers in the hot and cold states, respectively;

G_a is the available gain of the system;

T_{hot} and T_{cold} are the temperatures in the hot and cold states, respectively.

$$Y = \frac{P_{out,hot}}{P_{out,cold}} \tag{2.8}$$

where Y is the Y-factor.

$$F = \frac{N_o}{G_a N_i} = 1 + \frac{T_e}{T_0} = 1 + \frac{T_{hot} - YT_{cold}}{(Y-1)T_0} = \frac{ENR}{Y-1} \tag{2.9}$$

where N_o and N_i are the available noise powers at the input and at the output, respectively, and the value of T_{cold} can be assumed to be very close to T_0.

This resulting noise figure is the overall noise figure and it embraces the contribution of all the other parts of the system. Then, eq. (2.10) can be employed for removing the contribution of the stages after the DUT:

$$F_1 = F - \frac{F_2 - 1}{G_1} \tag{2.10}$$

where F_i and G_i are the noise figure and the gain of the i-th stage, respectively. F_2 and G_1 are usually extracted through a calibration step. For computing the four noise parameters, a more complex system is needed to measure different values of the noise figure at various source reflection coefficients. An admittance transformer or a tuner is necessary in order to adjust the values of Γ_s in eq. (2.5). By performing at least four noise figure measurements at different values of Γ_s, it is possible to solve an equation system having four unknowns, i.e. the four noise parameters. Once again, it is important to note that the measured noise figure is not a direct measurement and it suffers from the contribution of all the input and the output stages between which the DUT is embedded. Therefore, for a correct determination of its noise figure, these contributions must be taken into account.

A simplified example of the required evaluation is reported in eq. (2.11):

$$F_m = F + \frac{F_r(\Gamma_{out}) - 1}{G_a} \tag{2.11}$$

where F_m is the measured noise figure, $F_r(\Gamma_{out})$ is the noise figure of the receiver having at its input the mismatched value of reflection coefficient Γ_{out} due to the DUT output.

Before describing the properties of microwave transistors, a brief mention on scattering parameters is required. They consists of transmission and reflection coefficients defined by using matched termination in terms of incident and reflected powers. They are based on the expressions in eq. (2.12) and eq. (2.13):

$$b_1 = S_{11}a_1 + S_{12}a_2 \tag{2.12}$$

$$b_2 = S_{21}a_1 + S_{22}a_2 \tag{2.13}$$

where a_1 and a_2 are the incident travelling voltage waves respectively at port 1 and 2, whereas b_1 and b_2 are the reflected travelling voltage waves respectively at port 1 and 2. This situation is represented in Fig. 2.5.

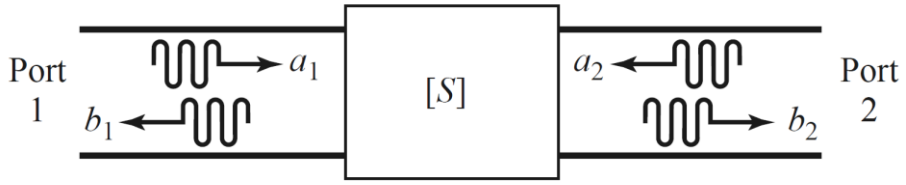

Fig. 2.5: Representation of a two-port network.

Finally, from eq. (2.12) and eq. (2.13), the expression of scattering parameters can be extracted, as reported from eq. (2.14) to eq. (2.17):

$$S_{11} = \left.\frac{b_1}{a_1}\right|_{a_2=0} \tag{2.14}$$

$$S_{22} = \frac{b_2}{a_2}\Big|_{a_1=0} \tag{2.15}$$

$$S_{21} = \frac{b_2}{a_1}\Big|_{a_2=0} \tag{2.16}$$

$$S_{12} = \frac{b_1}{a_2}\Big|_{a_1=0} \tag{2.17}$$

2.2.1 Microwave transistors

The microwave transistors treated in this thesis work belong to the family of high electron mobility transistors (HEMTs) since these devices are widely employed in microwave and millimeter wave applications. A typical HEMT structure consists of a heterojunction between a wide and a narrow bandgap material, as reported in Fig. 2.5. These may be either GaAs based structures employing a heterojunction between gallium aluminum arsenide (GaAlAs) and gallium indium arsenide (GaInAs) or gallium arsenide (GaAs), and GaN based structures presenting a heterojunction between aluminum gallium nitride (AlGaN) and gallium nitride (GaN). The basic structure of a HEMT consists of a heterojunction between AlGaAs and GaAs. Since electron mobility is larger than hole mobility, usually the device is n-channel. The GaAlAs is n-doped, thus electrons diffuse towards the undoped GaAs. In this way, the electric field causes a discontinuity in the conduction band profile shaped as a quasi-triangular well where the carriers are pushed from the doped layer and flow from the source to the drain in a thin sheet. In this way, a 2-D electron gas (2DEG) under the gate, with freedom of motion in the interface plane is formed and carriers flow in a pure crystal material. In addition, for spatially separating the carriers from the donors, a spacer layer is employed, reducing the Coulomb scattering.

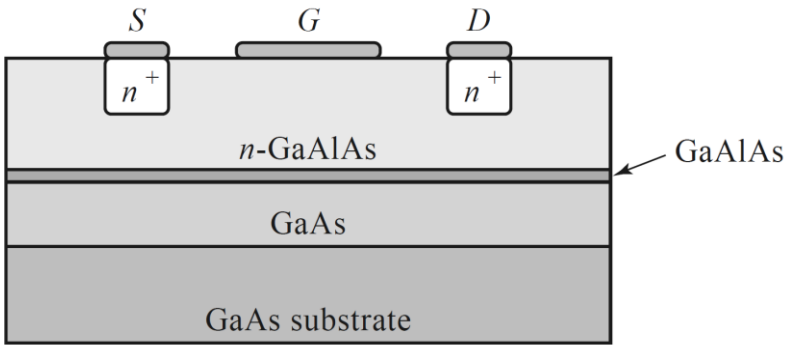

Fig. 2.5: Cross section of an n-channel HEMT [1].

The output current of the device, i.e. the current flowing from drain to source, is modulated by the gate voltage. When the controlling voltage is equal to zero, the channel is open and a current flows. The current can be increased by increasing the gate voltage, whereas it approaches zero when the gate voltage becomes lower than the pinch-off voltage and the 2DEG channel is depleted. One of the key parameters for working with higher power levels is the gate width, e.g. the larger the gate width, the higher the operating power.

One of the limiting parameter for the GaAs HEMTs is the Al concentration, since it should be quite small for minimizing the lattice mismatch at the interface. On the other side, a higher Al concentration would be needed to increase the depth of the quasi-triangular well thus enhancing the confinement of charged carriers within it. To overcome this limitation, the pseudomorphic HEMT (pHEMT) was introduced. It is based on the insertion of an undoped layer of InGaAs between the GaAs and AlGaAs layers. Since the narrow band InGaAs is not lattice matched to the other layers, it has to be so thin that it simply stretches to fit the other material.

The great improvement of the pHEMT consists of a greater carrier confinement due to the larger bandgap differences and the higher carrier mobility, related to the presence of Indium. The GaAs HEMTs or pHEMTs show top performance especially when a very low noise level is required. When the application requires high power levels and a high breakdown voltage, a material with a high bandgap energy is required. GaN and SiC have a bandgap energy higher than conventional semiconductors such as Si, GaAs and InP. They have relatively low mobility but very high values for the saturation velocity. In addition, the thermal conductivity of SiC is markedly higher than conventional semiconductors. This parameter is extremely important because it is a measure of the capability of dissipating power away from the device.

2.2.2 Microwave GaAs-based transistors under light exposure

The high maturity level reached by GaAs technology has been fueled by a wide range of applications in the extra-high frequency range as allowed by premium performances obtainable with Schottky-gate field-effect transistors such as MESFET's, HEMT's, pseudomorphic and HEMT's. The basic material characteristics (i.e., electron mobility, saturation velocity, ease of heterojunction formation) are rewarding for low-noise, high gain targets whereas the direct energy gap makes high optical responsivity levels achievable. Thus, optical control of the microwave signal has proven to be a powerful feature of III–V field-effect transistors that can be widely exploited in advanced telecommunication and high-speed computing systems

A typical approach for characterizing the GaAs HEMTs in terms of noise parameters employs an equivalent-circuit representation where an equivalent noise temperature to each resistor of the electrical model is assigned [7-12]. In the scientific literature, a significant interest for the use of GaAs HEMTs in integrated communication systems based on optical control of the microwave signal can be gathered. On the other hand, only limited attention has so far been paid to the characterization of the noise parameters under light exposure [13], [14]. Hereby, a noise model for a GaAs HEMT based on the AlGaAs/GaAs heterojunction has been implemented. The devices have been illuminated by an optical beam with a wavelength in the visible range. It might be absorbed by the undoped GaAs layer and/or by the AlGaAs donor layer thus stimulating a substantial amount of charge generation triggered by the concurrent photoconductive and photovoltaic mechanisms [15], [16].

The equivalent modelling technique is based on the equivalent circuit model extracted by using the cold bias approach and shown in Fig. 2.6 [17-19]. Due to the significant increase of the gate current under light exposure, it has been expanded with two resistances, R_{gsf} and R_{gdf}, placed at the input and feedback of the intrinsic section of the circuit. All the equivalent circuit elements have been straightforwardly and analytically extracted from scattering (S-) parameter measurements. To reproduce the measured noise parameters, an equivalent noise temperature has been assigned to each resistor. The equivalent circuit topology of the intrinsic section has been modified by the introduction of two resistors at the input (gate-to-source) and feedback (gate-to-drain) to take into account the substantial gate current increase under illumination. The equivalent noise temperatures of the resistances R_{gsf}, R_{gdf}, and R_{ds} have been straightforwardly extracted from the low-frequency input and feedback intrinsic admittance parameters. The degradation of the minimum noise figure is more pronounced at lower frequencies as R_{gsf} and

R_{gdf} play a more dominant role at low frequencies, consistently with the fact that their effects affect S-parameter measurements mostly in the low frequency range. On the other hand, the temperatures associated to the other resistances have been set to the ambient temperature.

The device under test has a 0.25 μm gate length and a 100 μm gate width. It presents two gate fingers connected in parallel. As it is well known, this multi-finger layout allows to achieve better noise performance. The N-parameters have been determined according to the standard source-pull procedure, which exploits a noise figure analyzer (Agilent N8975A) to measure the noise figure for at least four different source impedances synthesized by a tuner (Maury MT-983BU01) [20].A solid-state laser has been used for illuminating the device with a continuous wave illumination with a wavelength of 650 nm. The incident power density has been gradually increased to reach a value of about 0.3 $\mu W/\mu m^2$, in order to observe significant optical effects on the microwave noise parameters of the device under test.

The noise equivalent circuit used to model the studied device has been reported in Fig. 2.6.

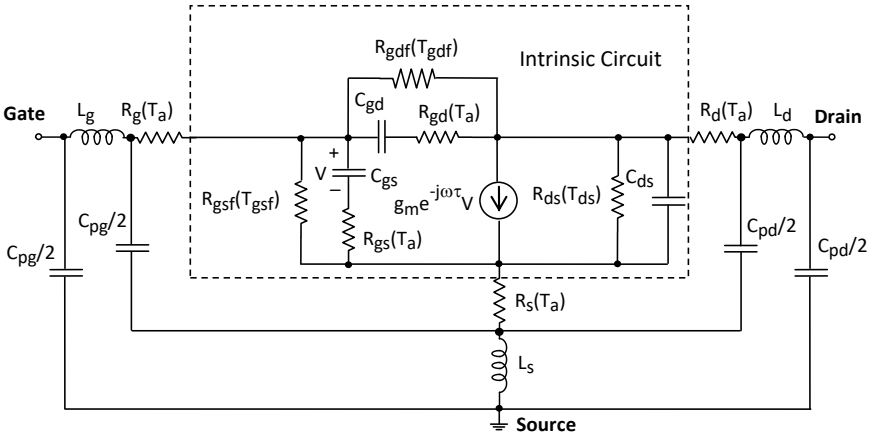

Fig. 2.6: Equivalent circuit noise model for a GaAs HEMT under optical illumination [21].

As shown in Fig. 2.6, the elements of the equivalent circuit can be divided into two main groups: the extrinsic and intrinsic elements. It should be pointed-out that the contributions of R_{gsf} and R_{gdf} have been included only for the model under illumination to take into account for the significant increase of the gate current, while their role is negligible in the case without illumination. The extrinsic elements can be assumed bias-independent and insensitive to the optical illumination [22]. Their values have been extracted from S-parameters performed under cold bias condition (i.e., V_{DS} = 0 V) [19]. Subsequently, the contributions of the extrinsic

elements have been removed from the S-parameter measurements with simple matrix manipulations [23]. Next, R_{gsf} and R_{gdf} have been calculated from the intrinsic admittance (Y-) parameters at low frequencies by assuming that the capacitances behave as open circuits [23], [24]. The expressions have been shown in eqs. (2.18), (2.19):

$$R_{gsf} = \frac{1}{Re(Y_{11} + Y_{12})} \tag{2.18}$$

$$R_{gdf} = \frac{1}{Re(Y_{12})} \tag{2.19}$$

Finally, R_{gsf} and R_{gdf} have been subtracted before calculating the other eight intrinsic elements from the real and imaginary parts of the four Y-parameters with the standard formulas [19]. The noise model has been constructed by assigning an equivalent noise temperature to each resistor. The equivalent noise temperatures of the resistances R_{gsf}, R_{gdf} and R_{ds} have been selected in order to reproduce the noise parameter measurements, whereas the other resistance temperatures have been set equal to the ambient temperature.

The values of the extracted intrinsic elements and the equivalent noise temperatures of the resistances R_{gsf}, R_{gdf}, and R_{ds} are reported in Table II.I.

TABLE II.I. Values of the intrinsic circuit elements and equivalent noise temperatures for a GaAs HEMT without and with illumination at V_{DS} = 2.5 V and V_{GS} = -0.6 V [21].

Elements	**Without Illumination**	**With Illumination**
$\mathbf{C_{gs}}$ (fF)	132.5	147.9
$\mathbf{R_{gs}}$ (Ω)	0.3	0.1
$\mathbf{C_{gd}}$ (pF)	17.9	21.0
$\mathbf{R_{gd}}$ (Ω)	17.0	73.2
$\mathbf{g_m}$ (mS)	32.8	40.5
$\boldsymbol{\tau}$ (ps)	1.3	1.1
$\mathbf{R_{ds}}$ (Ω)	744.5	508.6
$\mathbf{T_{Rds}}$ (°C)	7160	7160
$\mathbf{C_{ds}}$ (pF)	146.0	152.1
$\mathbf{R_{gsf}}$ (Ω)	-	5369
$\mathbf{T_{Rgsf}}$ (°C)	-	1000
$\mathbf{R_{gdf}}$ (Ω)	-	28544
$\mathbf{T_{Rgdf}}$ (°C)	-	1000

In agreement with the results reported in [22], g_m and C_{gs} have shown a significant increase under illumination. The equivalent noise temperature of R_{ds} has been selected for reproducing the observed behavior of the noise parameters without illumination. On the other hand, the equivalent noise temperatures of R_{gsf} and R_{gdf} have been chosen to model the measured noise parameters with illumination. The same temperature has been assigned to both the resistances as their temperatures play similar role from a simulation point of view. As illustrated in Figs. 2.7 and 2.8, a good agreement between measured and simulated N-parameters has been achieved for the tested device with and without optical illumination over the broadband frequency range spanning from 2 GHz to 18 GHz. The reported experimental results have shown that the contributions of R_{gsf} and R_{gdf} should be added to reproduce the noise behavior of the tested device in order to model the significant increase of the gate current under optical illumination. More in detail, a clear evidence of this increase of the gate current is given by the fact that the starting point of the optimum source reflection coefficient moves from the open-circuit condition towards lower impedance condition under light exposure.

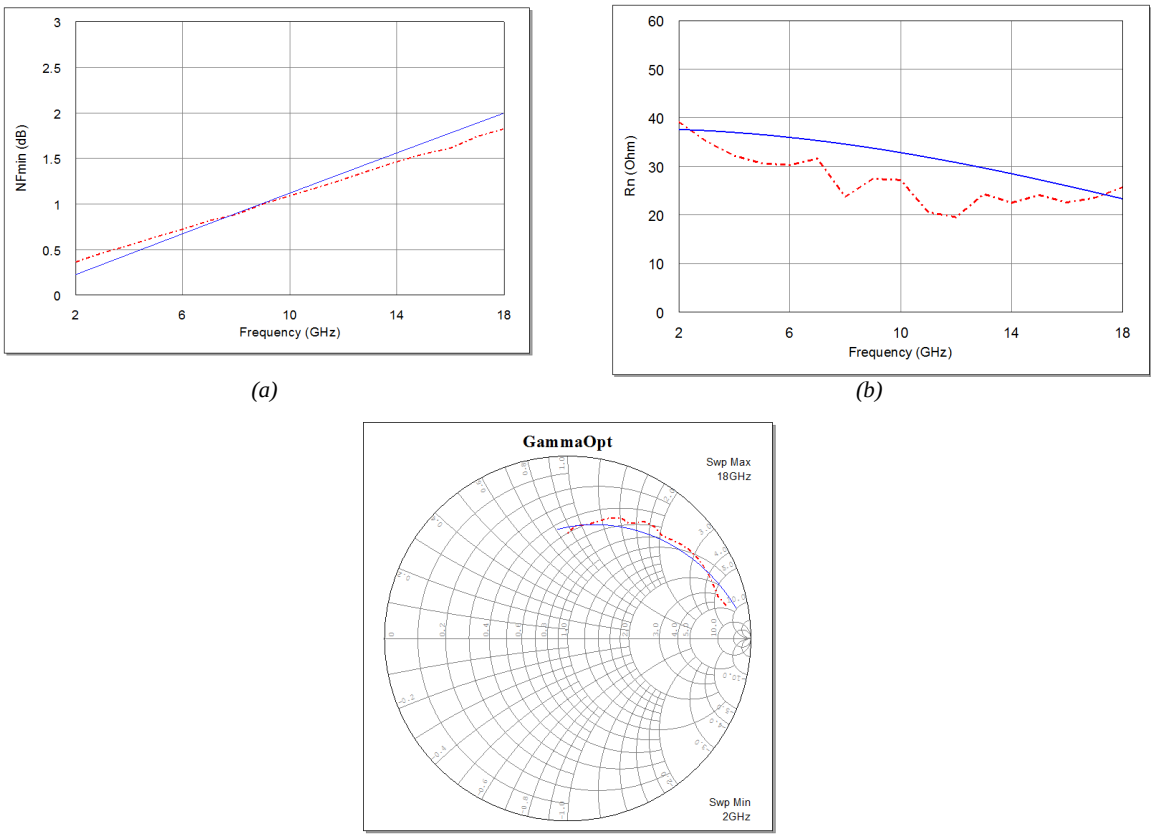

(a) *(b)*

(c)

Fig. 2.7: Simulated (blue solid line) and measured (red dashed line) N-parameters from 2 GHz to 18 GHz for a GaAs HEMT without illumination at V_{DS} = 2.5 V and V_{GS} = -0.6 V: (a) minimum noise figure, (b) equivalent noise resistance, and (c) optimum reflection coefficient [21].

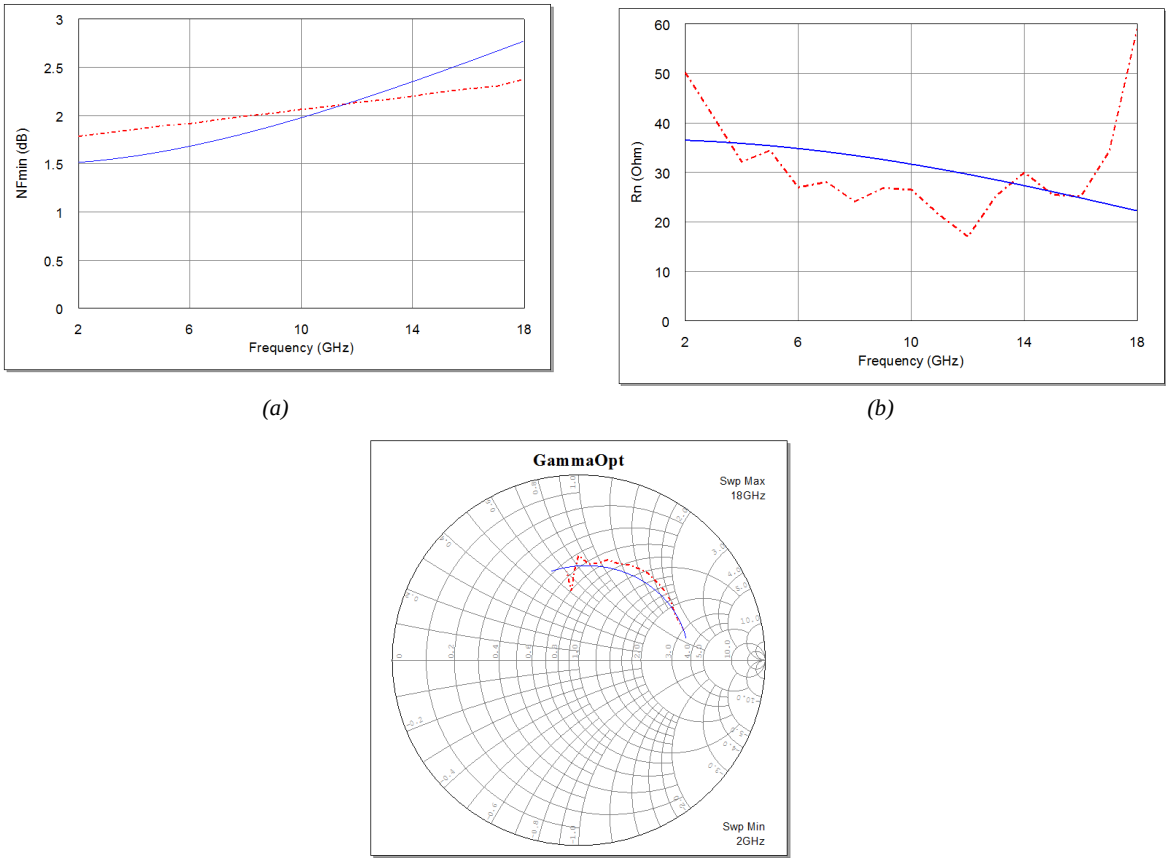

(a) *(b)*

(c)

Fig. 2.8: Simulated (blue solid line) and measured (red dashed line) N-parameters from 2 GHz to 18 GHz for a GaAs HEMT under optical illumination at V_{DS} = 2.5 V and V_{GS} = -0.6 V: (a) minimum noise figure, (b) equivalent noise resistance, and (c) optimum reflection coefficient [21].

As a complement to this study, the origin of the light-activated noise is investigated in terms of the intrinsic noise sources. The light activation of such excess noise has been analyzed by employing the just showed noise temperature circuit model and the analytical noise model based on K_g, K_r and K_c coefficients (hereinafter referred to as KGCR model) [7]-[25].

These three coefficients are directly related with the physics of the device. K_g, shows the strongest increase with drain current. The least dependence on drain current is exhibited by K_c, whereas for short gate lengths, K_r approaches zero.

The noise model formulation based on these coefficients is used to enlighten the key aspects of the optically activated noise on the device performance. It is observed that the origin of the degradation of the minimum noise figure can be attributed in each case to the noise coefficient related to the gate noise source that is strongly affected by the charge generation related to light exposure.

The devices under test are lattice-matched GaAs HEMT's having 0.25 μm gate length and 100-200-300 μm gate widths, whose DC, linear scattering and noise parameters had been previously measured in dark conditions and under CW light exposure at 650 nm. As mentioned above, an accurate circuit model was already extracted and discussed only for the 100 μm gate width device [26]. Following this step, the analysis has been completed by extracting the model for the 200 and 300 μm gate width devices in order to test the noise model accuracy on the whole transistor series whose scalability of the small-signal performance had been deeply investigated in [19]. In addition, a comparative analysis between the performance of the temperature noise model and the KGCR model referred to the core device structure is presented.

The bias conditions of the devices with the gate width of 200 and 300 μm are the same as those employed for the 100 μm gate width device, i.e. V_{DS} = 2.5 V and V_{GS} = -0.6 V. The devices were exposed to the same 650 nm laser radiation and their performance was tested by measuring the DC characteristics and both S- and N- parameters in the 2-18 GHz frequency range in dark condition and under illumination [13], [14].

The N-parameters were determined by implementing the same procedure of the 100 μm device [8].

In reference [14], it could be observed that the light exposure was beneficial to the small-signal performance leading to: a) an increase of the device gain ($|S_{21}|$); b) a decrease of the input and the output return loss ($|S_{11}|$, $|S_{22}|$); c) a decrease of the reverse gain ($|S_{12}|$).

In contrast, the light absorption evidently activated the generation of excess noise in all the devices leading to a remarkable increase of the minimum noise figure, especially at lower frequencies as reported in Fig. 2.9.

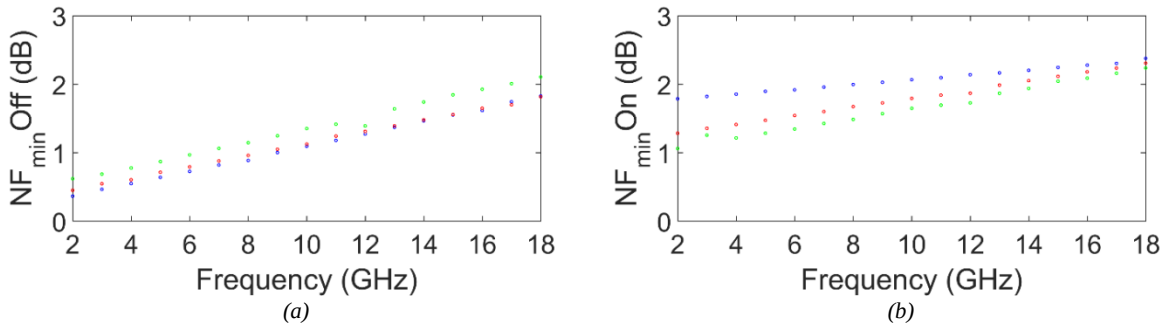

(a) *(b)*

Fig. 2.9: Measurements of NF_{min} of scaled HEMTs at V_{GS} = -0.6 V and V_{DS} = 2.5 V with three different gate widths of 100 um (blue circles), 200 um (red circles), and 300 um (green circles): (a) without light and (b) under light exposure [25].

The noise resistance typically exhibited a slight increase and the magnitude of the optimum source reflection coefficient was sensibly reduced. These effects were further confirmed in other experimental investigations on different devices and they were found to be consistent with an increase of the gate current under illumination [14].

To develop this analysis, a circuit model was then determined for each device by using the measured scattering parameters both in dark and under exposure conditions, according to the procedure employed for the 100 μm device [17].

Once the models were extracted, the noise correlation matrix of the intrinsic circuit under dark and light exposure could be straightforwardly determined by circuit analysis performed with Microwave Office® by NI AWR Design Environment™. All the element and temperature values of the three models are reported in Tab. II.II.

TABLE II.II Values of Id and the equivalent circuit elements for three HEMT's with different gate width under dark and light exposed condition [27].

W (μm)	***100***		***200***		***300***	
Element	*Dark*	*Light*	*Dark*	*Light*	*Dark*	*Light*
I_d **(mA)**	10.0	15.3	20.3	27.1	33.2	39.7
C_{gs} *(fF)*	132.5	147.9	203.0	224.3	299.3	317.7
R_{gs} *(Ω)*	0.3	0.1	0.1	0.1	0.1	0.1
C_{gd} *(fF)*	17.9	21.0	26.1	28.7	35.2	36.1
R_{gd} *(Ω)*	17.0	73.2	24.4	51.6	39.9	51.3
g_m *(mS)*	32.80	40.50	63.46	74.51	98.65	108.05
τ *(ps)*	1.3	1.1	1.3	1.2	1.4	1.4
R_{ds} *(Ω)*	744.5	508.6	363.8	314.4	243.4	229.7
T_{Rds} *(℃)*	7160	7160	6500	6500	7500	7500
C_{ds} *(fF)*	146.0	152.1	237.3	242.2	345.5	349.6
R_{gsf} *(Ω)*	-	5369	-	3875	-	10053
T_{Rgsf} *(℃)*	-	1000	-	500	-	700
R_{gdf} *(Ω)*	-	28544	-	31720	-	66950
T_{Rgdf} *(℃)*	-	1000	-	500	-	700
L_g *(pH)*	118.6		107.9		103.9	
R_g *(Ω)*	4.8		4.3		3.6	
L_d *(pH)*	127.7		99.0		103.4	
R_d *(Ω)*	2.0		1.7		1.5	
L_s *(pH)*	11.5		13.0		11.1	
R_s *(Ω)*	0.5		0.4		0.3	
C_{pg}- C_{pd} *(fF)*	15.2		16.6		25.2	

The noise correlation matrix elements in the admittance form are needed to obtain the mean square values of the input and the output noise current sources ($\bar{\imath}^2_g$, $\bar{\imath}^2_d$) as well as the correlation coefficient. The behavior of the intrinsic noise coefficients are indeed of basic importance to understand the origin of the excess noise activated by the light exposure and how the minimum noise figure is affected by this process.

As expected, the drain noise source $\bar{\imath}^2_d$ was independent of the frequency in dark condition whereas the gate noise source $\bar{\imath}^2_g$ exhibited a typical f^2 trend for all devices. Under light exposure, the gate noise was affected by a remarkable increase in the 100 and 200 μm devices and to a more limited extent in the 300 μm device. The drain noise remained almost frequency-independent and exhibited a maximum 50% increase in the smallest device, consistently with the observed increase in I_d.

As reported in Tab. II.II, constant noise temperature values T_{ds} have been assigned both in dark and under light exposure condition. Indeed, this is directly related to the data concerning the drain noise current values extracted from measurements as well as to the fact that most of the drain noise variation is accounted for by the decrease of the drain-source resistor values as obtained from the scattering parameter model extraction step.

The behavior of $\bar{\imath}^2_g$ under light ON-OFF conditions for the three HEMT's is shown in Fig. 2.10.

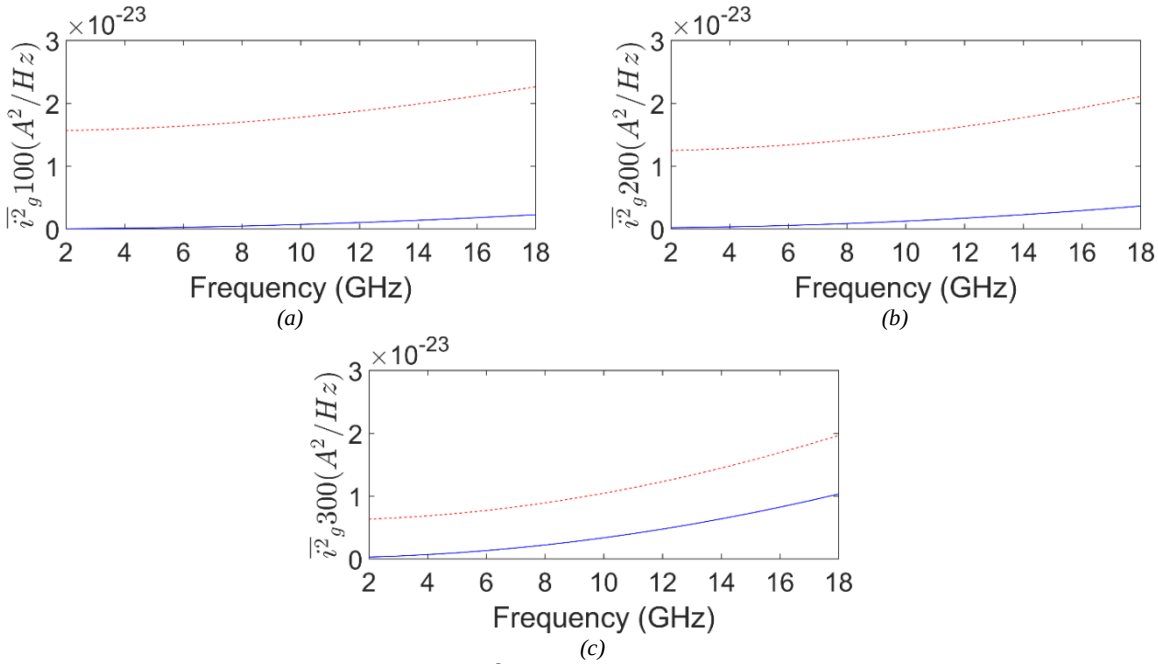

Fig. 2.10: Performance of the gate noise current $\bar{\imath}^2_g$ under light OFF (blue solid curve) and light ON (red dashed curve) conditions in the 2-18 GHz frequency range for the tested HEMTs with different gate width: (a) 100 μm, (b) 200 μm and (c) 300 μm [27].

For an in-depth investigation of the excess noise generation due to the device illumination, the widely known analytical noise model employing the K_g, K_r and K_c coefficients has been adopted [26].

This model started from the description of the noise sources in a field-effect device in terms of the intrinsic noise current sources and their correlation coefficient using the basic P, R and C coefficients. These coefficients are used to express the correlation coefficient jC with a different set of parameters. The coefficients P and R are strong functions of the drain current because of the dependence of the dipole noise contribution on the drain current itself. The expressions of the P, R and C coefficient are reported in eqs. 2.20-2.22.

$$P = \frac{\overline{|\imath_d^2|}}{4kT_0\Delta f g_m} \tag{2.20}$$

$$R = \frac{\overline{|\imath_g^2|}}{4kT_0\Delta f \omega^2 C_{gs}^2 / g_m} \tag{2.21}$$

$$jC = \frac{\overline{\imath_g^* \imath_d}}{\sqrt{\overline{|i_g^2|}\overline{|i_d^2|}}} \tag{2.22}$$

where C_{gs} is the gate-source capacitance and g_m is the device transconductance. Such coefficients can be computed from the circuit models and the relevant noise correlation matrix elements in admittance form by using the following correspondence:

$$\overline{|i_g^2|} = C_{Y11} \tag{2.23}$$

$$\overline{|i_d^2|} = C_{Y22} \tag{2.24}$$

$$C = |C_{Y21}| / \sqrt{C_{Y11}C_{Y22}} \tag{2.25}$$

The P, R, and C coefficients are plotted vs. frequency in Fig. 2.11.

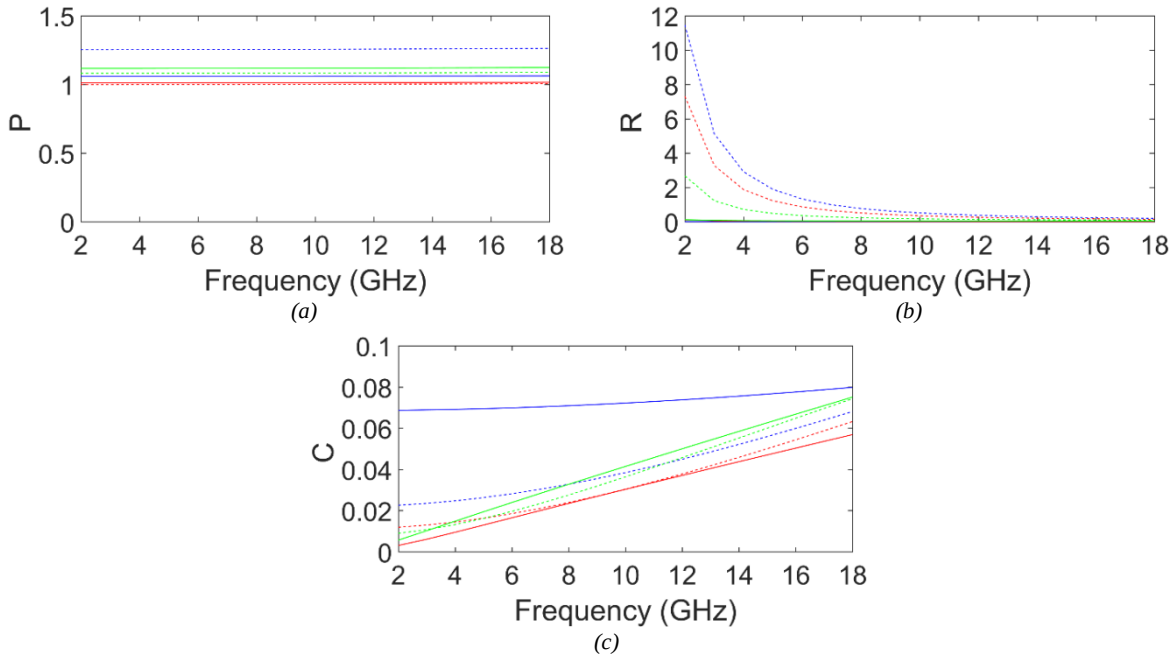

Fig. 2.11: Comparison between each set of values of the noise coefficients under light OFF (solid curve) and light ON (dashed curve) at V_{GS} = -0.6 V and V_{DS} = 2.5 V, in the 2-18 GHz frequency range for 100 μm (blue), 200 μm (red) and 300 μm (green) devices: (a) P, (b) R, (c) C [19].

By observing the behavior of the P coefficient under light OFF/ON conditions, it has been noted that its light sensitivity is maximum in the smallest device also for the contribution of the transconductance g_m term. Indeed, the effect of the noise generation related to light exposure on the P coefficient is cancelled by the predominant effect of the increases of g_m in the illuminated device.

On the basis of the P, R, and C coefficients, to obtain simple expressions for the noise parameters, another set of dimensionless noise coefficients has been introduced in [24], namely K_g, K_r and K_c, described above:

$$K_g = P\left[\left(1 - C\sqrt{R/P}\right)^2 + (1 - C^2)\,R/P\right] \tag{2.26}$$

$$K_c = \frac{\left(1 - C\sqrt{R/P}\right)^2}{\left(1 - C\sqrt{R/P}\right)^2 + (1 - C^2)\,R/P} \tag{2.27}$$

$$K_r = \frac{R(1 - C^2)}{\left(1 - C\sqrt{R/P}\right)^2 + (1 - C^2)\,R/P} \tag{2.28}$$

where K_g is related to the drain noise, K_c is related to the correlation between the drain and the gate noise and K_r is related to the gate noise. The behavior of K_g, K_r and K_c is illustrated in Fig. 2.12.

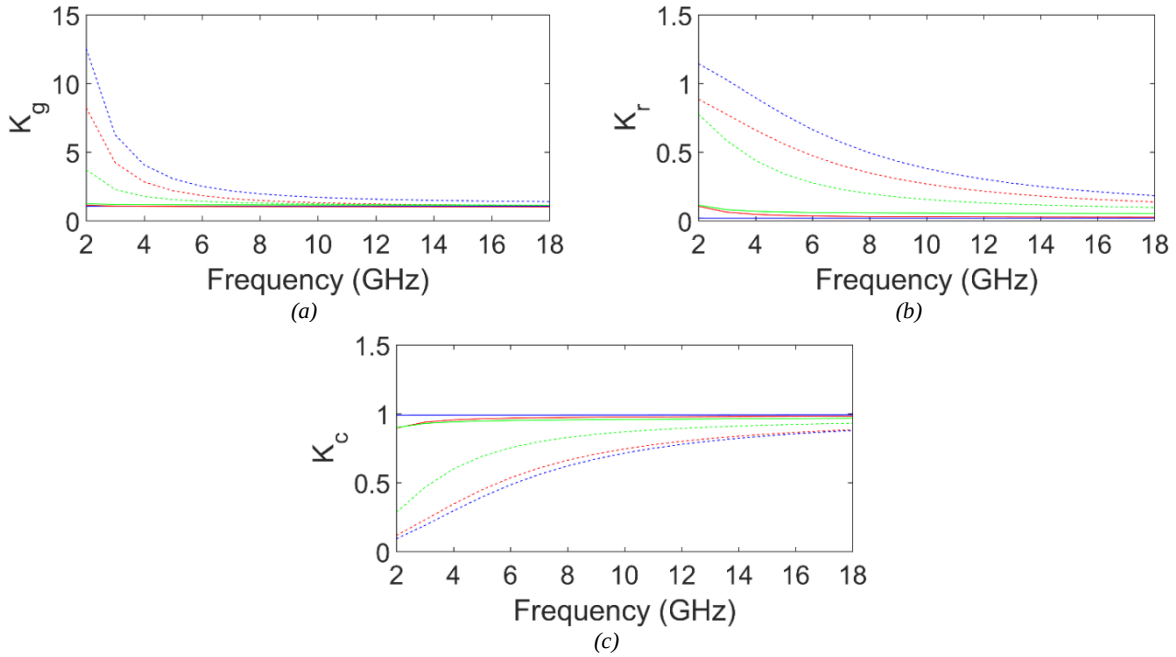

Fig. 2.12: Comparison between each set of values of the noise coefficients under light OFF (solid curve) and light ON (dashed curve) in the 2-18 GHz frequency range for 100 µm (blue), 200 µm (red) and 300 µm (green) devices: (a) K_g , (b) K_r, (c) K_c [27].

By using the KGCR model, the minimum noise figure F_{min} vs. frequency can be evaluated as follows [26]:

$$F_{min} = 1 + 2\left(2\pi f\, C_{gg}/g_m\right)\sqrt{K_g\left[K_r + g_m\left(R_g + R_s\right)\right]} + 2\left(2\pi f\, C_{gg}/g_m\right)^2\left[K_g g_m\left(R_g + R_s + K_g R_{gs}\right)\right] + \cdots \tag{2.29}$$

where truncation at the f^2 term applies. The reader will observe that in the present work the contribution of the feedback gate-drain capacitance C_{gd} is accounted for by considering the total gate capacitance C_{gg}, given by the sum of C_{gs} and C_{gd}.

To derive the noise parameters Γ_{opt} and R_n, the following equations are then used [26]:

$$R_n = \left(R_g + R_s\right) + K_r\left(\frac{1 + \omega^2 {C_{gg}}^2 {R_{gs}}^2}{g_m}\right) \tag{2.30}$$

$$g_n = K_g \frac{\omega^2 {C_{gg}}^2}{g_m} \tag{2.31}$$

$$Z_c = \left(R_g + R_s\right) + \frac{K_c}{Y_{11}} \tag{2.32}$$

$$R_{s,opt} = \sqrt{{R_c}^2 + \left(R_n / g_n\right)} \tag{2.33}$$

$$X_{s,opt} = -X_c \tag{2.34}$$

where Y_{11} is the input admittance parameter of the each device.

For achieving a correct comparison between models and measurements, the extrinsic reactive elements have been de-embedded from the experimental data. This is because the KGCR model refers to an equivalent circuit of the device without parasitic lossless elements such as series inductors and shunt/feedback capacitances [28].

Therefore, the noise parameters vs. frequency have been computed by using the eqs. from (2.29) to (2.34) and the performance of both the noise models have been compared with the experimental data in dark conditions as well as under light exposure, as shown from Fig. 2.13 to Fig. 2.16.

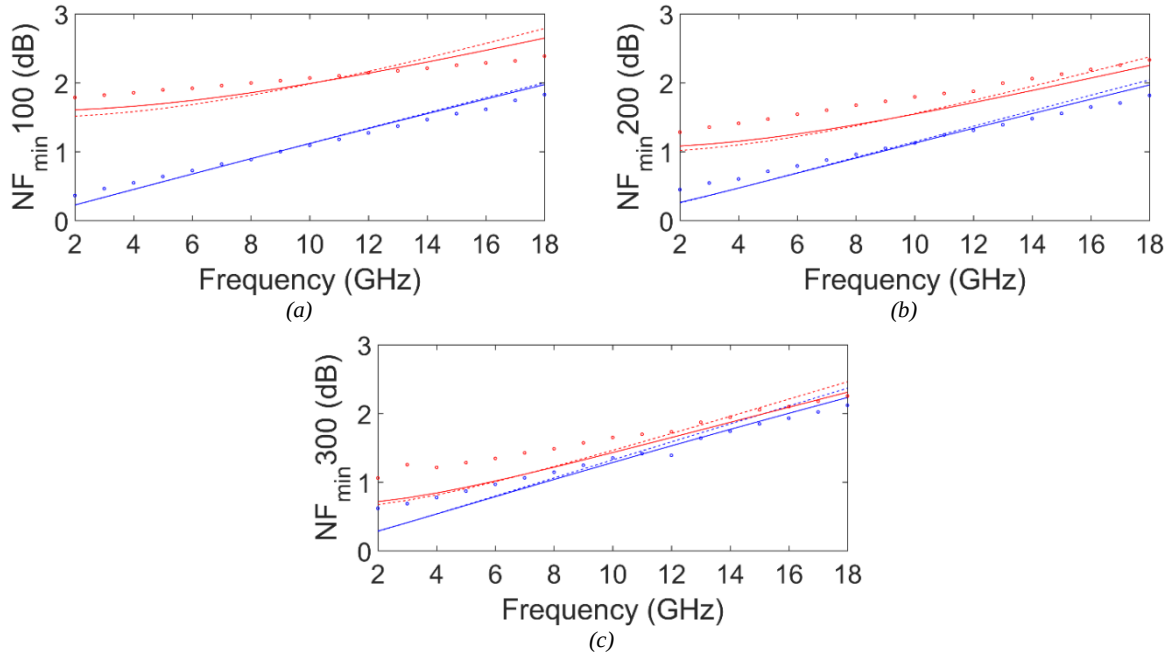

Fig. 2.13: Comparison of NF_{min} values without (blue) and with light (red) among measurements (dots), noise temperature model (dashed curve) and analytical model (solid curve) in the 2-18 GHz frequency range for the tested HEMTs with different gate width: (a) 100 μm, (b) 200 μm, (c) 300 μm [27].

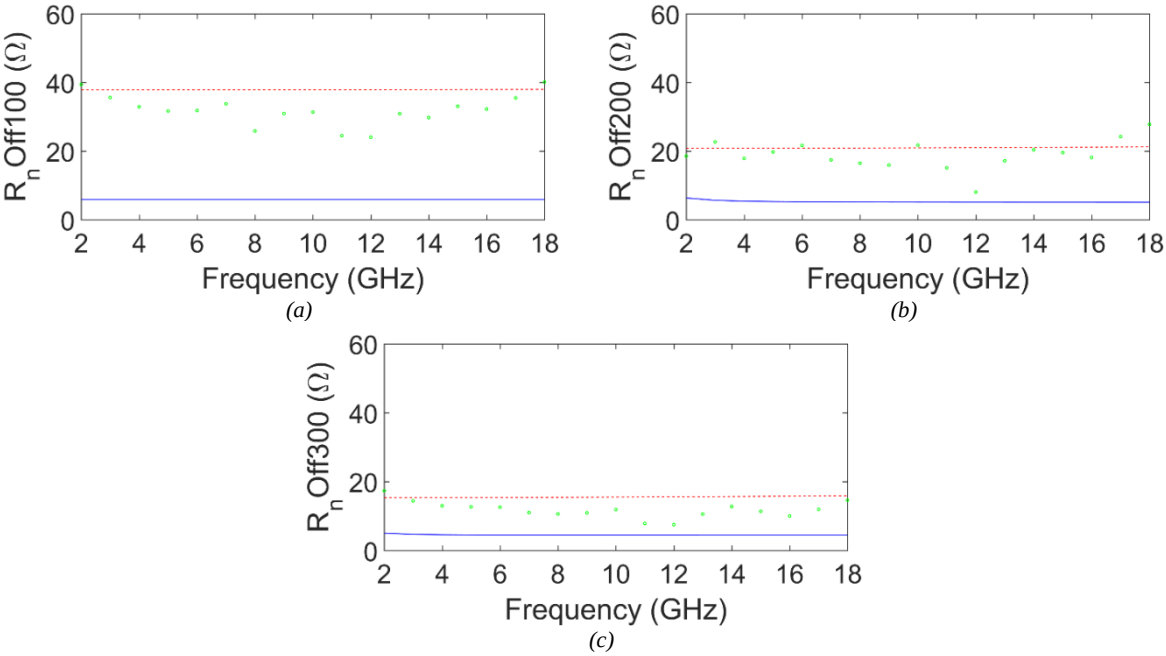

Fig. 2.14: Comparison of R_n values without light among measurements (green dots), noise temperature model (red dashed curve) and analytical model (blue solid curve) in the 2-18 GHz frequency range for the tested HEMTs with different gate width: (a) 100 μm, (b) 200 μm, (c) 300 μm [27].

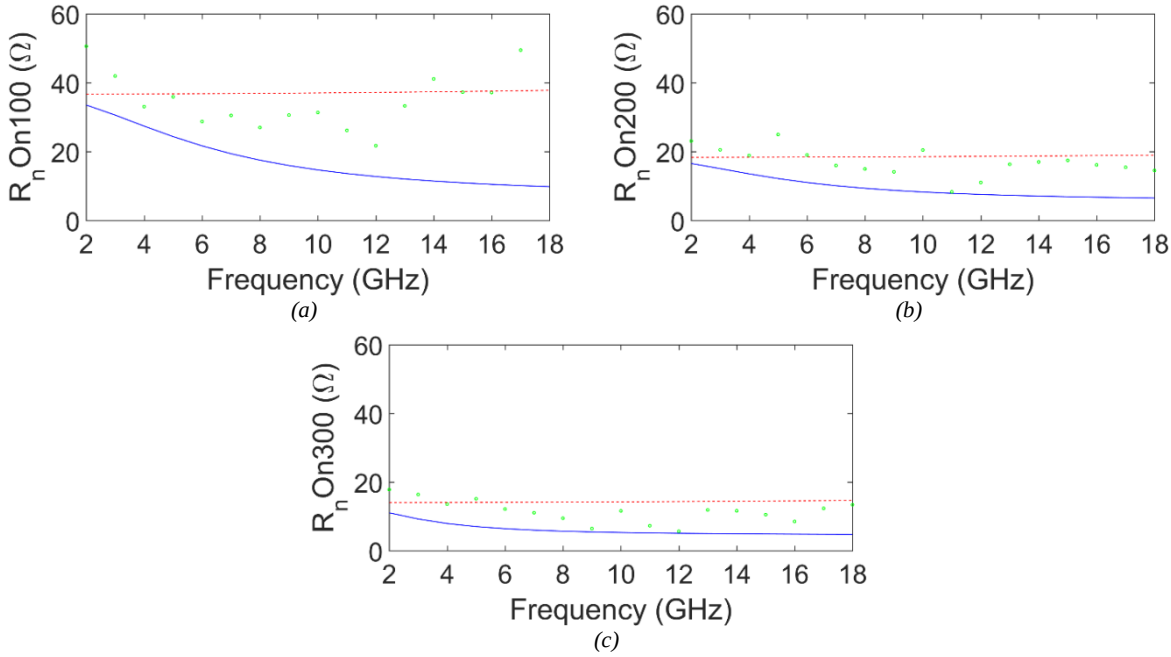

Fig. 2.15: Comparison of R_n values with light among measurements (green dots), noise temperature model (red dashed curve) and analytical model (blue solid curve) in the 2-18 GHz frequency range for the tested HEMTs with different gate width: (a) 100 μm, (b) 200 μm, (c) 300 μm [27].

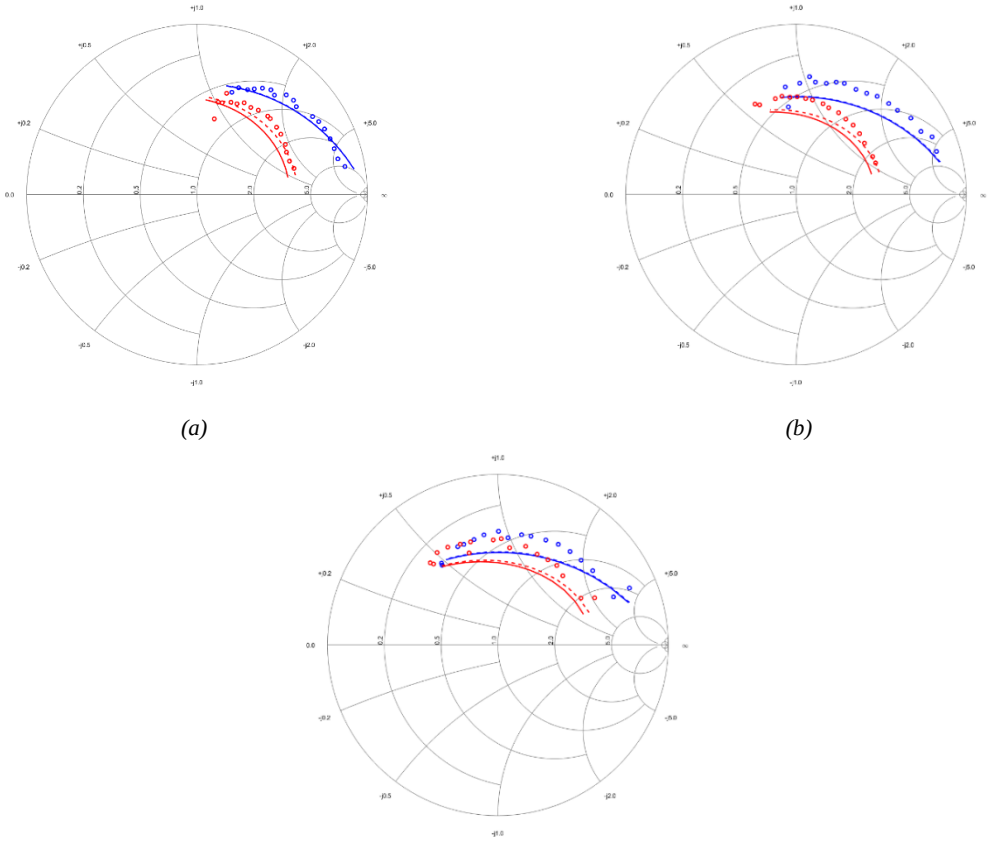

Fig. 2.16: Comparison of Γ_{opt} values without (blue) and with light (red) among measurements (dots), noise temperature model (dashed curve) and analytical model (solid curve) in the 2-18 GHz frequency range for the tested HEMTs with different gate width: (a) 100 μm, (b) 200 μm, (c) 300 μm [27].

Both models show a good accuracy in reproducing the strong degradation exhibited by the minimum noise figure during device illumination, thus suggesting their adoption for the analysis of the noise performance variations due to the light absorption (see Fig. 2.13).

As far as R_n is concerned, a poor performance of the KGCR model has been observed, which could be explained by observing the expression reported in eq. (2.30). It is evident that, apart from the expected contribution of the parasitic resistances R_s and R_g, the last term of the above equation does not contribute adequately to yield the correct value of R_n. This behavior is marked in the smallest size device in dark condition, but reduces as the device size increases as well as under light exposure (see Figs. 2.14-2.15).

The modeled optimum noise source reflection coefficient Γ_{opt} exhibits some discrepancies for the largest size device but shows its effectiveness in reproducing the variation between the dark and the light exposed condition, as reported in Fig. 2.16.

The main effect of the light exposure is represented by the increase of the gate current due the photogenerated electron-hole pairs separated by the electric field existing between gate and source. This aspect is effectively modeled by the R_{gsf} and R_{gdf} elements at the input and feedback section of the circuit model as reported in [19]. In addition, these two resistances need to be characterized by a high noise temperature to fit the remarkable increase of F_{min} under illumination.

By using the KGCR model, the relationship between the P, R, C and the K_g, K_r, K_c noise coefficient sets has been clearly observed. As reported in Fig. 2.11, the performance of all P, R and C coefficients is sensibly influenced by the photogeneration effect but the strongest variations are exhibited by R, as it is strictly related to the gate noise source (as seen in eq. (2.21)). It is also pointed out that the origin of this noise source is not correlated with the noise current existing in the channel thus causing a decrease of the value of C with a further increase of the minimum noise figure. Such consideration applies to each device size, with a general trend for decreasing effects of the light activation of noise with increasing gate width even though the behavior of $\bar{i}^2_g$ reported in Fig. 2.10 does not enlighten significant differences between the 100 and the 200 μm gate width devices.

A sensitivity analysis of the K_g, K_r and K_c noise coefficients has shown that their light sensitivity has to be ascribed mainly to the R parameter. The K_g coefficient values are highly affected by light exposure following a trend that exhibits a nice scalability according to the

device size. The K_c coefficient values tend to unity except for the lower frequency region under light exposure due to the large increase of R, as previously observed.

Eventually, when adopting optical control with field-effect transistors a generation of excess noise levels is to be expected during light exposure consistent with the increase of gate noise current generation. It has been assessed with increased device sizes that this noise degradation is fully reproduced by expanding the equivalent circuit with two intrinsic resistors to fit the S- and N-parameters under illumination. The topics treated above have been detailed and presented in a paper recently submitted for publication [27].

A different way for characterizing the microwave transistor noise adopts the transistor noise models in microwave circuit simulators. In the last few decades, although there have been plenty of studies dealing with the modeling of the microwave transistor noise parameters, only a small number is related to the noise parameter modeling for the case of devices under light exposure and to the best author's knowledge none of them is devoted to the wave modeling approach application.

The power of the wave representation of noise lies in its compatibility with the scattering matrix description of microwave networks. It permits the use of scattering matrices for the noise computations leading to advantages in Computer-Aided Design (CAD) of microwave networks. Therefore, in the case of the wave representation of noise, the noise analysis problems are formulated using scattering parameters. This is very important since they can be measured with high precision using vector network analyzers, which further contribute to the accuracy of the noise analysis. Furthermore, the noise wave representation offers alternative measurement techniques [29 – 31].

Within the framework of a close collaboration with the Faculty of Engineering, University of Nis, Serbia, an application of this approach has been developed and its results are here presented.

Hereby, the wave approach for the noise modeling of the GaAs HEMT under optical illumination is reported. The model has been developed for the 100 μm HEMT, and its accuracy has been verified by comparing the simulated and measured data with and without optical illumination. A detailed analysis of the wave approach and its applications to the topic treated above have been presented in a paper recently submitted for publication [32].

Based on the determined noise parameters of transistor intrinsic circuit, the noise wave temperatures were calculated for both illumination conditions using eqs. (2.35-2.37), in the whole frequency range within which the noise parameter measurements were performed.

$$T_a = T_0\left(F_{min,i} - 1\right) + \frac{4R_{n,i}T_0\left|\Gamma_{opt,i}\right|^2}{Z_0\left|1+\Gamma_{opt,i}\right|^2} \tag{2.35}$$

$$T_b = \frac{4R_{n,i}T_0}{Z_0\left|1+\Gamma_{opt,i}\right|^2} - T_0\left(F_{min,i} - 1\right) \tag{2.36}$$

$$T_c = \frac{4R_{n,i}T_0\Gamma_{opt,i}}{Z_0\left|1+\Gamma_{opt,i}\right|^2} \tag{2.37}$$

After that, the calculated noise wave temperatures were used for building the appropriate training sets used to train several ANNs with one hidden layer and different number of hidden neurons. For the process of ANN training the Levenberg-Marquardt algorithm was used [33]. Among the trained neural networks, ANNs with the highest accuracy have two hidden neurons in the case of non-illuminated device and three hidden neurons in the case with illumination. These ANNs were used to determine the noise wave temperatures in the same frequency range. Then, the obtained noise wave temperatures, which are presented in Fig. 2.17, were assigned to the noise wave model implemented within Advanced Design System® (ADS) circuit simulator of Keysight, and the transistor noise parameters were simulated. Finally, the simulated transistor noise parameters were compared with the corresponding measured data in both cases.

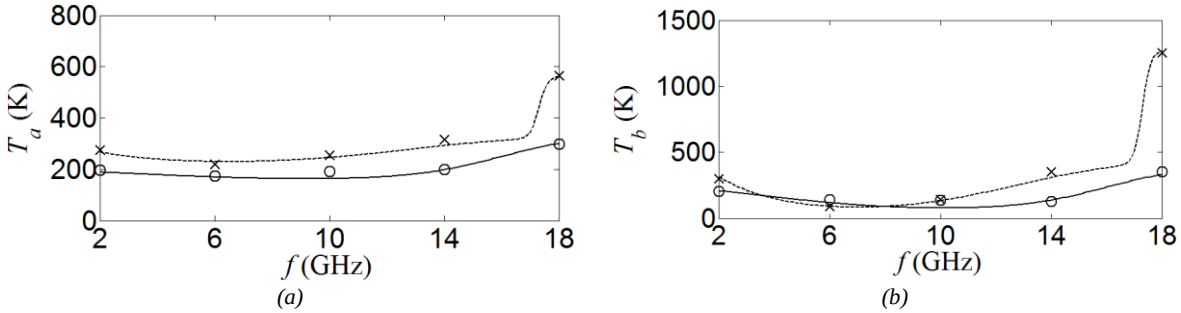

(a) *(b)*

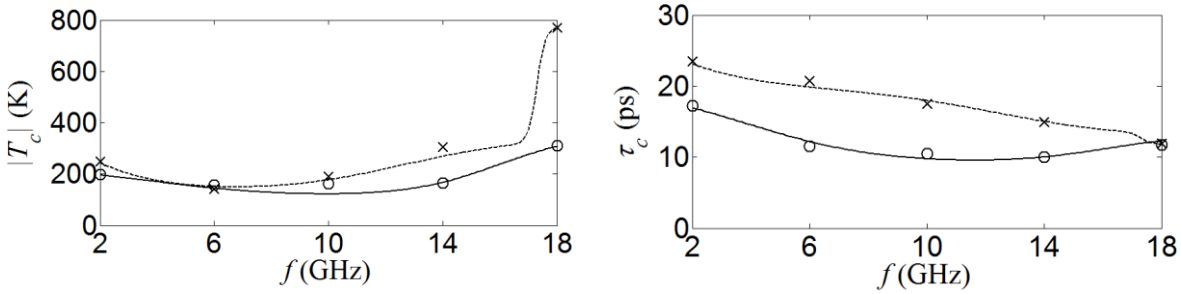

(c) *(d)*

Fig. 2.17: Calculated noise wave temperatures (circles – without illumination; crosses – with illumination) fitted by ANN (solid lines - without illumination; dashed lines – with illumination): (a) T_a, (b) T_b, (c) $|T_c|$, and (d) τ_c [32].

Figures 2.17 and 2.18 present the simulated F_{min}, R_n, and Γ_{opt} and the corresponding measured data. The results shown in Figs. 2.18 and 2.19 were obtained in the case of GaAs HEMT without and under optical illumination, respectively, in the frequency range from 2 to 18 GHz. It can be seen that the simulated values of the noise parameters are very close to the measured ones, verifying the noise wave model accuracy.

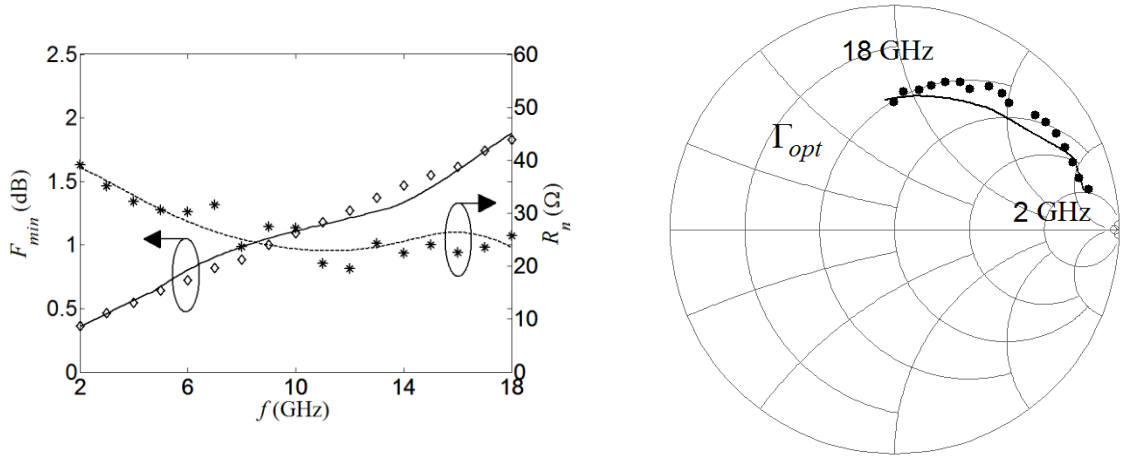

(a) *(b)*

Fig. 2.18: Noise parameters obtained by the noise wave model (lines) compared with the measured noise parameters (symbols) in the case of GaAs HEMT without optical illumination: (a) F_{min} and R_n, and (b) Γ_{opt} [32].

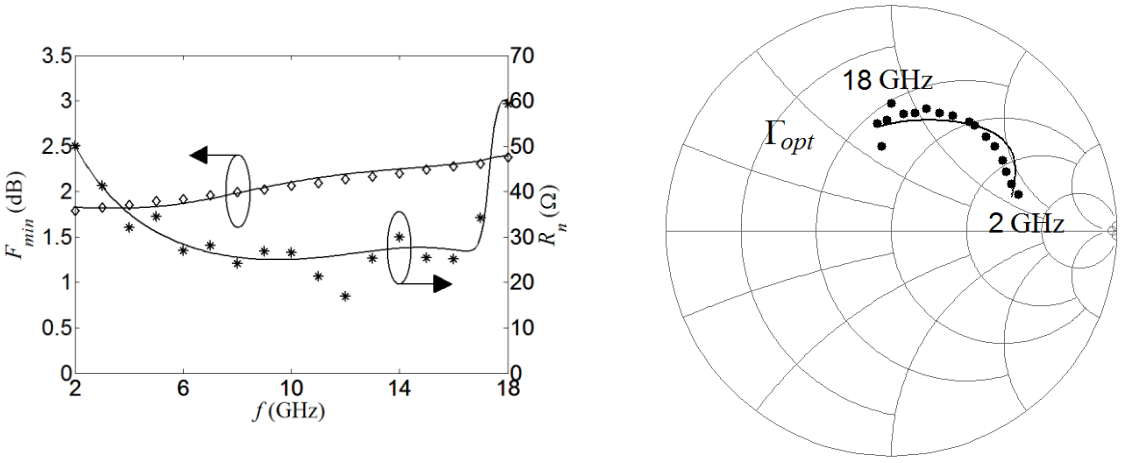

(a) *(b)*

Fig. 2.19: Noise parameters obtained by the noise wave model (lines) compared with the measured noise parameters (symbols) in the case of GaAs HEMT under optical illumination: (a) F_{min} and R_n, and (b) Γ_{opt} [32].

2.2.3 Microwave GaN-based transistors under light exposure

As mentioned before, when the application is high power demanding, the GaN semiconductor is used instead of GaAs. The GaN-based technology has made a great leap forward during the last twenty years for high-power microwave circuits and systems employing solid-state components. In addition, GaN high electron mobility transistors (HEMT) are more than promising candidates for those low-noise circuits requiring high isolation characteristics due to their satisfactory noise performance together with excellent linearity and inherent robustness. Fully integrated microwave GaN transceivers are extensively investigated, pointing towards high performance miniaturized circuitry for advanced telecommunication systems [34], [35].

Besides, GaN is a highly responsive material to the ultraviolet radiation, i.e. to an optical radiation whose photon energy can be absorbed in either the GaN and the AlGaN layer. This property not only makes GaN HEMT's excellent UV photodetectors, but can also be effectively exploited in optically controlled and optically switched integrated circuits where control/activation of the semiconductor devices is powered by light exposure [36], [37].

Hereby, a study on the microwave linear and noise performance of a low-noise GaN HEMT under CW UV illumination will be presented. The device, having 0.25 μm gate length and 100 μm gate width, has been characterized by measuring its (a) DC performance, (b) linear

scattering parameters, (c) noise parameters either in dark condition and under CW light exposure at 375 nm. A circuit model extraction has then been performed to analyze more deeply the effects of the UV exposure of the GaN HEMT on the behavior of the scattering and the noise parameters.

The present study has been performed on an AlGaN/GaN HEMT on SiC substrate with a gate length of 0.25 μm and a gate width of 100 μm (2x50 μm gate fingers in parallel) manufactured by United Monolithic Semiconductors.

To contact the device, a Cascade Microtech M150 on-wafer station with ground-signal-ground (GSG) probes has been used. The UV (375 nm) beam has been spotted on the transistor layout by means a focusing system connected to the light source with an optical quartz fiber.

The integrated microwave measurement system is software driven to switch automatically between the noise calibration/measurement chain and the scattering (S-) parameter measurement chain without removing any part or connection of the instruments. The block diagram of the measurement system is shown in Fig. 2.20.

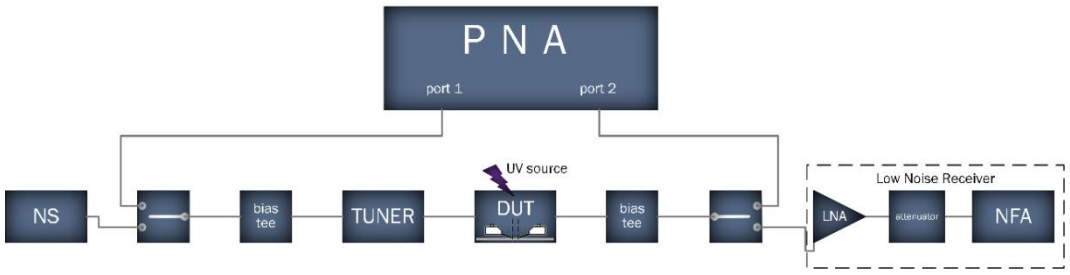

Fig. 2.20: Block diagram of the measurement system [38].

The device input is connected to a tuner (Maury MT-983BU01), whose input can be switched towards either the input port of the vector network analyzer (Agilent E8364A PNA) and the noise source (Agilent N4002A SNS). Moreover, the device output can be switched towards either the output port of the PNA and the input of the low noise receiver. The noise receiving section includes a low noise amplifier (LNA) and an attenuator, to set the correct power level that can be handled by the noise figure analyzer (Agilent N8975A NFA). A photograph of the experimental set-up is reported in Fig. 2.21.

Fig. 2.21: Picture of the measurement system [39].

As a first step, the DC analysis of the device has been performed. Once the measurement bias point has been chosen, both the S-parameters and the N-parameters have been measured.

Each set of measurements (DC, S-parameters, N-parameters) has been performed first in dark condition and, shortly after, under CW light exposure. An incident power density of 0.7 $nW/\mu m^2$ has been estimated from measurement of the output power at the end of the focusing optics. Such value could not be raised due to the inherent limitations of the illuminating system, but was enough to prove the occurrence of light absorption effects in the GaN HEMT tested. This has possibly led to a very low level of absorbed power due to the non-transparent behavior of the gate electrode which limits the size of the optical absorbing region and the device optical responsivity.

According to the device structure and the optical sensitivity of the relevant materials, when the photons are absorbed only in the GaN layer, an increase in the electron concentration of the 2-DEG channel occurs, the so-called photoconductive effect, leading to a photo-generated current due to excess carriers. In addition, the photo-generated holes in the active channel accumulate beneath the source region and effectively lower the potential barrier between the source and the channel, the so-called internal photovoltaic effect. The net effect due to this barrier lowering is a decrease of the threshold voltage and the increase of the drain current [39], [40]. When the photon energy matches the bandgap of the AlGaN layer and a high bias resistance is present, an external photovoltaic effect occurs dominantly and a noticeable forward

voltage arises across the gate plus the AlGaN Schottky barrier. In the last case, excess carriers are also generated in the AlGaN layer.

In this study, a slight internal photovoltaic effect and a small photoconductive current are expected because the incident photon energy is too low to interact with the AlGaN material, even for a reduced value of the Al mole fraction (typically, for GaN HEMT an Al content of 0.2 ÷ 0.4 is used).The device characterization has started with a complete DC analysis in order to explore its basic performance and to perform a careful choice of the bias point for the microwave parameter measurements. In addition, the changes due to the light exposure in DC condition has helped to understand the main processes occurring as a consequence of photon absorption within the internal semiconductor layers. The DC device response has been analyzed within the 0 ÷ 15 V drain-source voltage V_{DS} range and the -3 ÷ 1 V gate-source voltage V_{GS} range. The output characteristics I_{DS}- V_{DS} in Fig. 2.19 (a) are measured at V_{GS} values from −3 V to 1 V with 1 V step. The I_{GS}-V_{DS} curves in Fig. 2.19 (b) are measured at V_{GS} values of -3 V and -2 V. The transfer characteristics I_{DS}- V_{GS} in Fig. 2.19 (c) are measured at V_{DS} = 10 V. An expanded view is presented in Fig. 2.19 (d) for V_{GS} values between -3.5 V and 3 V, in order to show the shift of the threshold voltage due to the 375 nm illumination consistent with the occurrence of an internal photovoltaic effect. Finally, the DC transconductance g_m is reported in Fig. 2.22 (e). Likewise, the shift of the g_m curve demonstrates the occurrence of the internal photovoltaic effect.

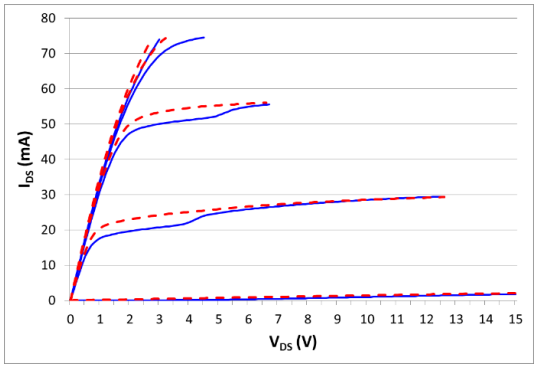

(a)

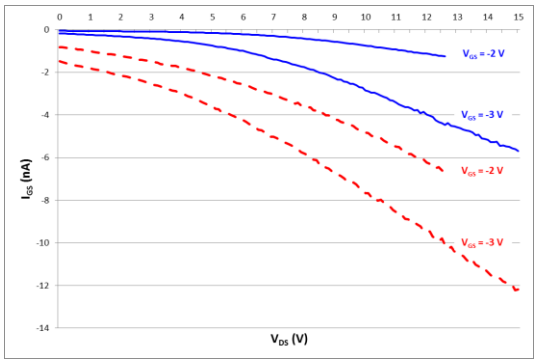

(b)

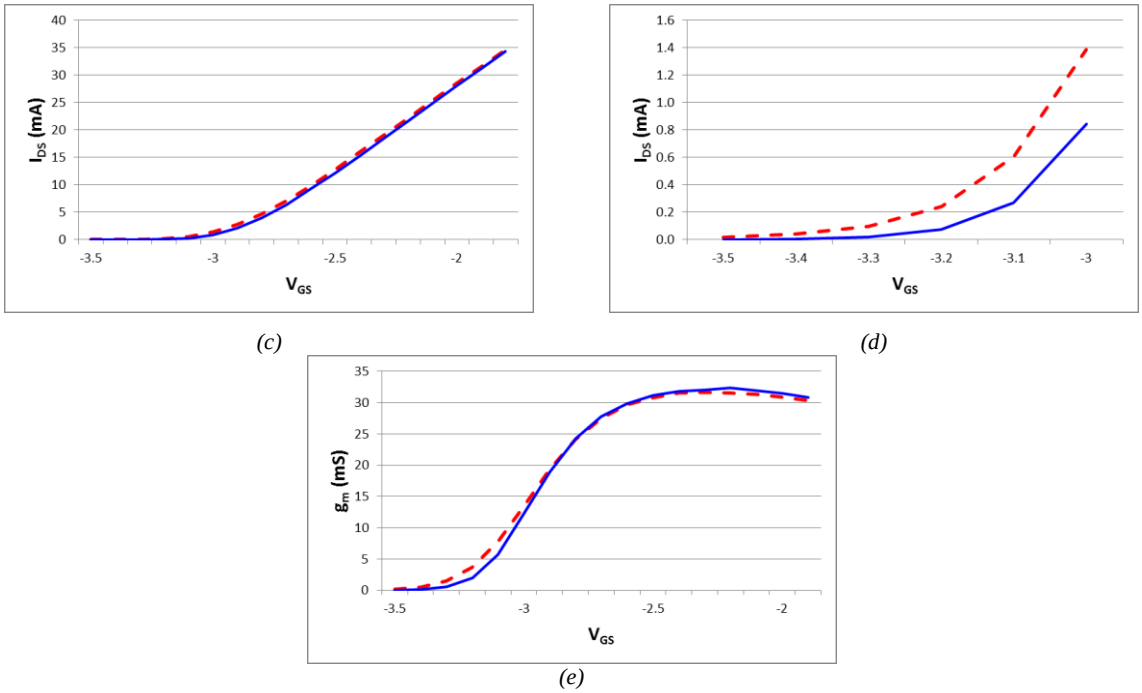

Fig. 2.22: DC behavior of the GaN HEMT without (blue solid line) and with (red dashed line) UV illumination: (a) I_{DS}-V_{DS} at V_{GS} values from −3 V to 1 V with 1 V step, (b) I_{GS}-V_{DS} at V_{GS} values of -3 V and -2 V, (c) I_{DS}-V_{GS} at V_{DS} = 10 V, (d) expanded view of I_{DS}-V_{GS} at V_{DS} = 10 V for V_{GS} values between -3.5 and 3 V, (e) g_m-V_{GS} at V_{DS} = 10 V [38].

The plots reported in Fig. 2.22 (a, b) show that the magnitude of both drain I_{DS} and gate I_{GS} currents vs. V_{DS} voltage increase when the device has been exposed to UV light, notably in the pre-saturation region. As a consequence, the kink effect that characterizes the I_{DS} behavior in dark condition disappears under light exposure. Again, this is consistent with de-trapping processes activated by light absorption in III-V semiconductor devices [41].

The S-parameters have been measured at V_{DS}= 10 V, I_{DS}= 10 mA in the 2-26 GHz frequency range. It is important to evidence that the drain current has been kept at a constant value during device illumination, i.e. the gate-source voltage V_{GS} has changed under illuminated condition. Therefore, the value of V_{GS} during exposure has been lowered with respect to the dark condition to maintain I_{DS} = 10 mA. This has been aimed at ruling out effects of the N-parameters merely due to the increase of the drain current under light exposure [14].

A slight change in all S-parameters has been found: in details, the magnitude of S_{22} decreases whereas the magnitude of S_{11}, S_{12} and S_{21} increases. The increase of $|S_{21}|$ is a well-known effect in optically stimulated transistors due to the charge generation. The comparison between S-parameters measured in dark and illuminated condition are shown in Fig. 2.23.

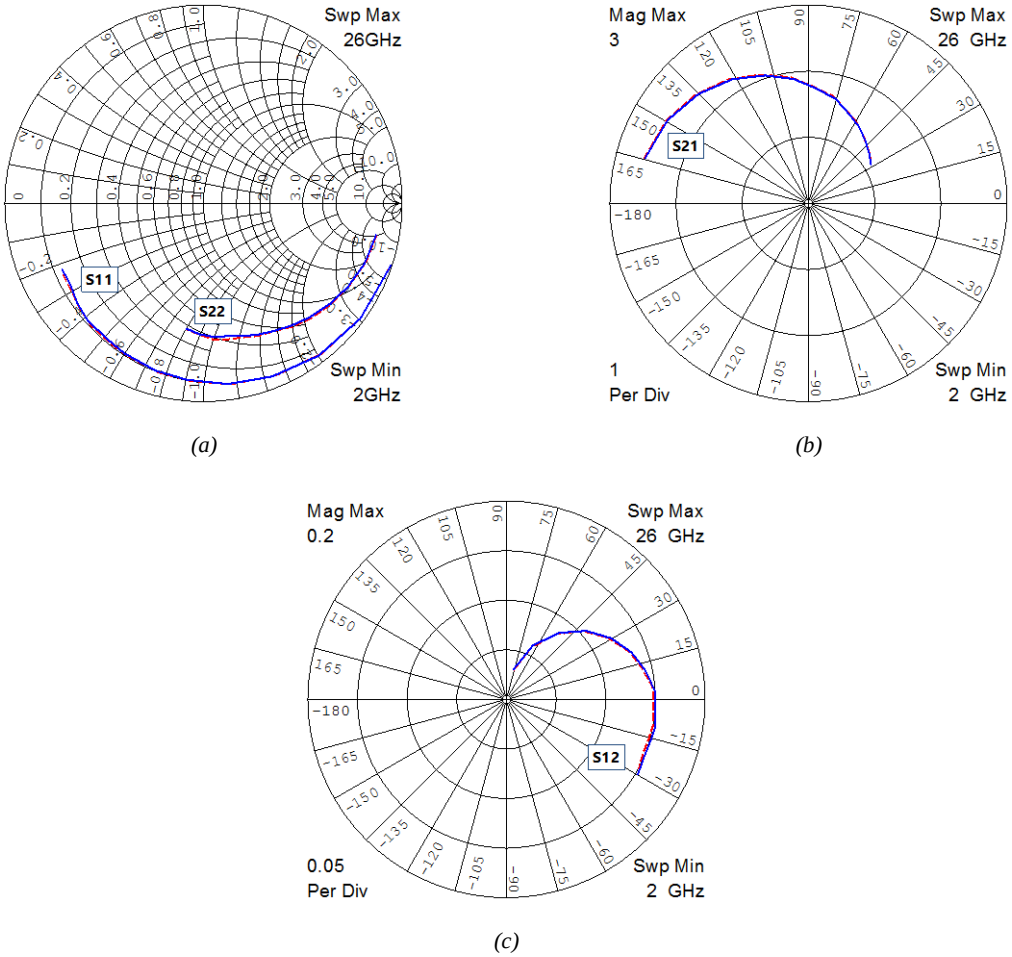

Fig. 2.23: Comparison between S-parameters measured without (blue solid line) and with (red dashed line) UV illumination. (a) S_{11} and S_{22}, (b) S_{21}, and (c) S_{12} [38].

As far the N-parameters are concerned, they have been determined by following the same procedure employed for the S-parameters. In the previous extensive characterization of GaAs devices exposed to visible radiation, different levels of light effects have been experienced [13], [19].The N-parameters before and during UV light exposure of the GaN HEMT under test are reported in Fig. 2.24 (a-c). For each parameter a typical trend is recognizable, i.e. the occurrence of a crosspoint between the dark and illuminated performance that makes it difficult to assess either a net beneficial or detrimental contribution due to device illumination.

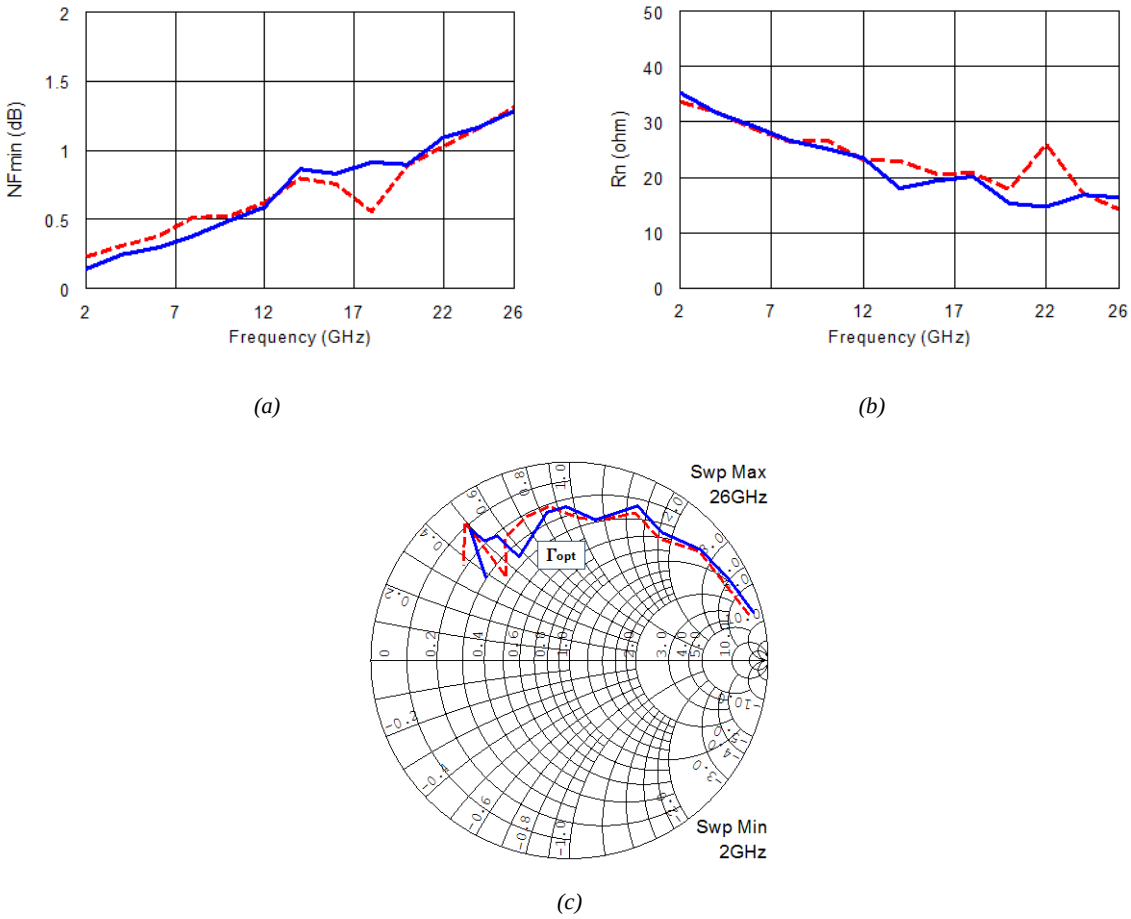

(a) *(b)* *(c)*

Fig. 2.24: Comparison between N-parameters determined without (blue solid line) and with (red dashed line) UV illumination. (a) NF_{min}, (b) R_n, (c) Γ_{opt} [38].

For example, in the graph in Fig. 2.24 (a) showing the NF_{min} behavior, a clear change in the line slope occurs, with a crosspoint located around 12 GHz, but the same note can be brought to evidence for the remaining N-parameters. In details, the noise figure behavior exhibits a degradation in the lower frequency range (<12GHz) whereas the noise resistance performance worsens at higher frequencies (>12GHz). With concern to the Γ_{opt} coefficient, it can be observed that a decrease of its magnitude alleviates the noise mismatch when referring to the standard characteristic impedance of 50 Ω typically used in microwave circuit design. In view of this consideration, the performance of Γ_{opt} seems to improve in the lower frequency range during UV illumination since it moves toward the center of the Smithchart. However, it would be very interesting to verify the above results at higher optical power levels where the device responsivity might exhibit a non linear trend.

The small-signal performance of microwave field-effect transistors is accurately reproduced by means of a linear circuit model provided with noisy resistors, i.e. resistors associated with a temperature value to produce thermal noise [5, 7]. Therefore, either the S-parameters and the N-parameters can be easily simulated by computer-aided analysis. The circuit element values are extracted from the S-parameter measurements using different approaches, whereas the noise temperatures are usually adjusted to fit the N-parameters.

In this case, an optimization approach has been used to fit S-parameters in dark condition starting from suitable initial values for the device technology under test. The final circuit model is shown in Fig. 2.25.

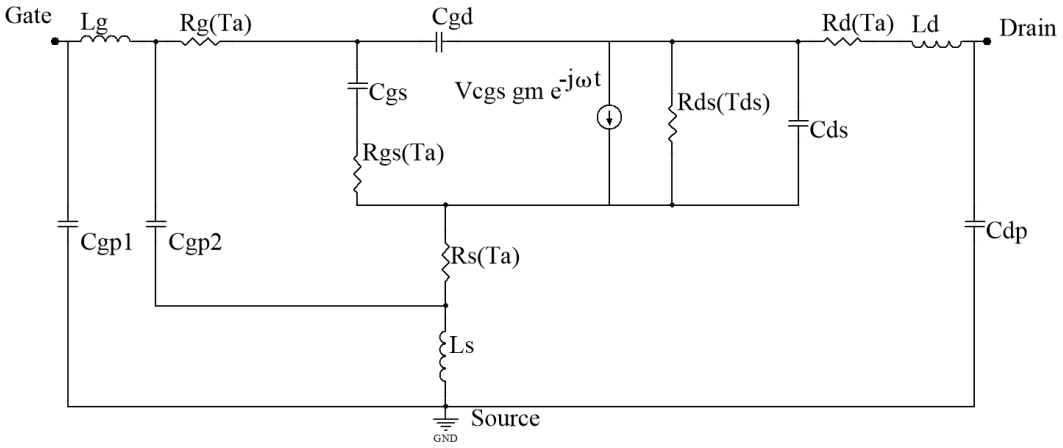

Fig. 2.25: Equivalent circuit noise model for a GaN HEMT in dark condition [38].

Afterwards, the noise temperatures have been associated to the resistors, following the widely adopted Pospieszalki's model that associates a fictitiously high excess temperature to the shunt drain-source resistor R_{DS} while all the other resistors are kept at ambient temperature [7].

The value of the R_{DS} noise temperature has been found to reach 3000°C for an optimal fitting of the N-parameters in dark condition as reported in Fig. 2.26 where the comparison between measured and modeled values of NF_{min} (a), R_n (b) and Γ_{opt} is shown.

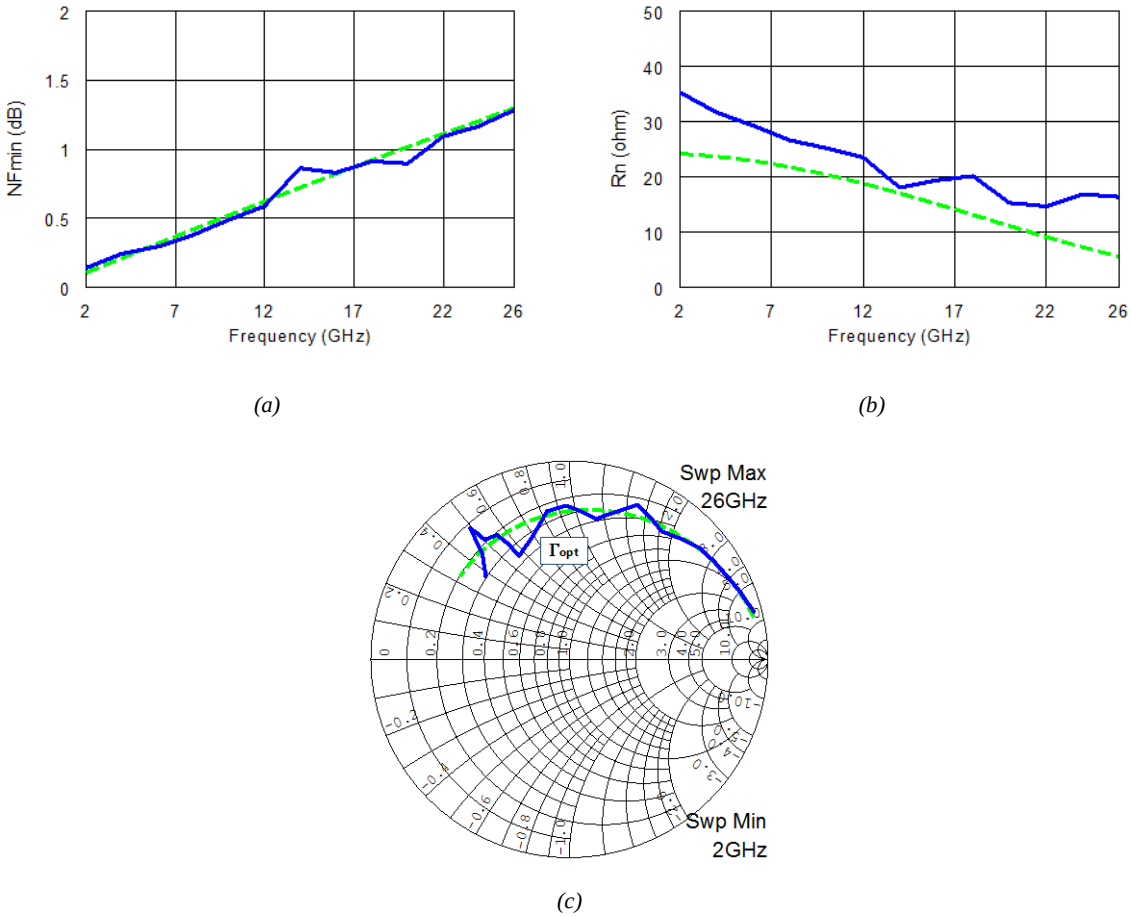

(a) *(b)*

(c)

Fig. 2.26: Measured (blue solid line) and simulated (green dashed line) N-parameters of the GaN HEMT in dark condition. (a) NF_{min}, (b) R_n, (c) Γ_{opt} [38].

Since the S-parameters with light exposure do not exhibit remarkable changes, we decided not to vary the circuit element values. Instead, we inserted a shunt resistor R_{GSf} between the internal gate and source terminals to account for the effects of the increased gate conduction occurring under illumination, as demonstrated by the three-fold increase of the gate current at the bias point, as recognizable in Fig. 2.22 (b).

The circuit model for the device behavior under illumination is reported in Fig. 2.27.

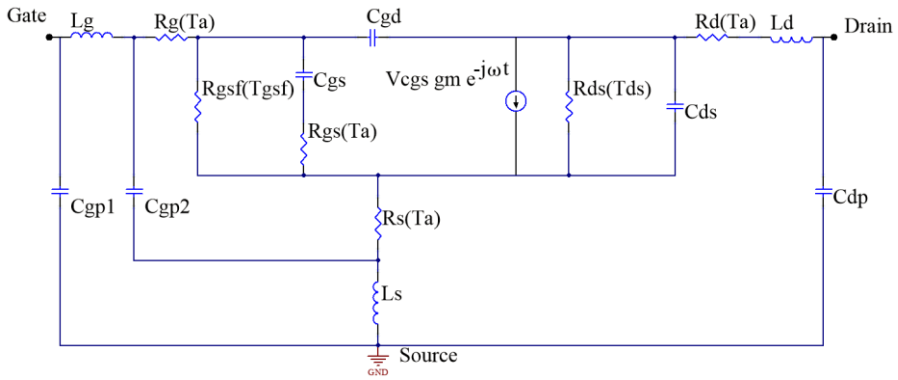

Fig. 2.27: Equivalent circuit noise model for a GaN HEMT under light exposure [38].

The element R_{GSf} has been brought to 3053°C to let the minimum noise figure fit the measured trend. The model performance under light exposure is shown in Fig. 2.28 where the comparison between measured and modeled values of NF_{min} (a), R_n (b) and Γ_{opt} is reported.

The model element and temperature values are listed in Tab. II.III for either dark and light exposure condition.

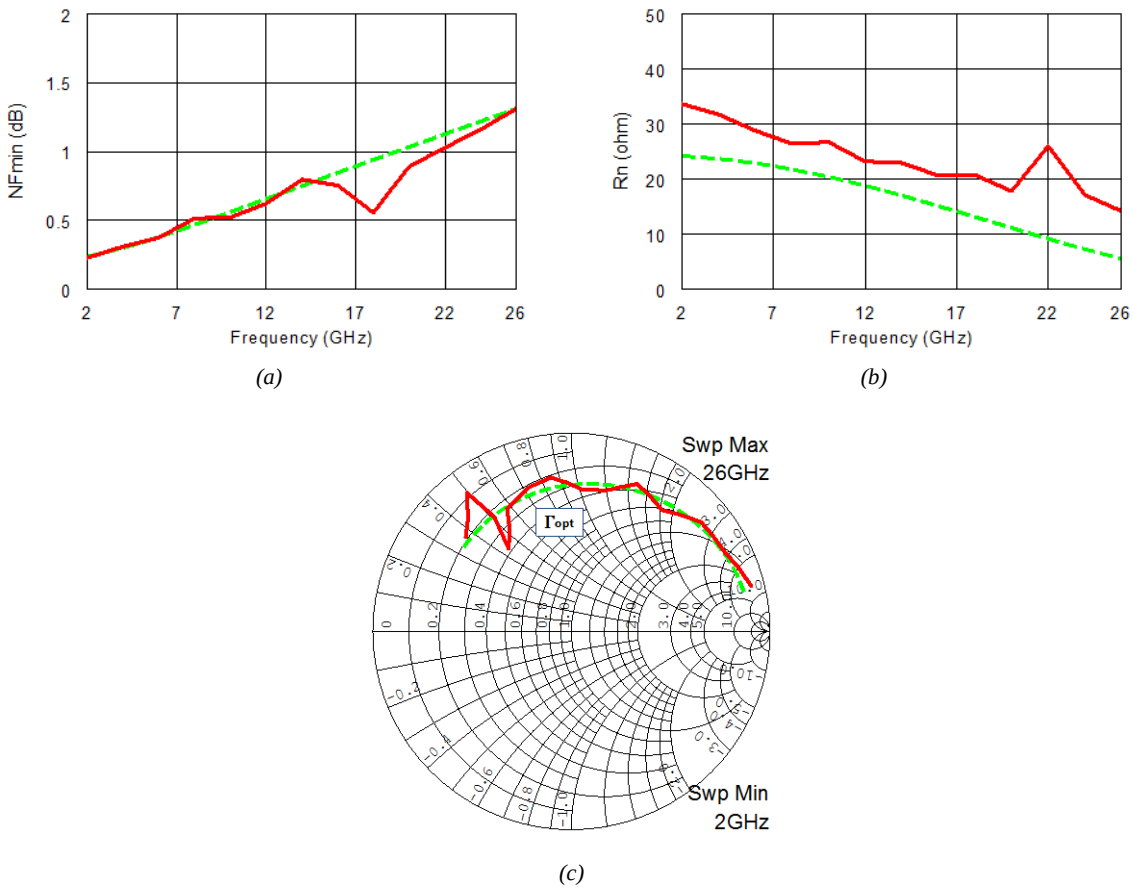

(a) *(b)* *(c)*

Fig. 2.28: Measured (red solid line) and simulated (green dashed line) N-parameters of the GaN HEMT under light exposure. (a) NF_{min}, (b) R_n, (c) Γ_{opt} [38].

The model behavior seems to work satisfactorily even if should be desirable to test its robustness at higher optical power levels, where a greater photocurrent generation might cause an increased amount of channel noise that has to be accurately modeled as well.

TABLE II.III. Values of the circuit elements and the equivalent noise temperatures for the GaN HEMT without and with UV illumination [38].

Element	***Dark value***	***Light value***
C_{GS} *(pF)*	0.087	0.087
R_{GS} *(Ω)*	2	2
C_{GD} *(pF)*	0.0257	0.0257
g_m *(mS)*	29.5	29.5
τ *(ps)*	1.3	1.3
R_{DS} *(Ω)*	665	665
T_{RDS} *(°C)*	3000	3000
C_{DS} *(pF)*	0.0699	0.0699
R_G *(Ω)*	2	2
L_G *(nH)*	0.14	0.14
C_{PG1} *(pF)*	0.0425	0.0425
C_{PG2} *(pF)*	0.0425	0.0425
R_D *(Ω)*	2	2
L_D *(nH)*	0.03	0.03
C_{PD} *(pF)*	0.018	0.018
R_S *(Ω)*	0.65	0.65
L_S *(nH)*	0.01	0.01
R_{GSf} *(kΩ)*	-	433
T_{GSf} *(°C)*	-	3053

2.3 Low-noise amplifiers

As stated before, the LNA is employed as the first active stage of a radar receiver, in order to amplify the very weak received signal with a minimum additional noise. The steps for designing a low-noise amplifier are complex and an extensive dissertation can be found in the scientific literature, e.g. in [6]. Nevertheless, the general concepts of the LNA's design will be introduced for a better understanding of the following paragraphs.

To build an amplifier, the first step is the choice of the suitable device and, thereafter, the bias point according to the desired performance. A lower bias current is needed for achieving a

low level of noise figure, but gain performance cannot be neglected, therefore, a satisfactory trade-off must often be sought.

To design a good LNA, an optimum matching at the input and output port of the active device is needed for transforming:

- ✓ The input termination for best noise performance with the tradeoff of obtaining an adequate input return loss.
- ✓ The output termination for best gain performance.

This can be accomplished by either lumped element networks (if the frequencies are in the low microwave range) or distributed networks (such as planar transmission lines). Microwave systems usually work in a 50 Ω environment, so that the normalized source Γ_S and load Γ_L reflection coefficients are equal to zero. The general situation has been reported in Fig. 2.29, where the active device behavior is represented by a scattering parameters network:

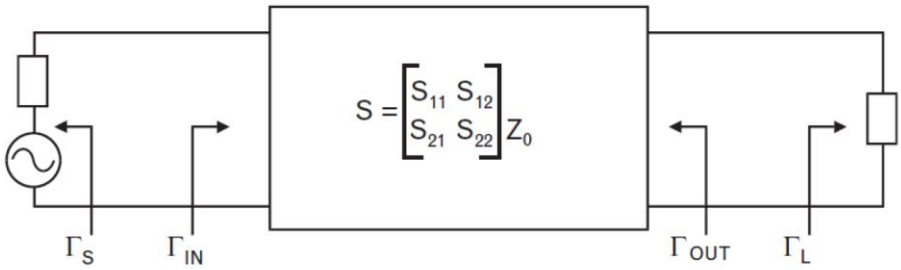

Fig. 2.29: S-parameters network connected with an input source and an output load.

where Γ_{in} and Γ_{out} are the input and output reflection coefficients looking into the active device and can be computed as follows:

$$\Gamma_{in} = S_{11} + \frac{S_{12}S_{21}\Gamma_L}{1 - S_{22}\Gamma_L} \tag{2.38}$$

$$\Gamma_{out} = S_{out} + \frac{S_{12}S_{21}\Gamma_S}{1 - S_{11}\Gamma_S} \tag{2.39}$$

If the device is unilateral ($S_{12} = 0$) no interaction takes place between the input and the output port and $\Gamma_{in} = S_{11}$ as well as $\Gamma_{out} = S_{22}$. In such a condition, the design of the LNA is very simple because of several reasons:

- ✓ The device is inherently.
- ✓ The input matching network will be designed for minimum noise figure (thus the objective will be $\Gamma_S = \Gamma_{opt}$) with the only tradeoff of obtaining an adequate input return loss.
- ✓ The output matching network will be designed for maximum gain $\Gamma_L = \Gamma_{out}^* = S_{22}^*$.

Unfortunately, at microwave frequencies, the S_{12} of the transistor is not equal to zero and this causes two main problems. The former is that the input port is influenced by the load reflection coefficient as well as the output port by the source reflection coefficient as visible in eqs. (2.38) and (2.39). The latter is that this bilateral behavior may lead to potential instability, i.e. to the possibility of oscillations.

The instability can set the device into a steady-state oscillation or stop it completely. Finally there is a remarkable risk level of damaging.

Therefore, the most important test to perform at the beginning of the amplifier design is to verify the stability performance of the device. One possibility is the evaluation of the Rollet's stability factor, K, by using two coefficients based on the scattering parameters of the transistor. The conditions shown in eqs. (2.40) and (2.41), must be respected for guarantying the unconditional stability of the transistor:

$$K = \frac{1 - |S_{11}|^2 - |S_{22}|^2 + |\Delta|^2}{2|S_{12}S_{21}|} > 1 \tag{2.40}$$

$$B = 1 + |S_{11}|^2 - |S_{22}|^2 - |\Delta|^2 > 0 \tag{2.41}$$

where $\Delta = S_{11}S_{22} - S_{12}S_{21}$.

The conditions have to be respected over the widest bandwidth to be aware of the risk of oscillations due to other sources, e.g. the turn-on or turn-off transients or harmonics originated from interferences or the noise itself.

Another tool for accurately examining the stability behavior employs the stability circles mapped on the Smith chart for either the input and the output port. For unconditional stability

of a transistor, the circles must not overlap the Smith chart. The Rollet's stability factor gives information only about the stability of the device over the frequency bandwidth, whereas the stability circles suggest the source and load impedance values that can generate instabilities.

Microwave transistors are often potentially unstable, therefore great care must be devoted to solve the problem. If the device is potentially unstable within the desired operating band, a good starting point is the stabilization of the transistor. One possibility is to employ the source degeneration technique that consists on introducing an inductive element at the transistor's source. Degeneration may be preferable to other more risky techniques for stabilization, however, its main use is for a better tradeoff between matching and noise. Usually, source degeneration just shifts the unconditional stability range and its potentiality is quite limited if not even dangerous to this end.

Another possibility is the introduction of a series or parallel resistor whose minimum value can be easily determined from the Smith chart analysis of the stability circle [4].

However, adding a stabilizing resistor degrades the performance at all frequencies and, in many cases, a frequency-selective stabilizing network may be the better choice. Simple R-L or R-C combinations may sacrifice the performances only where it is necessary to improve stability, without affecting other frequencies where the device may already be stable. The figure 2.30 shows two examples of available multi-element stabilization networks. The parallel R-C circuit (a) reduces the excessive gain of the active device at lower frequencies, thereby improving stability. The parallel resonant circuit (b) opens the branch at a desired frequency and lets the resistor cut the gain at both low and high frequencies.

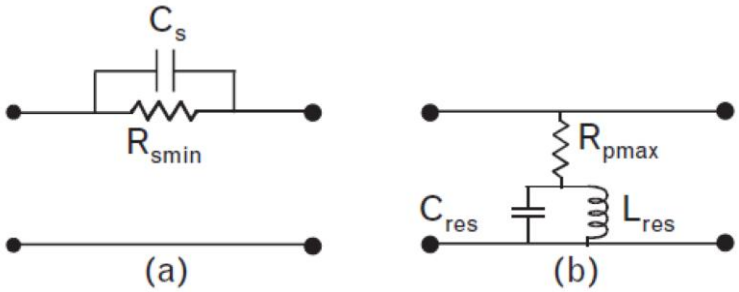

Fig. 2.30: Two examples of multi-element stabilization networks.

As a rule, it is better to avoid putting a resistor at the input side because the noise figure depends only on the input of the transistor.

After the device stabilization, the input matching network can be designed for obtaining a trade-off between the noise performances, i.e. $\Gamma_S = \Gamma_{opt}$ and a good input matching. This operation can be performed simultaneously checking the constant Γ_{noise} circles and the constant return loss circles.

Thereafter, the output matching network can be designed for obtaining a reflection coefficient as the complex conjugate of the reflection coefficient seen looking into the transistor drain, Γ_{out}, as shown in eq. (2.42):

$$\Gamma_{out} = S_{22} + \frac{S_{12}S_{21}\Gamma_S}{1 - S_{11}\Gamma_S} \tag{2.42}$$

The design of both the input and the output matching networks should be performed for the whole bandwidth. In this case, a single-frequency design with a following CAD optimization for extending the bandwidth has been implemented.

Later, the stability of the whole amplifier from D.C. to very high frequencies has to be checked.

Finally, the matching elements need to be optimized for obtaining the best trade-off among noise figure, gain, input/output return loss in order to fulfill the specifications and ensure a broadband amplifier stability.

Usually, the amplifier performances are simulated by using an electromagnetic (EM) simulator in order to accurately model the behavior of the realized amplifier. Unfortunately, the EM simulation is time-consuming if compared with the traditional CAD simulation. For this reason it is usually preceded by an accurate schematic simulation.

As cited before, to have an amplifier working properly, the transistor must be correctly biased. Therefore, a suitable bias current and voltage must be chosen and fed to the transistor ports without interfering with the signal path. To accomplish that, a bias network must be designed and connected with the gate and the drain terminals. For microwave HEMT's, a negative V_{GS} voltage and a positive V_{DS} are always required. A typical biasing network based on lumped elements is shown in Fig. 2.31:

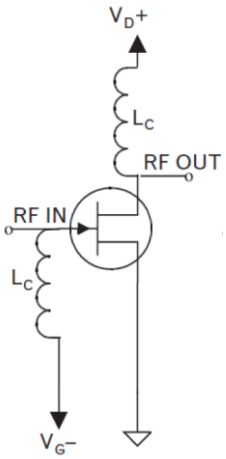

Fig. 2.31: Typical lumped element bias network.

The signal flows through RF IN path whereas gate and drain bias come from their respective DC source through a choke inductor whose task is to prevent signal from leaking into the bias branch.

For a better performance, a bypass capacitor is placed after the choke inductor, as shown in Fig. 2.32. Its tasks consists of shunting the AC components and giving the appropriate turn-on time constants at the gate and the drain terminals. Upon bias application, it is very important that the gate voltage is active faster than the drain voltage in order to avoid too large currents flowing through the device channel. Note that the DC components cannot interfere with the signal along the main line because blocking capacitors are placed both at the input and at the output of the amplifier chain.

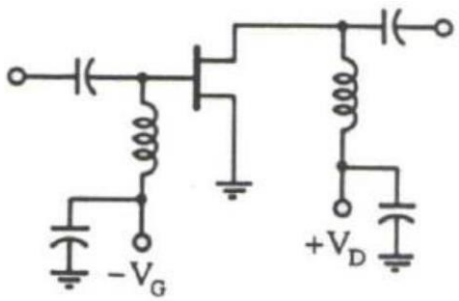

Fig. 2.32. Typical lumped element bias network with additional capacitors.

As previously underlined, at microwave frequencies the lumped elements are usually replaced by distributed elements. When adopting a distributed element design, a typical configuration for a bias network employs the so-called radial stub having a length of $\lambda/4$ at the

central frequency. It is followed by a high impedance line, also $\lambda/4$ long, that is connected to the main signal path in a section where a low impedance is seen. The behavior of the DC branch reported in Fig. 2.33, thus reproduces an RF choke plus a bypass capacitor.

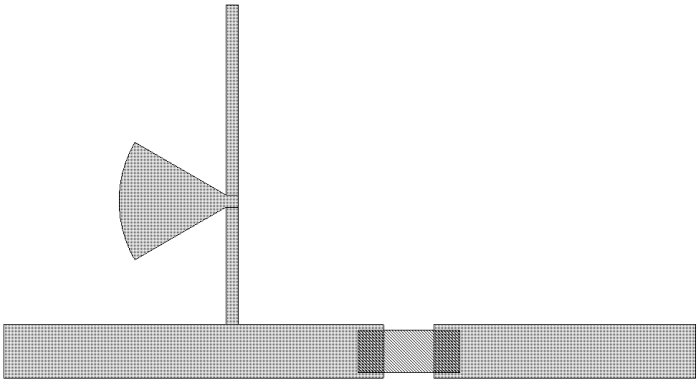

Fig. 2.33. Typical distributed element bias network.

2.3.1 Design, realization and performance of the low-noise amplifier prototype

Following the recommendations illustrated in the previous paragraph, a low-noise amplifier has been designed, realized with the internal laboratory facilities and tested. It has been realized as a hybrid microwave integrated circuit (HMIC), by using the microstrip technology. It operates within the X-band, from 9.5 to 10.5 GHz, where several applications can be found, not only in radar systems.

The employed transistor is the InGaAs HEMT MGF4953A by Mitsubishi Electric Corporation©. It has been designed to be used from C to K band amplifiers with a very low noise level (NF_{min} = 0.35 dB). It has a lead-less ceramic package that assures minimum parasitic losses. The bias point of the transistor is: V_{DS} = 2 V and I_{DS} = 10 mA.

The employed substrate is the RO3206 by Rogers Corporation© a high frequency ceramic-filled laminate reinforced with woven fiberglass. The main material characteristics are a good mechanical stability together with the surface smoothness of a non-woven PTFE laminate, for finer line etching tolerances, and with the rigidity of a woven glass PTFE laminate. Its dielectric constant is 6.15 and the dissipation factor, tanδ, is 0.0027. The design has been performed by

using the CAD environment Microwave Office® by NI AWR and its electromagnetic simulator AXIEM.

The first design step has been the check of the transistor stability over the entire bandwidth (limited by the achievable data). The transistor behavior has been reproduced by using the S- and N- parameters supplied by the manufacturer. As visible in Fig. 2.34, the transistor is not unconditionally stable over the working frequency bandwidth.

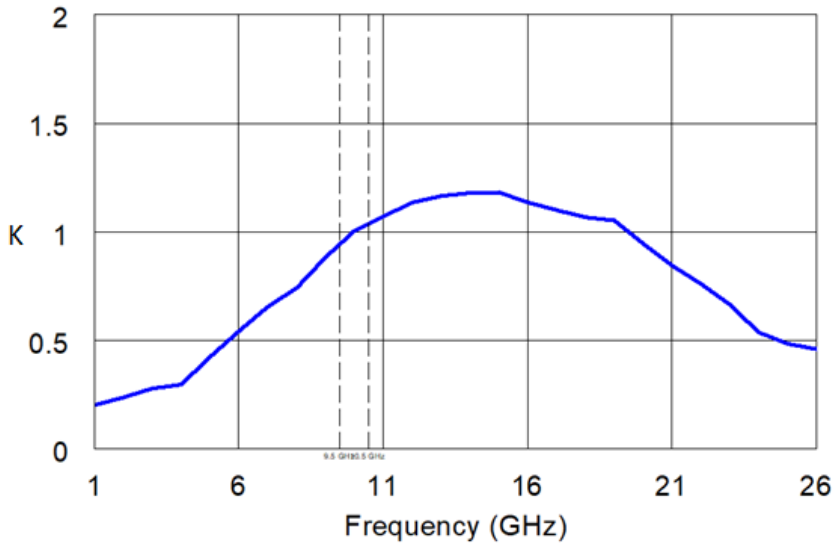

Fig. 2.34. Rollet's stability factor of the MGF4953A.

As outlined in the previous paragraph, a method for modifying the stability behavior is the source degeneration. In this case, degeneration has been used just for shifting the unconditional stability range. It consist of adding an inductive element to the transistor source, e.g. a microstrip line at the source of the MGF4953A. However, considering that the transistor source needs to be connected to the board ground, a little inductive contribution will be furnished by the via holes physical structure. Therefore, the presence of four via holes has been simulated by adding the MVIA1P model of Microwave Office®. It reproduces the behavior of the via hole as a microstrip short at the end of a transmission line. The model is composed by a transmission line, a transmission line with open-end effect and a via implemented as a lumped element series inductor and resistor. The values of the lumped elements are derived from the dimensions and resistivity of the hollow cylindrical conductor. The corresponding schematic

and the resulting Rollet's factor have been reported in Fig. 2.35, showing the achieved stability over the working bandwidth and the shift over the whole bandwidth.

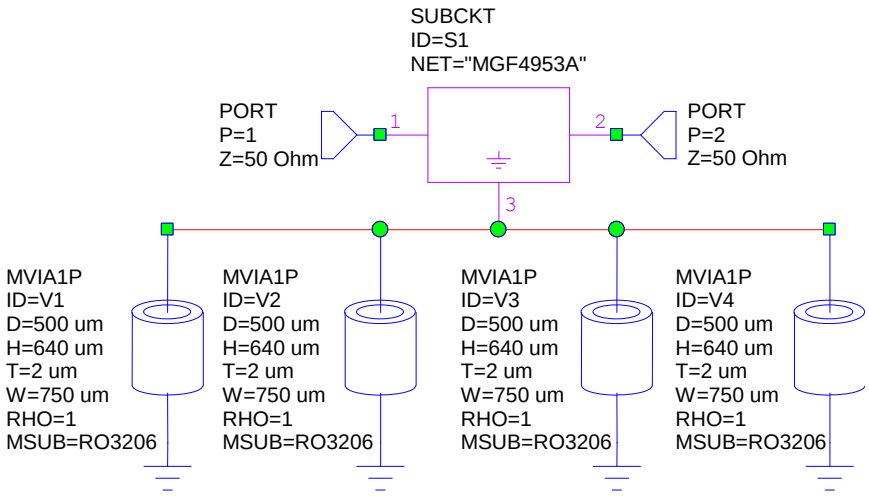

(a)

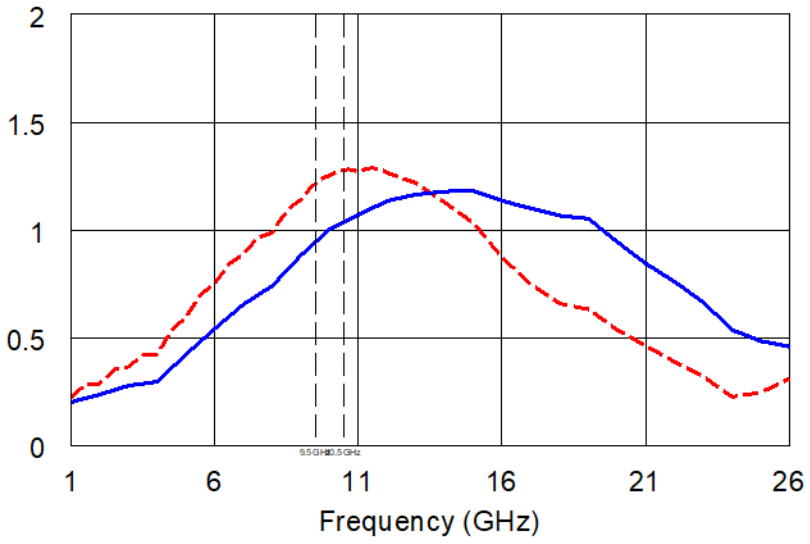

(b)

Fig. 2.35: Schematic of the transistor with source via holes (a) and Rollet's stability factor of the MGF4953A (b): without (blue) and with via holes (red).

The next step has been the design of the input and output bias networks, whose layout is reported in Fig. 2.36.

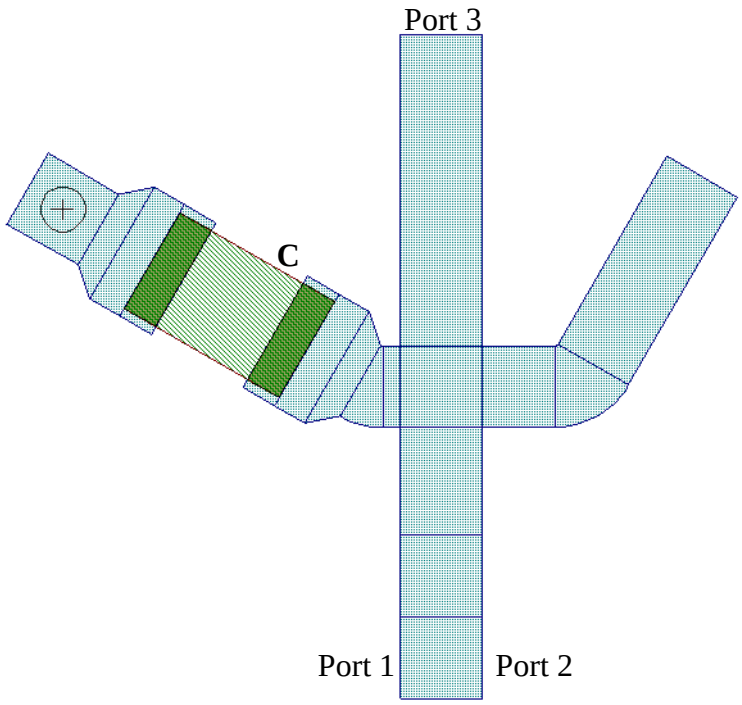

Fig. 2.36: Layout of the bias network.

The goal in designing the bias network is twofold:

- ✓ The creation of a path from port 1 to port 2 in which the X-band signal can flow without reflection.
- ✓ Avoiding the signal flow from port 1 to port 3, i.e. from the signal input to the supply network.

As reported in the previous paragraph, this purpose has been accomplished by employing a simple stub having a length of $\lambda/4$ at the central frequency, followed by a high impedance line, also $\lambda/4$ long. This solution has been preferred in place of the radial stub to limit the space occupation. It is possible to note that the stub line has been bended for space requirements. This aspect will be clear from the final layout.

The designed network has to be connected to the main signal path in a section where a low impedance is seen. In addition, to eliminate dangerous transients due to the supply section, a shunt capacitor of 1 pF has been employed. The simulations has been carried out by employing AXIEM, a 3D planar electromagnetic simulator within the Microwave Office®

by NI AWR Design Environment™ platform, that uses a method of moments solver. The performance of the bias network has been reported in Fig. 2.37.

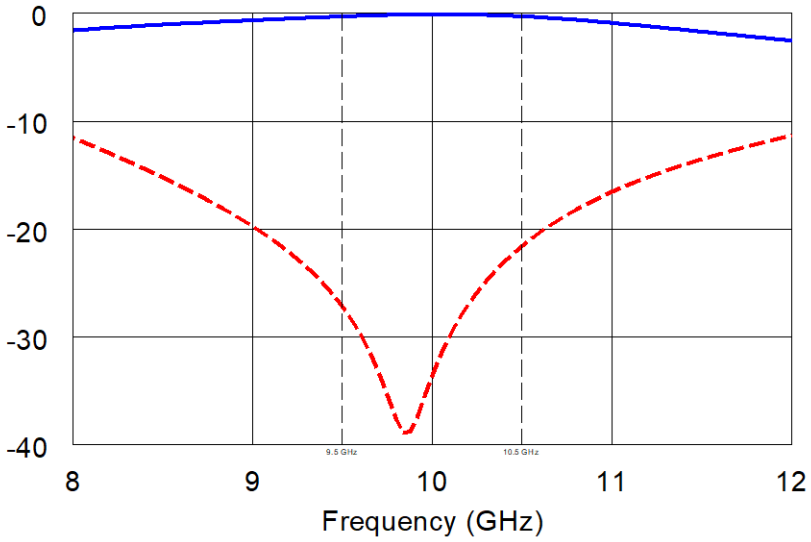

Fig. 2.37: S_{21} (blue) and S_{31} (red) of the bias network. Y-values are in dB.

Thereafter, the input matching network has been designed with the aim of reproducing the optimum reflection coefficient, Γ_{opt}, at its port 2. A double-L matching technique has been selected for obtaining a good matching over a wide bandwidth, due to its relatively low quality factor (Q). The final layout has been reported in Fig. 2.38.

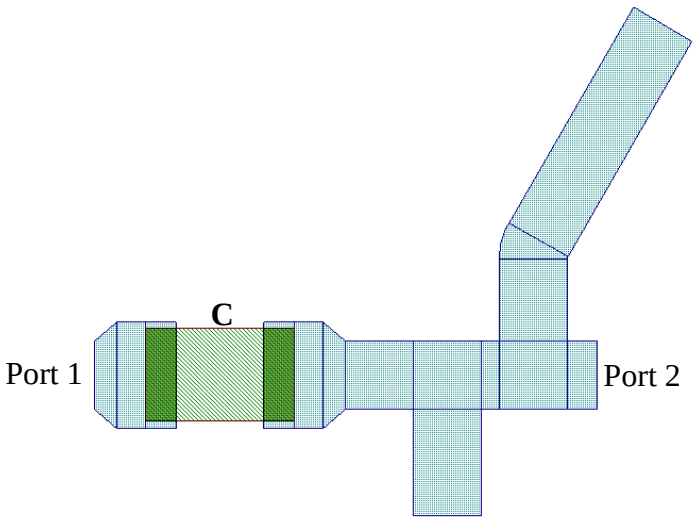

Fig. 2.38: Layout of the input matching network.

It is possible to note that one of the two stubs has been bended for space requirements. In addition, a DC-block capacitor of 1 nF has been used to prevent the DC signal going towards the input connector.

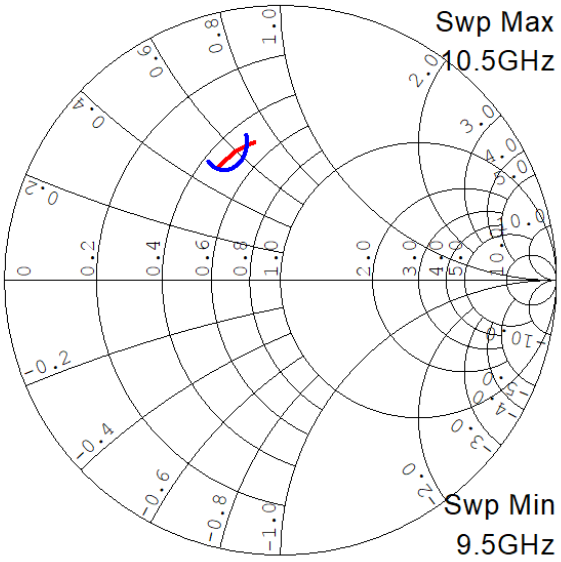

Fig. 2.39: S_{22} (blue) of the input matching network and Γ_{opt} (red) in the operating bandwidth.

Then, the output matching network has been designed following the same considerations of the input one. In this case, the purpose has been to reproduce the complex conjugate of the transistor output reflection coefficient, in order to obtain the maximum operative gain.

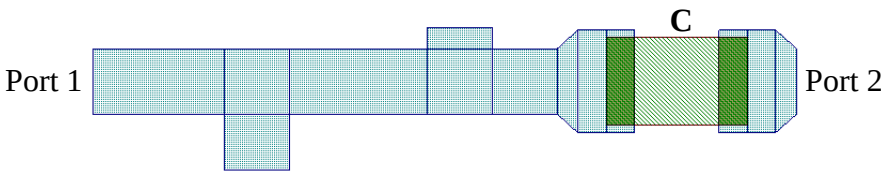

Fig. 2.40: Layout of the output matching network.

At this point, before verifying the overall performance of the amplifier, a stability check has been performed. Although the unconditional stability of the amplifier should be preferred, a different approach has been followed here. As stated before, the unconditional stability of a transistor is ensured when the stability circles do not overlap the Smith chart. If part of a stability circle lies inside the Smith chart, some impedance values exist that might generate

instability conditions. The adopted approach has been to maintain the stability circles outside the circle centered in the center of the Smith chart, with a radius defined by a certain tolerance value. Thus, the impedance values inside the tolerance circle will not generate instability.

By relaxing the stability requirements, better performances could be obtained from the other parameters of the amplifier, e.g. gain, NF, input and output RL, etc. The tolerance circle shown in Fig. 2.41, has been fixed in order to obtain a VSWR = 3.

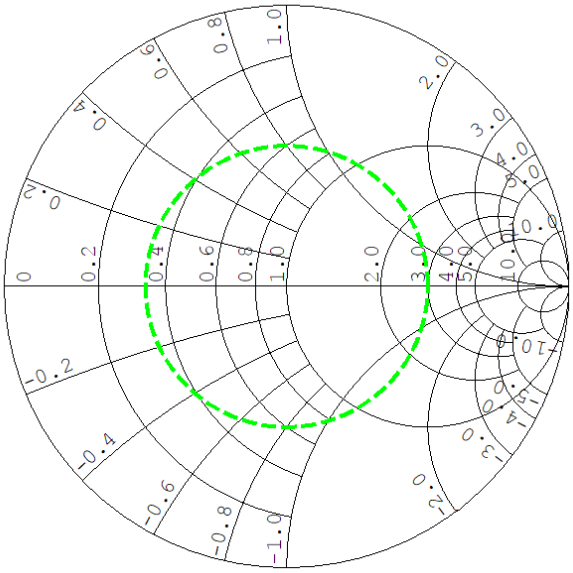

Fig. 2.41: Tolerance circle: VSWR = 3.

The adopted solution has been the employment of frequency-selective resistors. As visible in Fig. 2.42, a resistor with a series $\lambda/2$ open-circuit stub at the frequency of 10 GHz have been added to the lower section of both the bias networks. Thus, the network behaves as an open circuit at the frequency of 10 GHz. Away from this frequency, the effect of the resistor increases and the stabilizing effect of the resistor takes place.

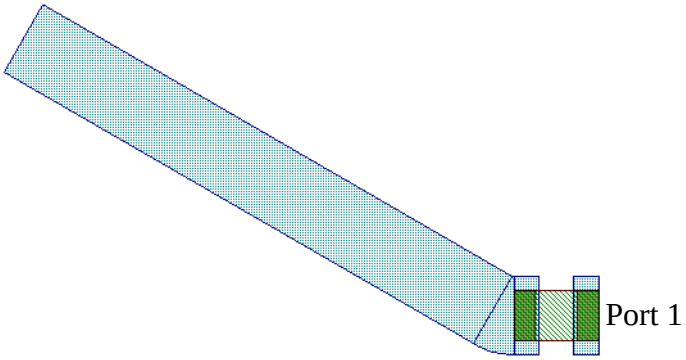

Fig. 2.42: Frequency-selective stabilization network.

Again, the stub has been bended for space requirements. The input and output stability circles together with the tolerance circle have been reported in Fig. 2.43. A tolerance circle equivalent to a VSWR = 7 has been finally obtained.

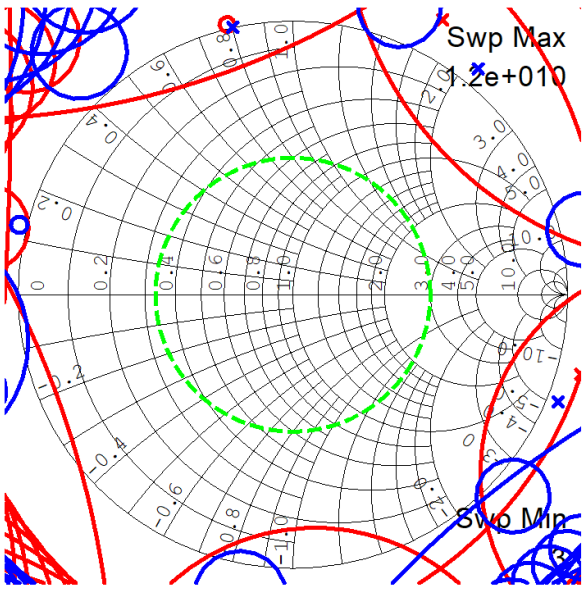

Fig. 2.43: Input (blue) and output (red) stability circles together with the tolerance circle (green).

As the last step of the design, an electromagnetic optimization has been performed for obtaining the best possible values of NF, gain and input and output return loss. The final amplifier layout that minimizes the overall occupied space is reported in Fig. 2.44. It has a length of 39 mm and a width of 15 mm. It is possible to note the additional pad, included for connecting the power supply ground. In addition, to insert the employed connectors (two

Southwest Microwave, Inc. ® 2.92 mm JACK End Launch Connectors), two pads have been designed, the input and output feed lines have been extended and a taper has been introduced. Finally, some microstrip lines have been bended to avoid crossing with other lines or with the two connectors.

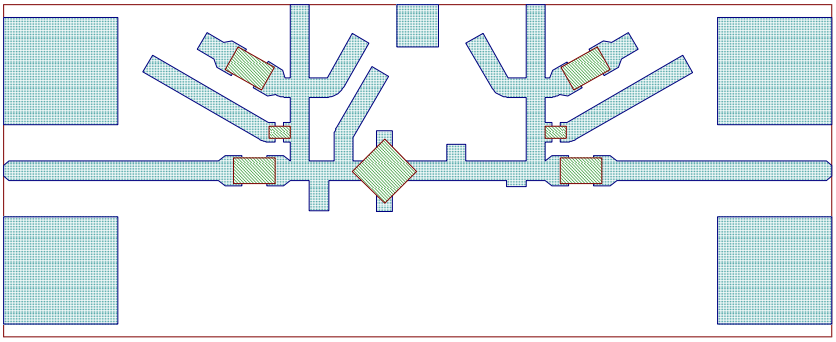

Fig. 2.44: Final layout of the low-noise amplifier.

In Fig. 2.45, the EM simulated LNA performances are reported. The amplifier NF is below 0.7 dB, the gain is above 11.4 dB and both the S_{11} and the S_{22} are higher than -10 dB.

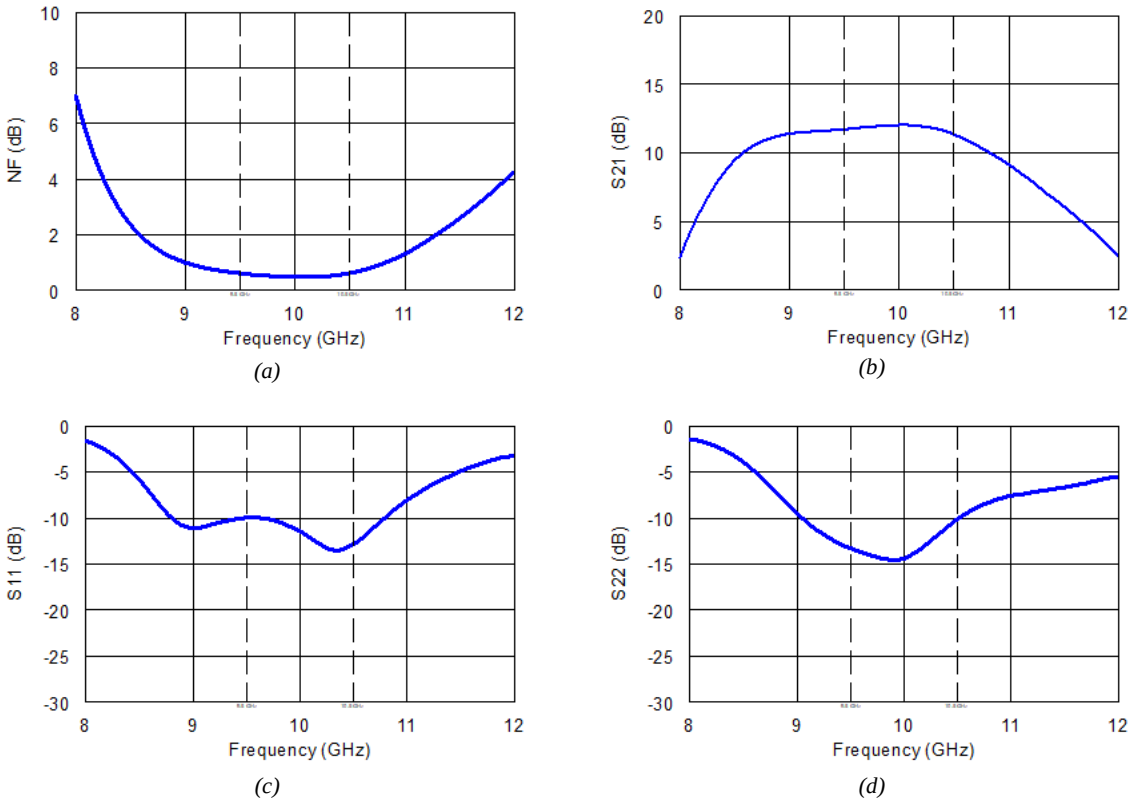

Fig. 2.45: LNA's performance: (a) NF, (b) S_{21}, (c) S_{11} and S_{22}. Y-values are in dB.

Then, the circuit has been prototyped using a high precision mechanical plotter S103 Protomat LPKF. It consists of a base plate and a machining head that can be moved along both axes with the aid of an X/Y motion system. The machining head can also be lowered thus offering two basic processing possibilities. As a first option, a channel can be milled with a milling cutter in a piece of base material fastened to the base plate by moving the lower machining head. As a second option, a hole can be drilled in the base material by lowering the machining head. It uses a moving speed of 150 mm/s and a motor speed of 40000 to 100000 min-1 with a resolution of 0.25 μm. The plotter is controlled by using a software interface.

After the realization and the components assembly, a brass slab has been place under the substrate to increase the stiffness of the LNA. Indeed, the very thin substrate is quite fragile and it can break especially when tightening the LNA connectors with external cable connectors. A picture of the LNA prototype is reported in Fig. 2.46.

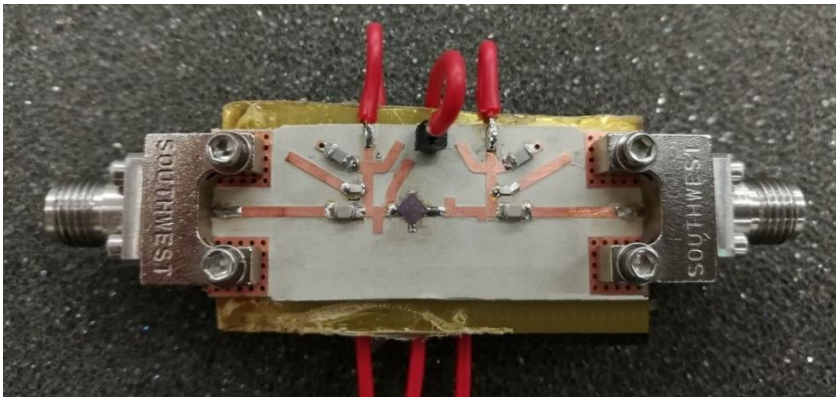

Fig. 2.46: Picture of the LNA prototype.

As a final step, the performance of the low-noise amplifier has been measured. In Fig. 2.47, a comparison between the simulated and measured data is reported. Regarding the noise figure, it is necessary to consider that the effects of the connectors have not been simulated. Indeed, since each connector has S_{21} equal to -1 dB at 10 GHz, it is necessary at least to take into account the additional noise figure of 1 dB related with the input connector, thus resulting in an good correspondence between simulated and measured data. The same consideration for both connectors needs to be made with respect to the gain, whose measured values have been better than the simulated ones. Unfortunately, a degradation of the input and output matching parameters has occurred. It could be either due to the handmade placement of the components or to the tolerances of the data used for reproducing the behavior of the components, e.g. the

active device, the resistors, or the capacitors. Of course, these aspects will be deeply analyzed and hopefully solved in the next version of the amplifier prototype in progress. In the next prototype version, suitable layout structures/pads will be added for possible tuning. Indeed, one of the key advantage of designing a HMIC (compared with the MMICs design) is the possibility of correcting and improving the quality of the design with a relatively low cost and time.

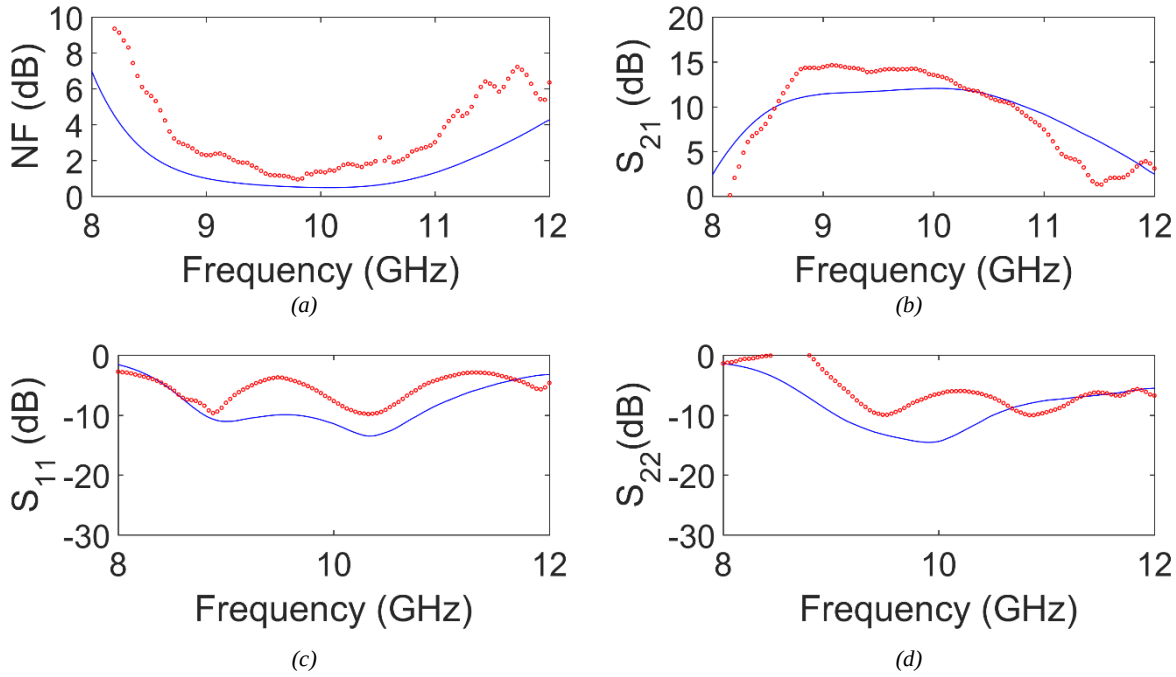

Fig. 2.47: LNA's simulated (blue solid line) and measured (red dotted line) data: (a) NF, (b) S_{21}, (c) S_{11} and (d) S_{22}.

2.3.2 Analysis of low-noise amplifiers under light exposure

The present paragraph is based upon a comparative study of the light-induced changes in low-noise amplifier performances employing the AlGaAs/GaAs HEMT's with three scaled gate widths, already described in this Chapter. The LNA's have been designed to operate in the 7.5-8.5 GHz range exploited not only in radars but also in point-to-point radios, point-to-multi-point radios, VSAT and satellite communication applications [24]. On the basis of measured results, a low-noise amplifier was designed for each device type in dark conditions. The obtained results could only be considered as a theoretical study because the LNA analysis has been carried out at simulation level. The working frequency is also different from that used in paragraph 2.3.1 because of the different employed devices. The design was carried out employing Microwave Office® by NI AWR Design Environment™ with performance goals

centered in the 7.5 GHz to 8.5 GHz frequency band. Alumina (ε_r = 9.9, tan δ = 0.0002, h = 250 μm) was adopted for the substrate with 5 μm-thick gold metallization. Modeling of the bonding wires was accomplished by means of the resident multilevel bond wire model BWIRES2 that define bonding scheme parameters in compliance with EIA/JEDEC Standard No. 59. The basic structure of the circuit comprises a lossy stabilization network on the gate side of the transistor, a stabilization resistor on the drain side, input/output bias networks and input/output matching networks. The structure was first tailored to the design of a LNA employing the smallest device. Then, the same topology was optimized to the performance of the larger devices by changing the passive element values, reported in Table 1. The schematic of the LNA designed for the 100 μm HEMT is shown in Fig. 2.48.

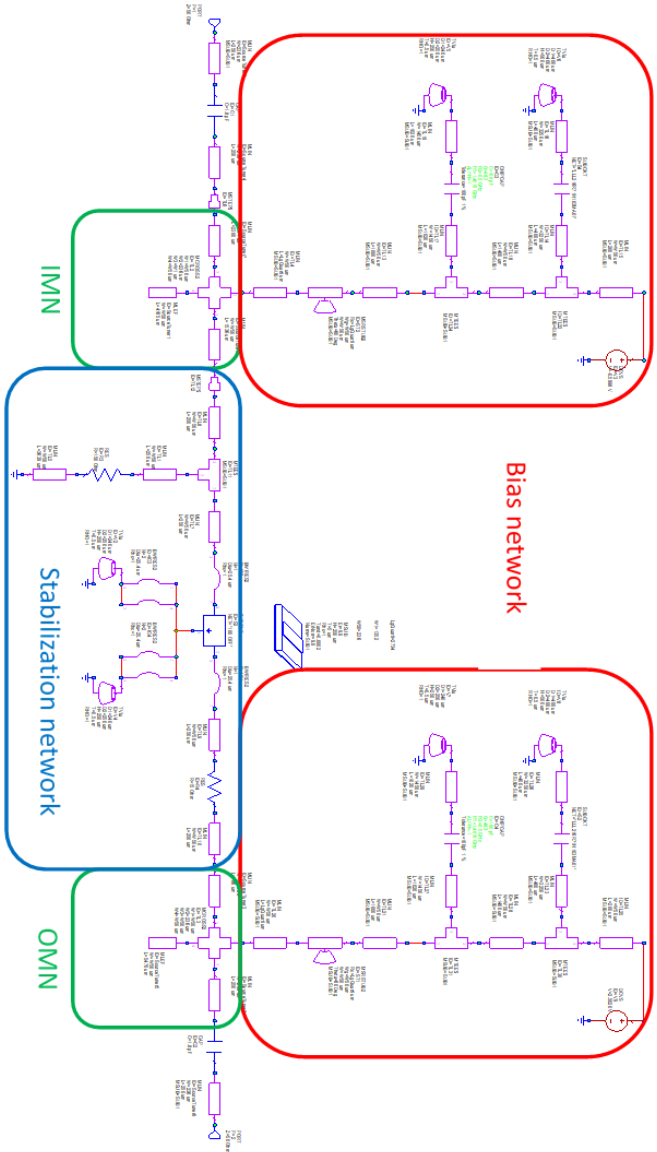

Fig. 2.48. Schematic of the LNA operating in the 7.5-8.5 GHz frequency band. The performance was optimized for dark condition of the 100 μm HEMT [24].

As expected, the amplifier performances depend on the device gatewidth. Either input or output matching levels stay lower than -10 dB within the chosen frequency band for all LNA's. The stability was monitored either inside or all over outside the operating band by checking the value of the μ coefficient which must be higher than unity to ensure stable operation. Due to the required stabilization of the amplifiers, we noticed that the reflection coefficient "seen" at the device input was not really close to Γ_{opt} within the operating band, i.e., broadband stabilization was achieved at the expense of the noise mismatch.

It is also to be noted that, for maintaining the structure unchanged, in-band stability has been provided by increasing the value of the drain resistor thus hindering the higher gain available from the larger devices. As a consequence, the 300 μm - based LNA has the lowest gain, despite the fact that the isolated device shows the top values of $|S_{21}|$ as reported in the graphs in Fig. 2.49.

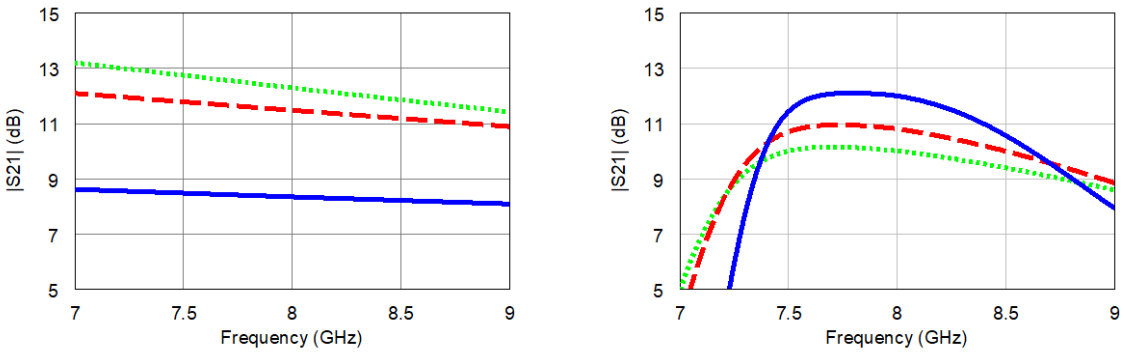

(a) *(b)*

Fig. 2.49. Comparison between (a) device $|S_{21}|$ and (b) LNA $|S_{21}|$ in the 7 - 9 GHz frequency range for dark operation. Devices are: 100 μm (blue solid line), 200 μm (red dashed line), and 300 μm (green dotted line) [24].

Concerning noise figure, the amplifiers based on the smaller (100 and 200 μm) transistors were characterized by the lowest mid-band values, whereas the largest device offered a more equalized performance as recognizable in Fig. 2.50.

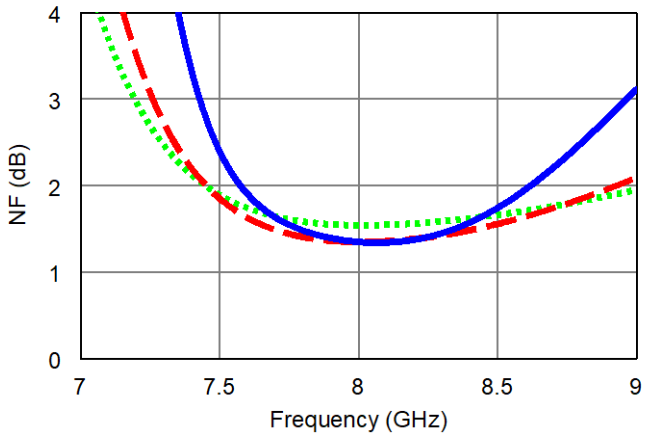

Fig. 2.50. Noise figure of the LNA's optimized in the 7 - 9 GHz frequency range for dark operation. Devices are: 100 μm (blue solid line), 200 μm (red dashed line), and 300 μm (green dotted line) [24].

The performance of the low-noise amplifiers was then analyzed under light exposure. Regarding noise figure behavior, it was noted that a maximum increase of 1.28 dB (at 7.5 GHz) occurred for the 100 μm HEMT-based LNA since the smallest device was the most sensitive to light effect, whereas decreasing degradation was observed for the remaining amplifiers as shown in Fig. 2.51.

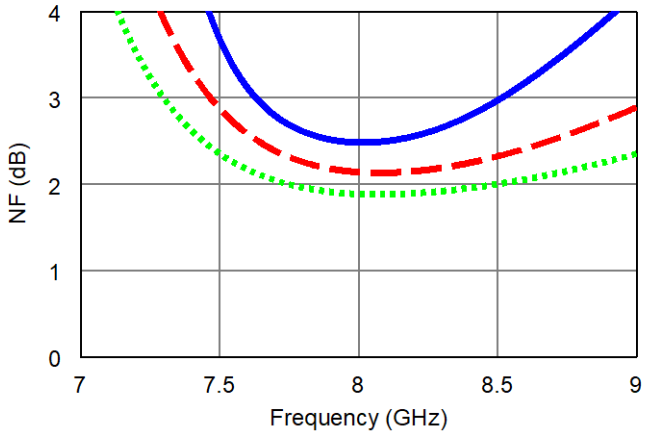

Fig. 2.51. Noise figure of the illuminated LNA's in the 7 - 9 GHz frequency range. Devices are: 100 μm (blue solid line), 200 μm (red dashed line), and 300 μm (green dotted line) [24].

In general, these noise figure values were lower than expected if compared to: (a) the F_{min} variations of the isolated devices seen in Fig. 2.9b; (b) the changes of Γ_{opt} under light exposure; (c) the losses added by the circuit elements. All the above aspects should have led to a higher degradation of the noise figure of the illuminated LNA's because of the increased noise levels

produced by charge generation, the significant increase of the gate current, the thermal noise contribution due to lumped and distributed lossy elements and the degradation of noise mismatch. On the other hand, by looking at the reflection coefficient Γ_{mn} "seen" by the device input for the three LNAs, we observed that in all cases it tends to be closer to the values of Γopt illuminated, especially in the upper frequency band, as shown in the plots in Fig. 2.52.

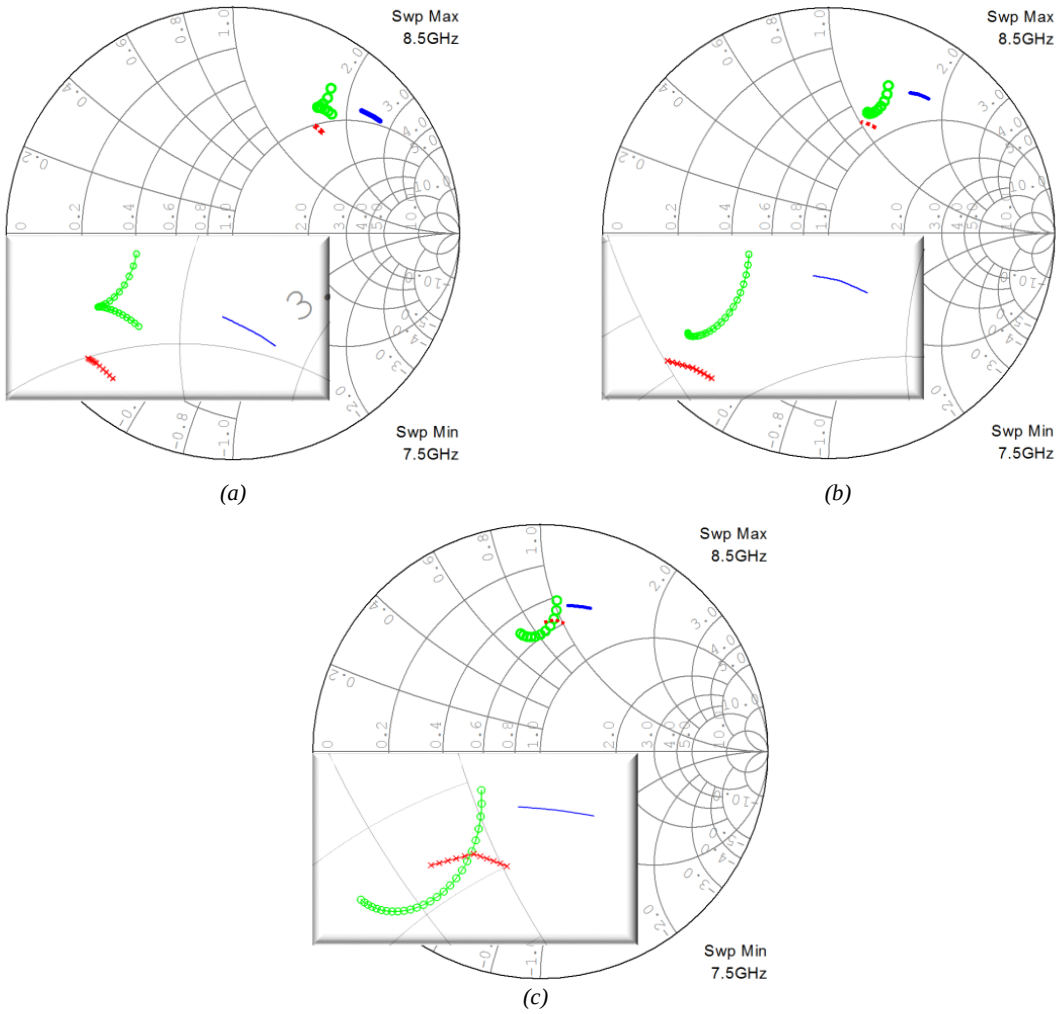

Fig. 2.52: Comparison among Γ_{opt} dark (blue solid line), Γ_{opt} illuminated (red dotted line) and Γ_{mn} reflection coefficient seen by the device input (green circle) in the 7.5 – 8.5 GHz frequency range for the (a) 100 μm, (b) 200 μm, and (c) 300 μm device LNA [24].

It should be underlined that Γ_{mn} is the same with and without optical illumination, since the three devices with and without light have been embedded in the same three circuits.

This would explain the mitigation of the light effects on the noise figure performance. It is possible thus concluding that the effects of illumination are beneficial to the level of noise matching.

Concerning gain, it was observed that despite a slight increase of $|S_{21}|$ in the illuminated devices has been reported in Fig. 2.53a, the overall effect of light exposure in the amplifiers was a decrease of gain clearly recognizable in the plot in Fig. 2.53b.

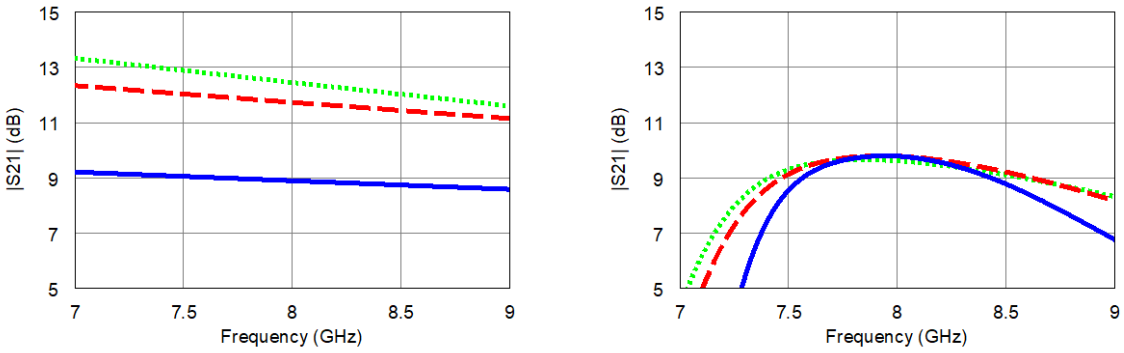

(a) *(b)*

Fig. 2.53. Comparison between (a) device $|S_{21}|$ and (b) LNA $|S_{21}|$ in the 7 - 9 GHz frequency range under light exposure. Devices are: 100 μm (blue solid line), 200 μm (red dashed line), and 300 μm (green dotted line) [24].

This effect was quite remarkable in the 100 μm HEMT-based LNA and much less sensitive in the 300 μm HEMT-based LNA, thus leading to a very similar performance of all the amplifiers within the operating band.

This behavior seems to be related to the changes occurring under exposure in the values of the device $|S_{22}|$. Such variations are more pronounced for the smallest transistor as shown in Fig. 2.54.

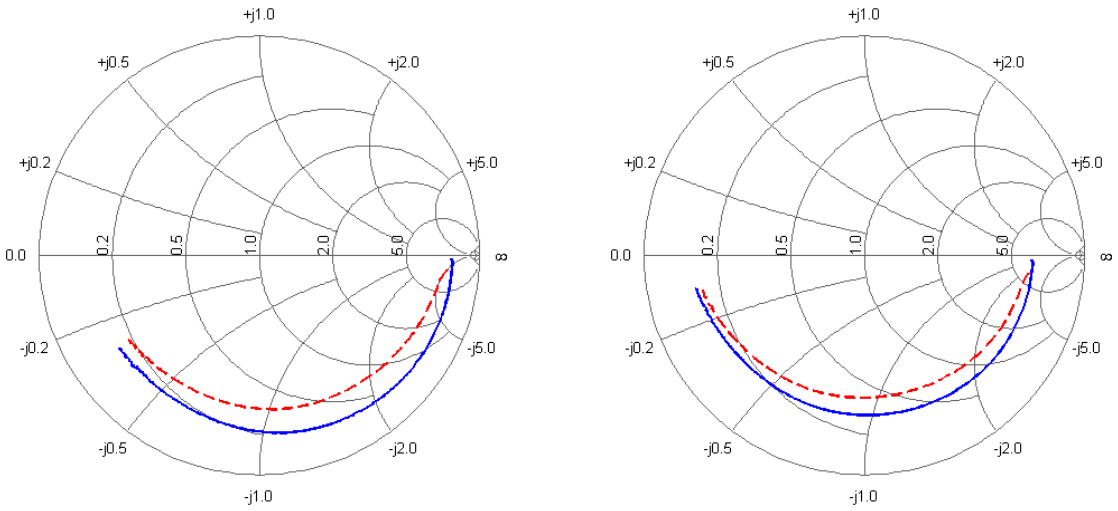

(a) *(b)*

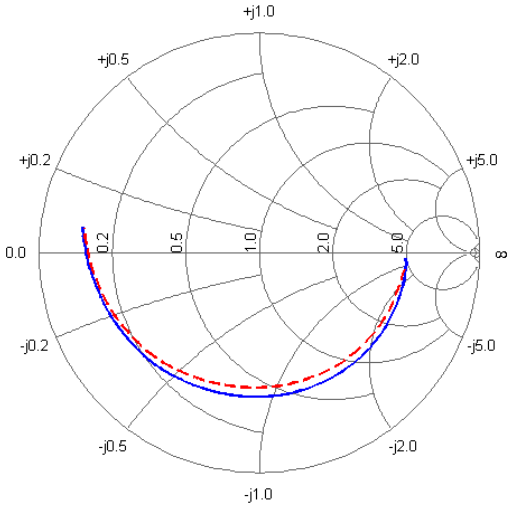

(c)

Fig. 2.54: Comparison between S_{22} dark (blue) and S_{22} illuminated (red) in the 2-18 GHz frequency range for the (a) 100 μm, (b) 200 μm, and (c) 300 μm device, respectively [24].

The light exposure thus promotes a mismatch at the device output port since the output matching network was optimized for dark mode operation.

The amplifier stability was sensibly enhanced in each case within the operating band, as shown in the graphs in Fig. 2.55.

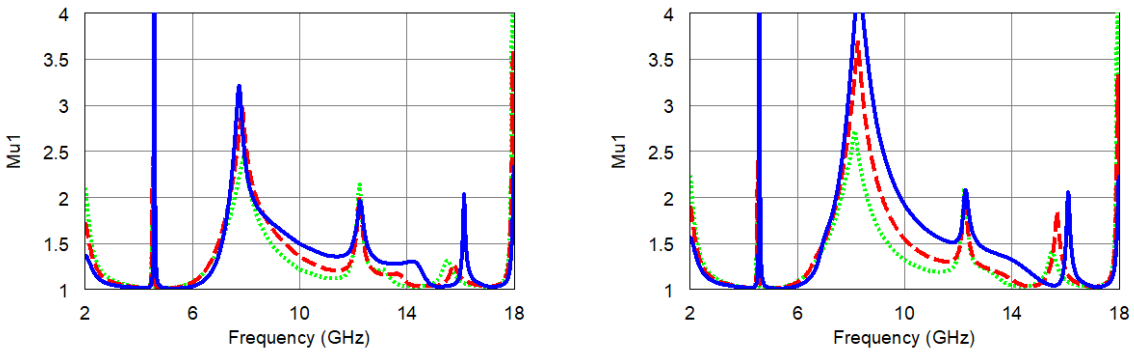

(a) *(b)*

Fig. 2.55. Comparison between LNA broad-band stability performances in (a) dark operation; (b) illuminated condition. Devices are: 100 μm (blue solid line), 200 μm (red dashed line), and 300 μm (green dotted line) [24].

For this analysis, the geometric stability factor μ_1 has been employed. It measures the radius from the center of the Smith Chart (Z_0) to the nearest unstable point in the output load plane. The larger it is (above one), the more margin the design has to variations in processing. The

necessary and sufficient condition for unconditional stability of the two port is that $\mu_1 > 1$. The stability factor can be computed from eq.

$$\mu_1 = \frac{1 - |S_{11}|^2}{|S_{22} - S_{11}{}^{*}\Delta| + |S_{12}S_{21}|} > 1 \tag{2.43}$$

where $\Delta = S_{11}S_{22} - S_{12}S_{21}$.

The results for the LNAs, in terms of scattering parameters, have been confirmed also by simulating the behavior of two gain hybrid amplifiers to better put in evidence the light effects [42]. Again, the obtained results could only be considered as a theoretical study because the amplifier analysis has been carried out at simulation level. They are optimized in the 7.5-8.5 GHz frequency band according to the dark parameters of two pseudomorphic HEMT's having 0.15 μm gate length and 100-200 μm gate widths. The design has been implemented by using the three-dimensional (3-D) planar electromagnetic AXIEM™ software, available in the NI AWR Design Environment platform. In addition, the EM analysis of the effects of the coaxial-to-microstrip connectors has been addressed for a better evaluation of their impact on the electrical behavior of the amplifiers. For the analysis of the effects of the coaxial-to-microstrip connectors, the arbitrary 3-D finite element method Analyst™ software has been employed. An alumina substrate ($\varepsilon_r = 9.9$, $\tan\delta = 0.0002$, h = 250 μm) has been adopted with 5 μm-thick gold metallization. The amplifier gain is higher than 14 dB, always ensuring a good match over the entire bandwidth at both input and output ports, not less than -11 dB. The stability was monitored both inside and all over outside the operating band by employing the standard μ coefficient. The basic structure of the circuit includes a stabilization resistor on the drain side of the transistor, a lossy stabilization network on the bias side networks, input/output bias networks, input/output matching networks and input/output coaxial-to-microstrip connectors. The first step in the design procedure has been the creation of the circuit schematic by using built-in microstrip blocks. Thereafter, the EXTRACT block (an Axiem feature) has been employed associating the layout cells of the circuit to the previously set up electromagnetic (EM) simulation. Finally, the EM results are automatically merged back into the schematic by replacing the element built-in models and the simulation of the entire schematic is performed. The extracted 3D EM layouts are shown in Fig. 2.56.

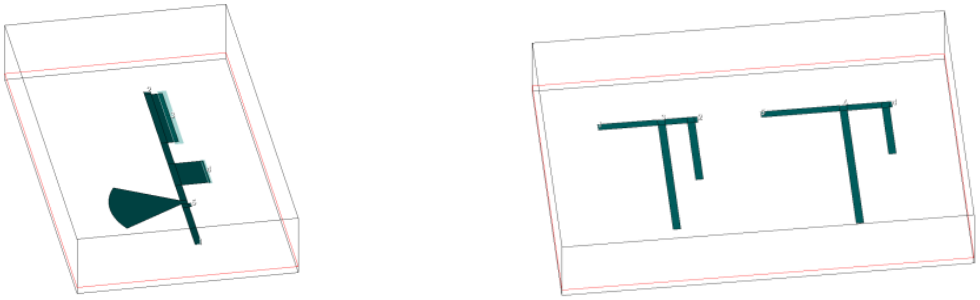

(a) *(b)*

Fig. 2.56. (a) 3-D layout of the bias and (b) matching networks [42].

Thereafter, a SMA connector model has been properly modified for a more accurate prediction of the amplifier performance. The employed elements are Southwest Microwave, Inc. ® 2.92 mm JACK End Launch Connectors, that allow a fast connection of the ports without any soldering. Since the main discontinuity occurs in the transition between the central pin of the connector and the microstrip line, the bulk connector structure of the transition blocks has not been included in the 3-D model. The 3-D layout of the connector is reported in Fig. 2.57.

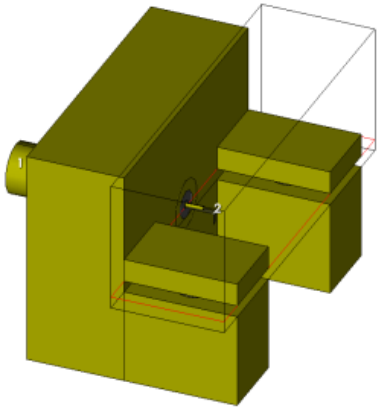

Fig. 2.57. 3-D layout of the connector [42].

The observed characteristics of the amplifiers are gain level, bandwidth, input/output return loss and stability degree. In the reported plots, the effect of the connectors has shown to cause a slight degradation of the simulated parameters. Regarding the parameters S_{11} and S_{22}, the light exposure shows different effects on the two different devices. In the 100 μm amplifier, it promotes a mismatch at the input whereas it improves the matching at the output. An almost opposite behavior has been noticed for the 200 μm device. The more interesting observations

concern the gain of the amplifiers. In both cases, the gain decreases with light exposure thus leading to the conclusion that the optical signal can be used to adjust the amplifier performance. The scattering parameters of the 100 μm and 200 μm amplifiers in dark conditions and under light exposure are respectively reported in Fig. 2.58 and Fig. 2.59.

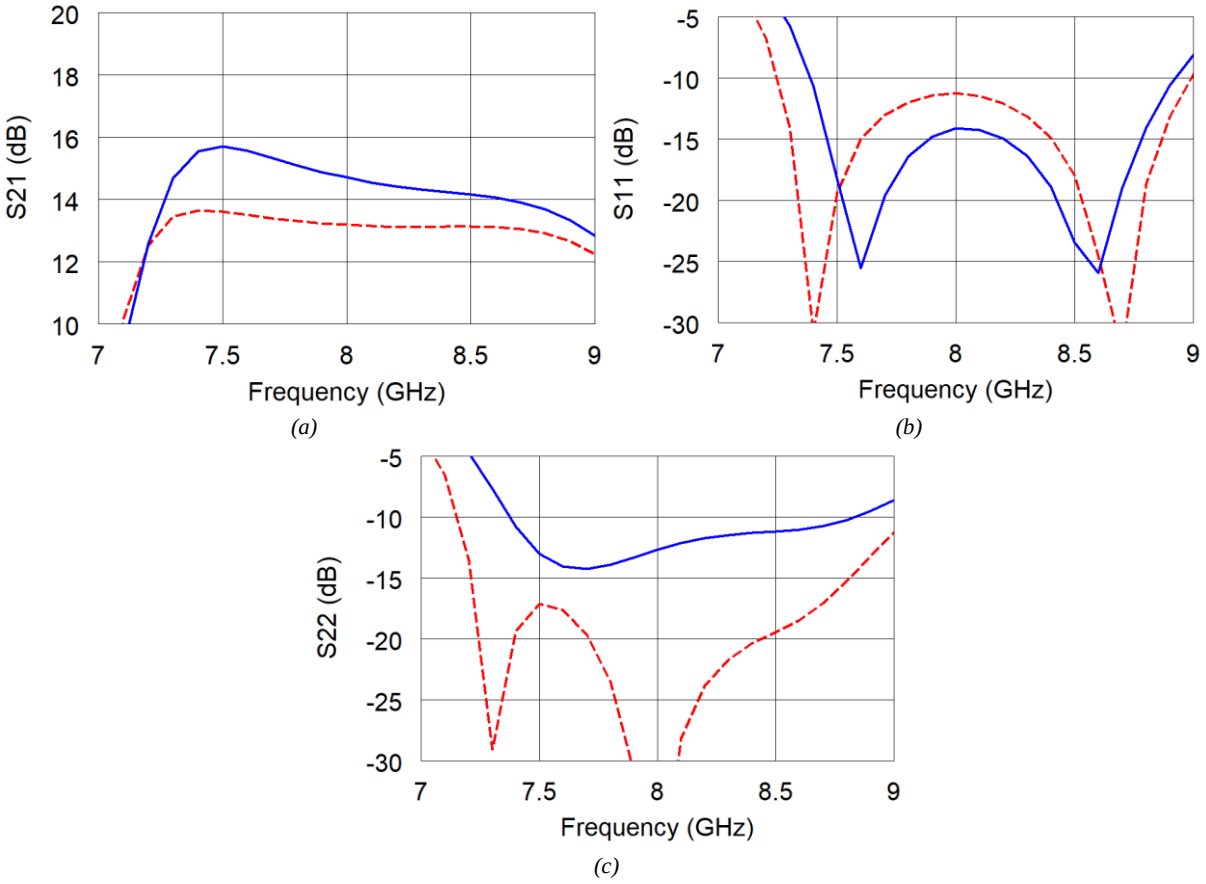

Fig. 2.58: (a) S_{21}, (b) S_{11}, (c) S_{22} of the 100 μm amplifier in dark (blue) condition and light exposure (red) [42].

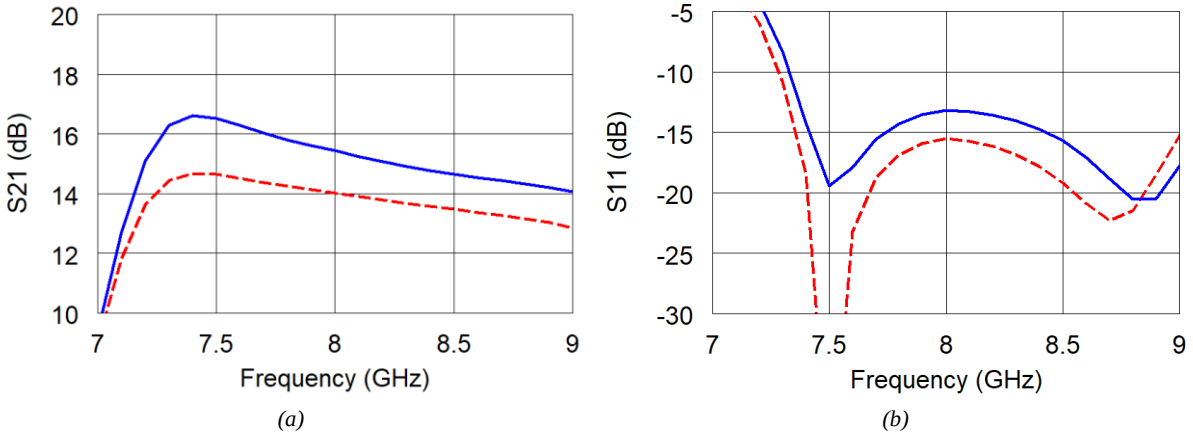

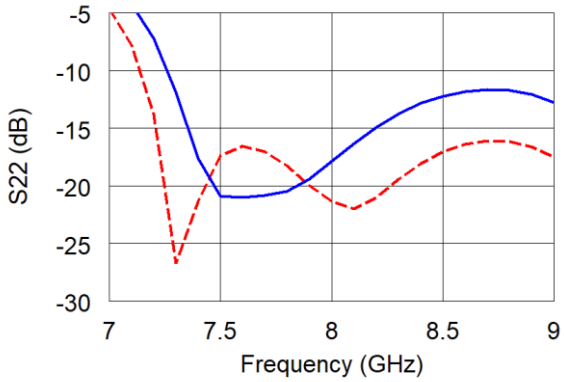

(c)

Fig. 2.59: (a) S_{21}, (b) S_{11}, (c) S_{22} of the 200 μm amplifier in dark (blue) condition and light exposure (red) [42].

2.3.3 LNA prototype under light exposure

In the previous paragraph, a comparative analysis among the dark vs light performances of three low-noise amplifiers has been presented [24]. Although the noise figure degradation due to light absorption confirmed the effects on the single device as noticed in [14], a degradation of the LNA gain was also observed.

This finding is opposite to the common belief that by exposing an amplifier to a light stimulus, a substantial improvement of the performance can be obtained as a consequence of the increase of both the transconductance and the $|S_{21}|$ parameter, typically encountered under illumination. In [43], evidence of gain improvement under light exposure was shown. Particularly, the possibilities to optically control a S-band GaAs monolithic amplifier are evidenced biasing the transistor near the pinch-off.

In the previous paragraph, the behavior of the LNA's has been just simulated by employing the measured data of the devices under on and off light exposure. Therefore, the obtained results could only be considered as a predictive study. In addition, to my best knowledge, in the scientific literature, only a paper was found that confirms the striking result of the gain decrease in a LNA under illumination [44].

In this paragraph, an extensive experimental investigation of the behavior of a microwave low-noise amplifier under optical illumination is presented [45].

It has been assessed that the LNA performance is significantly influenced by the light exposure with optical effects more pronounced at higher wavelengths for a fixed incident

power. Upon applying the recommended bias conditions of the sensing amplifier, the main changes consist of a degradation of the noise figure and gain. As opposite to this, an overall performance enhancement is clearly recognizable with the amplifier biased at the transistor pinch-off. The results obtained in present paragraph fully confirm the theoretical analysis previously carried out by employing different devices and LNA design.

The employed device and the designed LNA are those described in paragraph 2.3.1. They are different from those used in paragraph 2.3.2, so that the relevant findings can be considered of general validity.

The top side of the device package has been removed thus allowing the interaction with a light beam. The un-packaging of the transistor caused a substantial worsening of the overall amplifier performance. A picture of the low-noise amplifier with the un-packaged pHEMT, has been reported in Fig. 2.60.

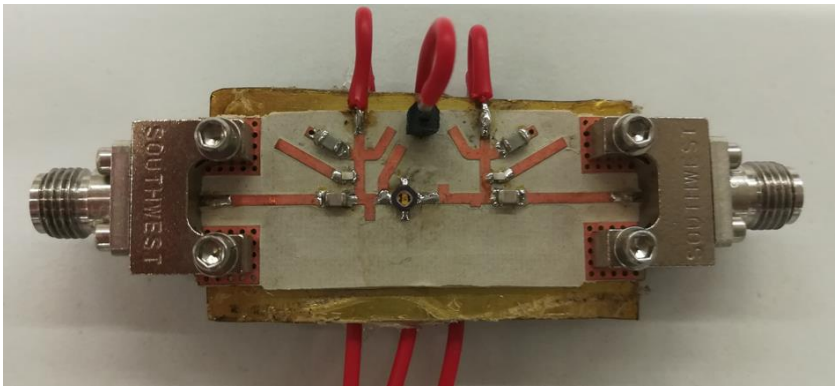

Fig. 2.60: Picture of the low-noise amplifier with the un-packaged pHEMT.

The scattering parameters and the noise figure of the LNA have been measured without and under light exposure for two different light wavelengths (635 nm and 532 nm) and for different optical power levels.

The experimental tests have been performed by first biasing the LNA at the recommended bias conditions to ensure the proper operation of the transistor in the active region, then by biasing it at the transistor pinch-off. This last choice has been made both to allow a proper comparison with the already published results and to address the feasibility of the optical control in LNA's.

To perform the S- and N- parameter measurements, an Agilent E8364A (0.045 ÷ 50 GHz) vector network analyzer and an Agilent N8975A (10 MHz ÷ 26.5 GHz) noise figure analyzer have been employed.

An optical set-up has been properly designed for exposing the device to two laser beams with wavelengths of 635 nm (red light) and 532 nm (green light) respectively, without removing the LNA. Moreover, the set-up has been calibrated for illuminating the amplifier with different optical power levels.

A properly designed optical set-up has been used to expose the device to two laser beams with wavelengths of 635 nm (red light) and 532 nm (green light) respectively, without removing the LNA. To this purpose, the laser beams are deflected by a mirror installed on a micrometric mount and focused by a lens on the sample surface. A removable rotating mirror works to switch the wavelengths and adjust the beam direction. The optical powers of the two laser sources have been calibrated in order to match the light intensity which reaches the device. The setup also is equipped with a neutral step variable optical filter that is used to change the laser power impinging onto the sample. In Fig. 2.61, a picture of the optical set-up has been reported.

Fig. 2.61: Optical set-up.

The first set of measurements has been performed by biasing the LNA at the recommended bias conditions of the transistor, i.e. V_{DS} = 2 V and V_{GS} = - 0.21 V (I_{DS} = 10 mA). Its

performance has been tested in the frequency range from 8.5 GHz to 10.5 GHz. The amplifier has been exposed to different optical power levels, i.e. 3 mW, 5.5 mW and 10 mW, respectively.

Fig. 2.62 shows the performance of the noise figure NF without and with illumination at the wavelength of 635 nm

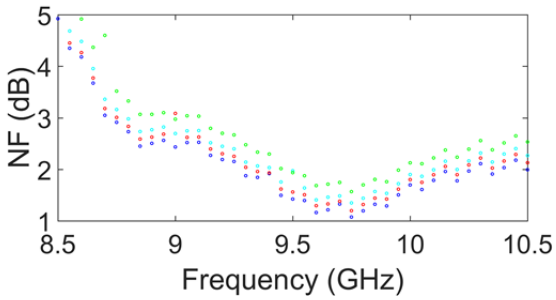

Fig. 2.62: NF without (blue) and with illumination at the optical power levels of 3 mW (red), 5.5 mW (cyan), 10 mW (green) at the bias point V_{DS} = 2 V and V_{GS} = - 0.21 V. The light wavelength is 635 nm.

As previously enlightened, the results are in agreement with the theoretical expectation. The light absorption evidently activated the charge generation, thus leading to a remarkable increase of the noise figure. It could be observed that the higher the optical power, the higher the degradation of the noise figure.

In Fig. 2.63, the comparison of the S-parameters S_{21}, S_{11} and S_{22} without and with illumination at the wavelength of 635 nm is reported for different optical power levels.

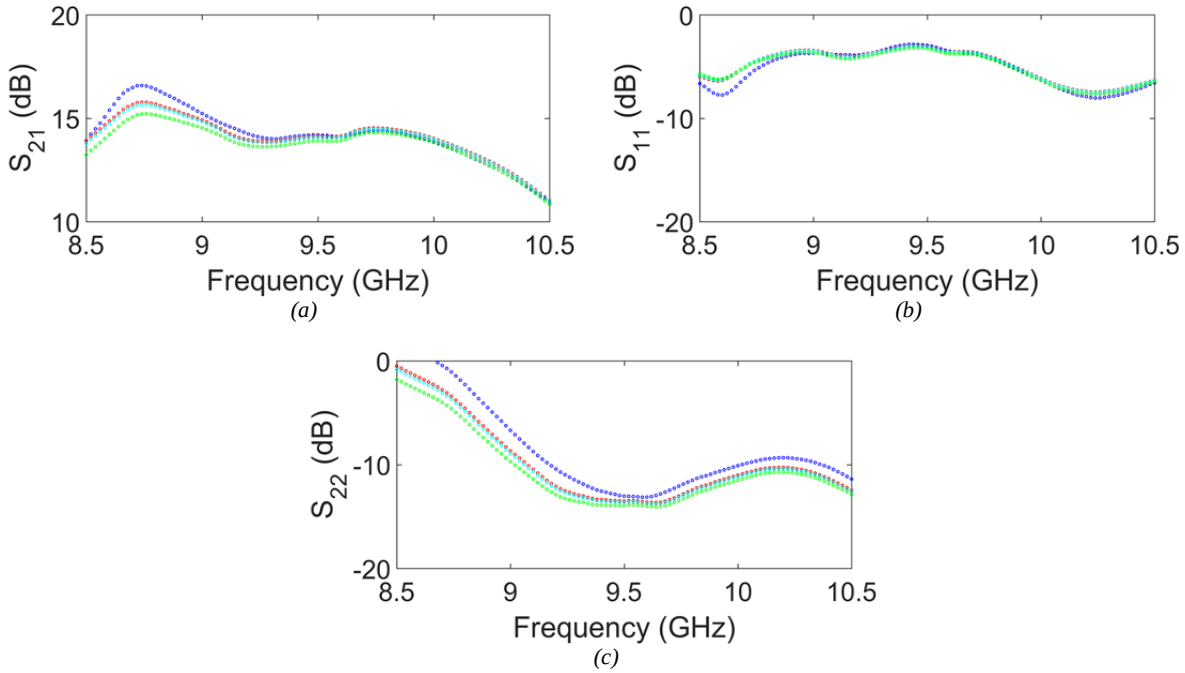

Fig. 2.63: S-parameters of the LNA (a) S_{21}, (b) S_{11}, (c) S_{22} without (blue) and with illumination for optical powers of 3 mW (red), 5.5 mW (cyan), 10 mW (green) at the bias point V_{DS} = 2 V and V_{GS} = - 0.21 V. The light wavelength is 635 nm.

Although a clear trend in the input matching parameter S_{11} under illumination is not recognizable, we observed a net improvement of the output matching parameter S_{22}. Instead, it is worth noting the decrease of S_{21} at increasing optical power levels.

This result suggests to analyze the scattering parameters of the devices reported in [14] under a different viewpoint, by considering the expression of the maximum stable gain MSG, reported in eq. 2.44:

$$MSG = \left|\frac{S_{21}}{S_{12}}\right| \left(K - \sqrt{K^2 - 1}\right) \tag{2.44}$$

where K is the Rollet's stability factor.

The light absorbed by the donor layer stimulates a substantial amount of charge generation triggered by the concurrent photoconductive and photovoltaic mechanisms, thus causing the increase of the $|S_{21}|$ parameter of the devices. Contrary to this beneficial effect, the $|S_{12}|$ parameter of the devices increases more sensibly than $|S_{21}|$ under illumination. Usually, the changes under light exposure of the Rollet's stability factor are negligible compared to the $|S_{12}|$ increase. The overall effect is a decrease of the maximum stable gain of the single transistor under illumination that causes a degradation of the S_{21} parameter of the entire amplifier. Obviously, the decrease of the amplifier S_{21} is also due to the mismatch at the device output caused by the variations of transistor $|S_{22}|$ parameter under light exposure, although this can be considered as a minor contribution. The light exposure effects occur by varying the wavelength of the laser beam, provided that the associated photon energy exceeds the bandgap energy of the heterojunction layers. In Figs. 2.64-2.65, the comparison between the noise figure and the scattering parameters without and with illumination at the wavelength of 532 nm is shown.

Once again, the light exposure causes a degradation of the noise figure and magnitude of S_{21}, whereas an improvement of the output matching parameter S_{22} occurs.

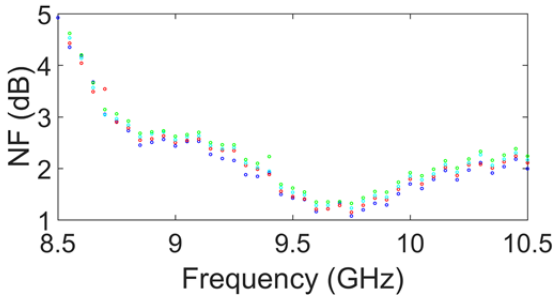

Fig. 2.64: Noise figure NF without (blue) and with illumination for optical power levels of 3 mW (red), 5.5 mW (cyan), 10 mW (green) at the bias point V_{DS} = 2 V and V_{GS} = - 0.21 V. The light wavelength is 532 nm.

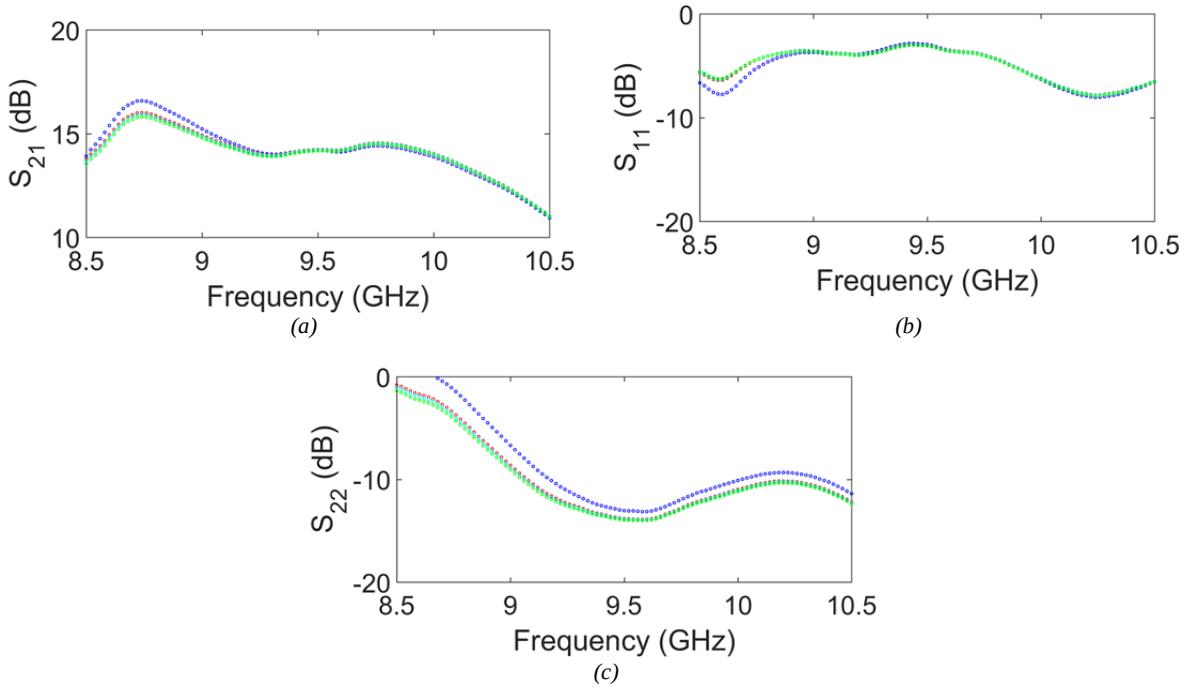

Fig. 2.65: S-parameters of the LNA (a) S_{21}, (b) S_{11}, (c) S_{22} without (blue) and with illumination for optical power levels of 3 mW (red), 5.5 mW (cyan), 10 mW (green)) at the bias point V_{DS} = 2 V and V_{GS} = - 0.21 V. The light wavelength is 532 nm.

The obtained data can be considered as an experimental proof of the predictive study reported in [24], as fully confirm the published results. Moreover, in the present work the analysis has been extended by varying the wavelength and the optical power levels of the laser beam.

In Figs. 2.66-2.67, the effects due to both optical wavelengths have been highlighted by reporting the S-parameters and the noise figure for the maximum optical incident power (10 mW) at V_{DS} = 2 V and V_{GS} = - 0.21 V.

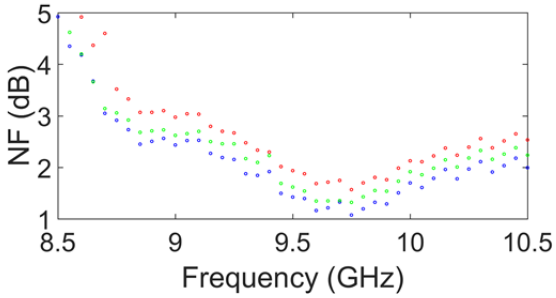

Fig. 2.66: Noise figure NF without (blue) and with illumination for the maximum optical power (10 mW) at the wavelengths of 635 nm (red), 532 nm (green). The bias point is V_{DS} = 2 V and V_{GS} = - 0.21 V.

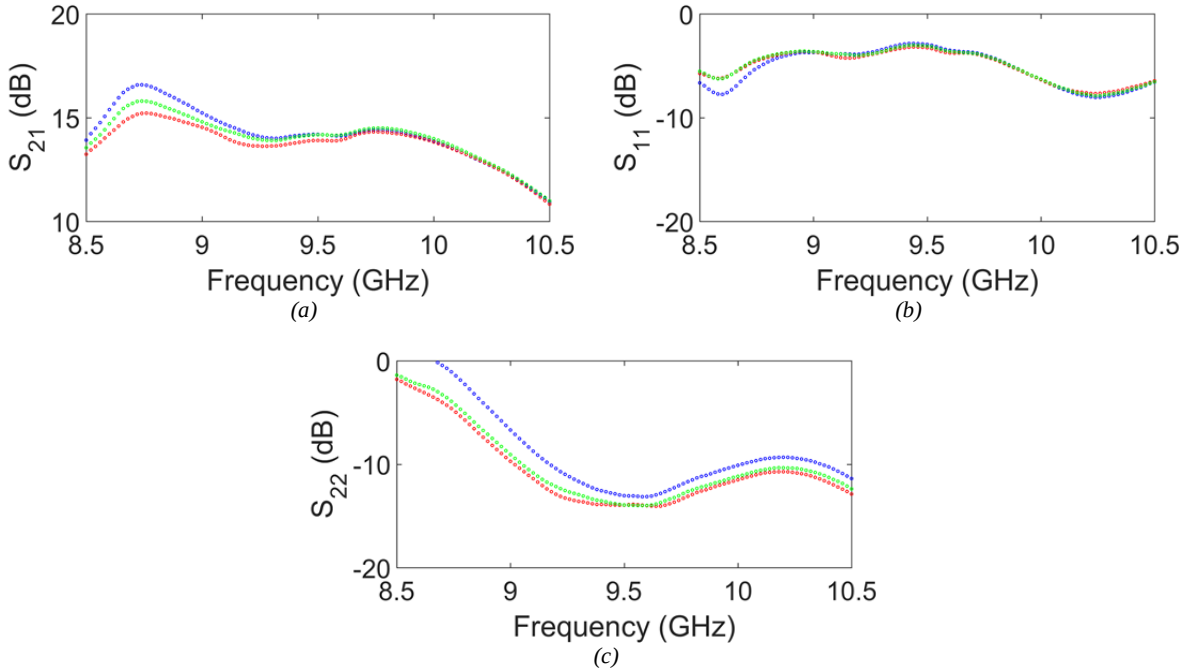

Fig. 2.67: S-parameters of the LNA (a) S_{21}, (b) S_{11}, (c) S_{22} without (blue) and with illumination for the maximum optical power (10 mW) at the wavelengths of 635 nm (red), 532 nm (green). The bias point is V_{DS} = 2 V and V_{GS} = - 0.21 V.

As it can be seen, the performance of the scattering parameters suggests that no advantages can be achieved by illuminating an amplifier biased at the recommended bias conditions.

It is worth noting that the effects seem more pronounced in the case of the 635 nm laser beam. Indeed, it must be observed that when the optical power level is kept at a constant value, the 635 nm laser beam contains a greater number of photons than the 532 nm one.

The higher the number of photons, the greater the effects on the amplifier behavior due to the higher number of electron-hole pairs generated by both the InGaAs channel and the AlGaAs donor layer provided that the optical absorption coefficient does not vary significantly.

By using the Planck's law reported in eq. 2.45 together with eq. 2.46, it is possible to evaluate the power level associated to the two laser beam wavelengths for obtaining the same number of photons ($n = 1.34 \cdot 10^{16}$) and therefore the same effects on the amplifier behavior:

$$E(\lambda) = h\nu \tag{2.45}$$

$$n = \frac{P}{E(\lambda)} \tag{2.46}$$

where E(λ) is the energy of the single photon at the optical wavelength λ, h is the Planck's constant, ν is the frequency of the emitted light and P is the optical power level incident on the amplifier.

To demonstrate the validity of the above argument, the LNA has been exposed first to the 635 nm laser light at the incident power of 4.2 mW, then to the 532 nm laser light at the incident power of 5 mW. The related NF and S- parameters are shown in Fig. 2.68.

As expected, the curves almost overlap thus confirming the hypothesis and assessing the accuracy of the measurement set-up.

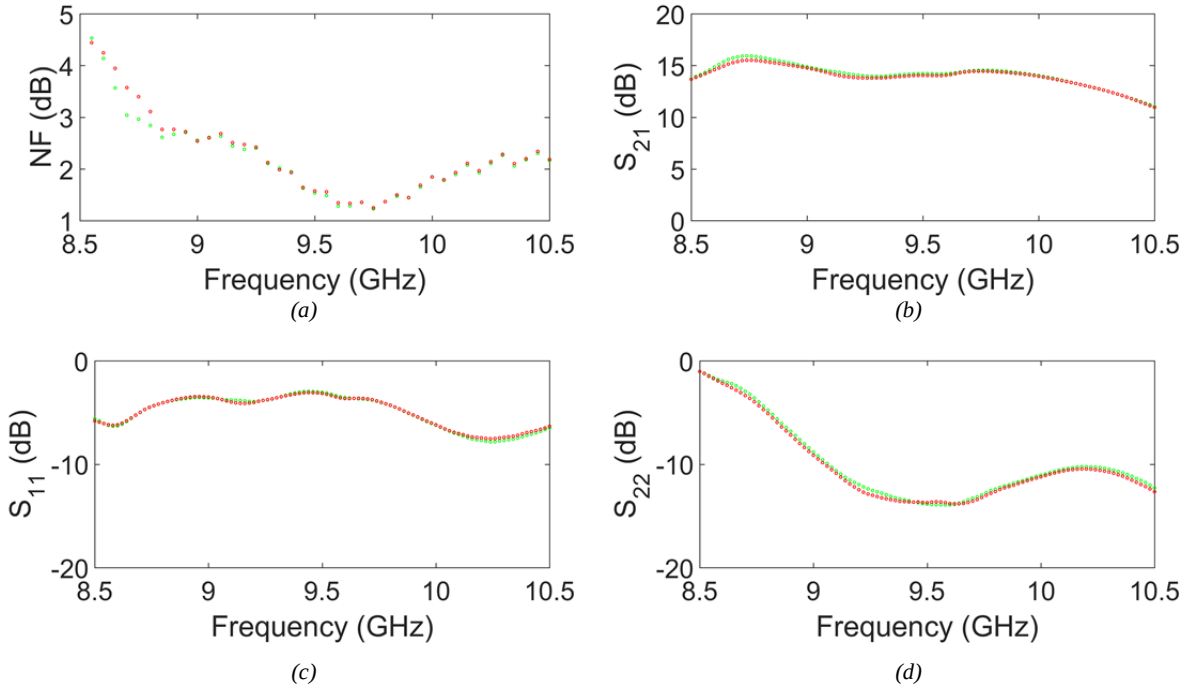

Fig. 2.68: LNA parameters: (a) NF, (b) S_{21}, (c) S_{11}, (d) S_{22} under illumination with 635 nm laser light delivering 4.2 mw (red) and 532 nm laser light delivering 5 mW (green) incident power. The bias point is V_{DS} = 2 V and V_{GS} = - 0.21 V.

With the aim of carrying out a proper comparison with [43], where evidence of the gain improvement under light exposure was claimed, the S- and NF parameters have been measured by biasing the LNA at the transistor pinch-off.

As a matter of fact, the marked improvement of the performance is due to the switching-on of the transistor but this is the only case where a performance enhancement can be noticed. This behavior is recognizable in Figs. 2.69-2.70, showing the effects observed for the S- and NF parameters under exposure to the maximum incident optical power (10 mW) at V_{DS} = 2 V and V_{GS} = - 0.56 V.

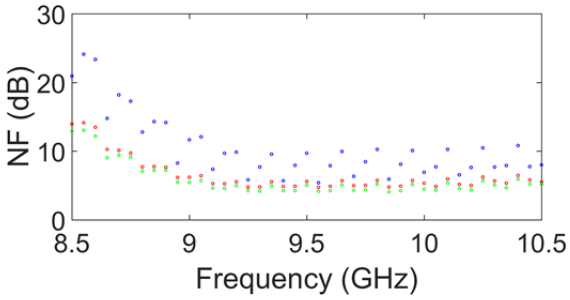

Fig. 2.69: NF without (blue) and with illumination at the wavelengths of 635 nm (red), 532 nm (green) under the maximum incident optical power (10 mW). The bias point is V_{DS} = 2 V and V_{GS} = - 0.56 V.

A clear improvement of the noise figure is evidenced, due to the light activation of the device since at the pinch-off bias the transistor is essentially a passive device and the LNA is truly far from the design conditions.

A similar comment can be made in terms of the scattering parameters. At the pinch-off, the small signal behavior of the pHEMT is very different from the one characterizing the active region performance. This allows a marked improvement of the performance when the amplifier is switched-on, because of the charge generation induced by the light exposure

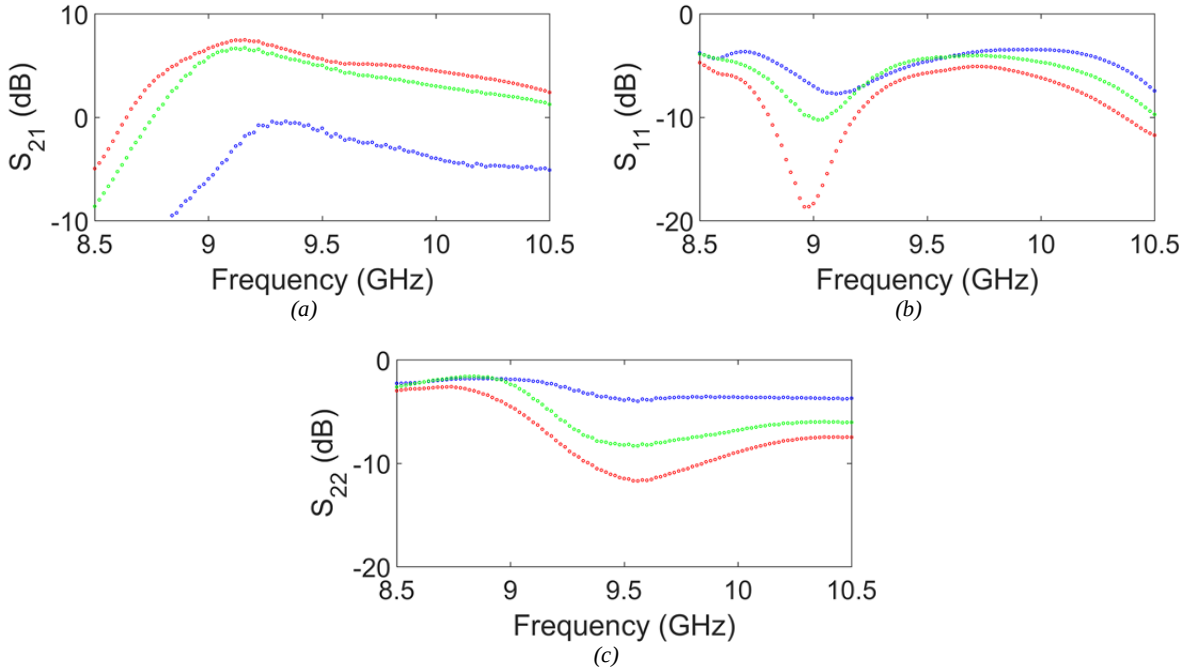

Fig. 2.70: S-parameters (a) S_{21}, (b) S_{11}, (c) S_{22} without (blue) and with illumination at the wavelengths of 635 nm (red), 532 nm (green) under the maximum incident optical power (10 mW). The bias point is V_{DS} = 2 V and V_{GS} = - 0.56 V.

As a consequence, we could claim that the improvement of the amplifier performance is due to the generated electron-hole pairs that move the operating point of the transistor from the pinch-off towards the active region. No additional benefits seem to be attributable directly to the effect of the light exposure

2.4 References

[1] D. M. Pozar, "Microwave engineering," Wiley, Inc., 2012.

[2] J. J. Carr, "RF components and circuits," Newnes, 2002.

[3] H. Friis, "Noise figures of radio receivers," *Proceedings of the IRE*, July 1944.

[4] G. D. Vendelin, A. M. Pavio, U. L. Rohde, "Microwave circuit design using linear and nonlinear techniques," Wiley, Inc., 2005.

[5] A. Caddemi, G. Martines, and M. Sannino, "HEMT for low noise microwaves: CAD oriented modeling," *IEEE Trans. Microw. Theory Techn.*, vol. 40, Jul. 1992

[6] G. Gonzales, "Microwave transistor amplifiers," Prentice Hall, 1984.

[7] M. W. Pospieszalski, "Modeling of noise parameters of MESFET's and MODFET's and their frequency and temperature dependence," *IEEE Trans Microw Theory Techn*, 1989.

[8] A. Caddemi, G. Martines, and M. Sannino, "HEMT for low noise microwaves: CAD oriented modeling," *IEEE Trans Microw Theory Techn*, 1992.

[9] G. Dambrine, H. Happy, F. Danneville et A. Cappy, "A new method for on wafer noise measurement," *IEEE Trans Microw Theory Techn*, 1993.

[10] A. Lazaro, L. Pradell, and J.M. O'Callaghan, "FET noise-parameter determination using a novel technique based on a 50-Ω noise-figure measurements," *IEEE Trans Microw Theory Techn*, 1999.

[11] A. Caddemi and G. Crupi, "On the noise measurements and modeling for on wafer HEMTs up to 26.5 GHz," *Microw Opt Tech Lett*, 2010.

[12] F. Danneville, "Microwave noise and FET devices," *IEEE Microw Mag 11*, 2010.

[13] A. Caddemi, G. Crupi, E. Fazio, S. Patanè, and G. Salvo, "Remarks of an extensive investigation on the microwave HEMT behavior under illumination," *IEEE Microw Wirel Compon Lett, Feb.* 2014.

[14] A. Caddemi, G. Crupi, and G. Salvo, "A link between noise parameters and light exposure in GaAs pHEMT's," *Solid-State Electron*, Mar. 2015.

[15] G. Crupi, D. M. M.-P. Schreurs, A. Raffo, A. Caddemi, and G. Vannini, "A new millimeter wave small-signal modeling approach for pHEMTs accounting for the output conductance time delay," *IEEE Trans Microw Theory Techn*, 2008.

[16] A. Zarate-de Landa, J.E. Zuniga-Juarez, J.R. Loo-Yau, J.A. Reynoso-Hernandez, M.C. Maya-Sanchez, and J.L. del Valle-Padilla, "Advances in linear modeling of microwave transistors," *IEEE Microw*, May. 2009.

[17] A. Caddemi, G. Crupi, and A. Macchiarella, "On wafer scaled GaAs HEMTs: direct and robust small signal modelling up to 50 GHz," *Microw Opt Tech Lett*, 2009.

[18] G. Dambrine, A. Cappy, F. Heliodore, and E. Playez, "A new method for determining the FET small-signal equivalent circuit," *IEEE Trans Microw Theory Techn*, 1988.

[19] A. Caddemi, E. Cardillo, G. Crupi, "Microwave Noise Parameter Modeling of a GaAs HEMT under Optical Illumination," *Microw Opt Tech Lett*, Jan. 2016

[20] R. Vandersmissen, D. M. M.-P. Schreurs, S. Vandenberghe, and G. Borghs, "A time- and frequency-domain characterization of a thin-film metamorphic HEMT under modulated backside illumination," *Int J RF Microw Comput-Aided Eng*, 2004.

[21] G. Crupi and D. M. M.-P. Schreurs, "Microwave de-embedding: from theory to applications," Oxford, UK: Academic Press, 2013.

[22] M. Berroth and R. Bosch, "High frequency equivalent circuit of GaAs FET's for large-signal applications," *IEEE Trans Microw Theory Techn*, 1991

[23] H. Fukui, "Optimal noise figure of microwave GaAs MESFET's," *IEEE Trans. Electron Devices*, Jul. 79.

[24] A. Caddemi, E. Cardillo, and G. Crupi, "Comparative analysis of microwave low-noise amplifiers under laser illumination," *Microw. Opt. Tech. Lett.*, Oct. 2016.

[25] A. Caddemi, G. Crupi, E. Fazio, S. Patanè, and G. Salvo, "Analysis of microwave noise parameters of scaled AlGaAs/GaAs HEMT's under light exposure," *Proceedings of the 11th IEEE International Conference on Telecommunications in Modern Satellite, Cable and Broadcasting Service (TELSIKS)*, Nis (Serbia), Oct. 2013.

[26] R. A. Pucel, H. A. Haus, and H. Statz, "Signal and noise properties of gallium arsenide microwave field-effect transistors," *Adv. Electronics Electron Phys*., 1975.

[27] A. Caddemi, E. Cardillo, and G. Crupi, "Light activation of noise at microwave frequencies: a study on scaled gallium arsenide HEMT's," *IET Circuits, Devices and Systems*, Nov. 2017.

[28] R. Pucel, W. Struble, and R. Hallgreen, "A general noise deembedding procedure for packaged two-port linear active devices," *IEEE Trans. Microwave Theory Techn.*, Nov. 1992.

[29] R.P. Meys, "A wave approach to the noise properties of linear microwave devices," *IEEE Trans Microw Theory Tech*, 1978.

[30] S.W. Wedge and D.B. Rutledge, "Wave techniques for noise modeling and measurement," *IEEE Trans Microw Theory Tech*, 1992.

[31] D. Pasquet, E. Bourdel, S. Quintanel, T. Ravalet, and P. Houssin, "New method for noise-parameter measurement of a mismatched linear two-port using noise power wave formalism," *IEEE Trans Microw Theory Tech*, 2008.

[32] V. Đorđević, E. Cardillo, Z. Marinković, O. Pronić-Rančić, A. Caddemi, and V. Marković, “Wave approach to the noise modeling of the GaAs HEMT under optical illumination,” submitted for publication in *Electrical Engineering*, Feb. 2018.

[33] Q.J. Zhang and K.C. Gupta, “Neural networks for RF and microwave design,” Boston, Artech House, 2000.

[34] P. Choi, S. Goswami, U. Radhakrishna, D. Khanna, C.-C. Boon, H.-S. Lee, D. Antoniadis, "A 5.9-GHz fully integrated GaN frontend design with physics-based RF compact model," *IEEE Trans. Microw. Theory Techn.,* Apr. 2015.

[35] Z. Q. Cheng, Y. Cai, J. Liu, Y. Zhou, K. M. Lau, K. J. Chen, "A low phase-noise X-band MMIC VCO using high-linearity and low-noise composite-channel Al0.3Ga0.7N/Al0.05Ga0.95N/ GaN HEMTs," *IEEE Trans. Microw. Theory Techn.,* Jan. 2007.

[36] S. K. Mazumder, "An overview of photonic power devices," *IEEE Trans. Power Electronics*, Sept. 2016.

[37] J. H. Leach, R. Metzger, E. A. Preble, K. R. Evans, "High voltage bulk GaN-based photo-conductive switches for pulsed power applications," *Proc. SPIE 8625, Gallium Nitride Materials and Devices VIII*, March 2013.

[38] A. Caddemi, E. Cardillo, G. Salvo, and S. Patanè, “Microwave effects of UV light exposure of a GaN HEMT: Measurements and model extraction,” *Microelectronics Reliability*, Oct. 2016.

[39] M. A. Romero, L. E. M. de Barros Jr, P.R. Herczfeld, "Internal photovoltaic effect in microwave devices," *1994 IEEE MTT-Symposium Digest*, Jun. 1994.

[40] C.-S. Choi, H.-S. Kang, Woo-Young Choi, H.-J. Kim, W.-J. Choi, D.-H. Kim, K.-C. Yang, K.-S. Seo, "High optical responsivity of InAlAs–InGaAs metamorphic High-Electron Mobility Transistor on GaAs substrate with composite channels," *IEEE Photonics Technology Letters*, Jun. 2003.

[41] M. H. Somerville, A. Ernst, J. A. del Alamo, "A physical model for the Kink effect in InAlAs/InGaAs HEMT’s," *IEEE Trans. Electron. Dev.,* May 2000.

[42] A. Caddemi, and E. Cardillo, "Optical control of gain amplifiers at microwave frequencies," *Computing and Electromagnetics International Workshop (CEM)*, Barcelona, Spain, Jun. 2017.

[43] J.M. Zamanillo, J. Portilla, C. Navarro, C. Pérez-Vega, "Optical ports: Next generation of MMIC control devices?," *35th European Microwave Conference*, Oct. 2005

[44] A.A. de Salles, and M. A. Romero, "Al0.3Ga0.7/GaAs HEMT's under optical illumination," *IEEE Trans. Microwave Theory Tech.*, Dec. 1991.

[45] Caddemi, E. Cardillo, S. Patanè, and C. Triolo, "Low-noise amplifier under optical illumination: a complete experimental investigation of microwave and noise performance," submitted for publication in *IEEE Sensors Journal*, Jan. 2018.

3 Microwave filters

This chapter describes why filters are components of basic importance in a microwave radar. During the development of this thesis work, a planar microwave filter with a very wide bandwidth has been designed, realized and tested. The results are also presented and discussed in the current chapter.

3.1 Filters in radar receiver

Filters are essential components not only in a radar systems but virtually in any type of microwave communication or test and measurement system.

This aspect can be clear by considering the sensitivity of a receiver, i.e. the lowest signal power level S_{min} that can be correctly detected for obtaining the desired signal with a certain signal-to-noise, SNR. It can be expressed as reported in eq. (3.1):

$$S_{min} = SNR\ k\ T_0 B\ F \tag{3.1}$$

where:

k is the Boltzmann's constant in watt-per-seconds/Kelvin;

T_0 is the temperature of the receiver input in Kelvin;

B is the receiver bandwidth in Hertz;

F is the noise factor.

The kT_0B term is the total thermal noise power. Since it depends from the overall bandwidth of the receiver, the importance of using a filter becomes clear because filtering reduces the noise in the receiver.

Moreover, another major problem which requires filtering is the presence of large interference signals which can cause receiver desensitization.

A microwave filter is a two-port network used to control the frequency response at any given section of a microwave system by providing transmission at frequencies within the passband of the filter and attenuation in the stopband of the filter [1].

Typical frequency responses include low-pass, high-pass, band-pass and band-reject (band-stop) characteristics.

An ideal filter would have zero insertion loss in the passband, infinite attenuation in the stopband and a linear phase response (to avoid signal distortion) in the passband. Actually, a compromise must be reached; herein lies the art of filter design. The necessary trade-offs can be evaluated to best meet the application requirements.

The transfer function of a filter, i.e. the mathematical description of the response characteristics, corresponds to the S_{21} parameter of the filter when working with radiofrequency or microwave systems. In most cases, for a lossless filter it can be written as an amplitude-squared transfer function defined as reported in eq. (3.2):

$$|S_{21}(j\Omega)|^2 = \frac{1}{1 + \varepsilon^2 F_n^2(\Omega)} \tag{3.2}$$

where:

ε is the ripple constant;

$F_n(\Omega)$ is the filtering or characteristics function;

Ω is the angular frequency.

From eq. (3.2), the insertion loss of the filter can be expressed as in eq. (3.3) [2]:

$$L_A(\Omega) = 10 \log \frac{1}{|S_{21}(j\Omega)|^2} \, dB \tag{3.3}$$

Whereas the return loss of the filter can be computed by using eq. (3.4):

$$L_r(\Omega) = 10 \log(1 - |S_{21}(j\Omega)|^2) \, dB \tag{3.4}$$

Consequently, if the rational transfer function is available, the phase and group delay response can be calculated by using respectively eq. (3.5) and eq. (3.6):

$$\phi_{21} = Arg S_{21}(j\Omega) \tag{3.5}$$

$$\tau_d(\Omega) = \frac{d\phi_{21}(\Omega)}{-d\Omega} \tag{3.6}$$

Different transfer functions can be considered, based on their response.

The Butterworth (maximally flat) response has a L_{Ar} = 3 dB insertion losses at the normalized cut-off frequency Ω_C = 1 (rad/s). Here n is the order of the filter, corresponding to the number of reactive elements of the network. The Butterworth response exhibits a maximally flat behavior within the pass band as depicted in Fig 3.1.

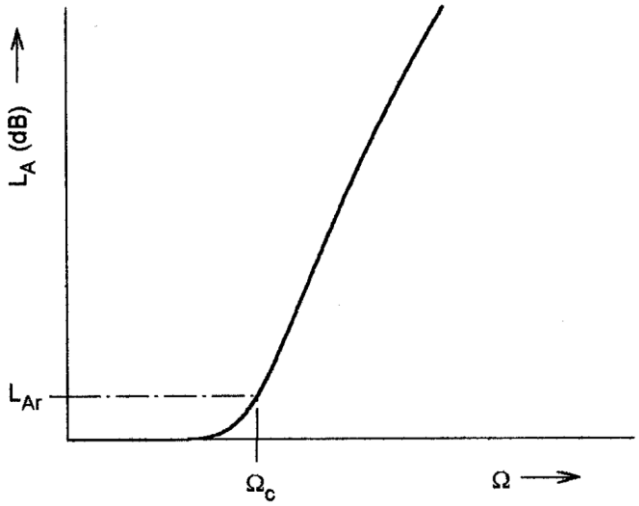

Fig. 3.1. Butterworth low-pass response [2].

When a sharper rejection is needed, the filter response may be chosen to be of the Chebyshev type characterized by a maximally flat rejection band and an equal ripple in-band performance. The filter response is described by eq. (3.7):

$$|S_{21}(j\Omega)|^2 = \frac{1}{1 + \varepsilon^2 T_n^2(\Omega)} \tag{3.4}$$

where the ripple factor is given by eq. (3.8):

$$\varepsilon = \sqrt{10^{\frac{L_{Ar}(\Omega)}{10}} - 1} \tag{3.4}$$

The Chebyshev response has been reported in Fig 3.2.

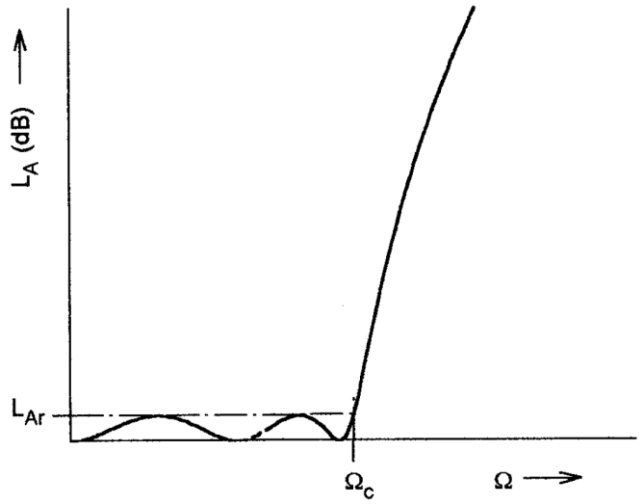

Fig. 3.2. Chebyshev low-pass response [2].

When better performances of rejection are required, the Cauer or Elliptic response is chosen with equal ripple characteristics either in band and out-of-band. The filter response can be computed by using eq. (3.8):

$$|S_{21}(j\Omega)|^2 = \frac{1}{1+\varepsilon^2 F_n^2(\Omega)} \tag{3.8}$$

The Cauer response has been depicted in Fig 3.3.

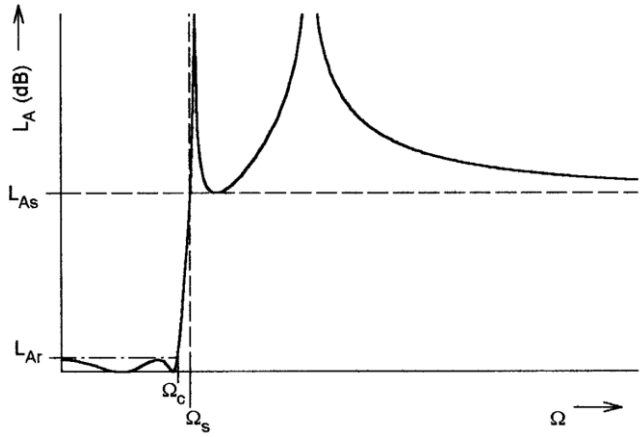

Fig. 3.3. Chebyshev low-pass response [2].

In some applications (such as multiplexing filters for communication system) it is important to have a linear phase response in the band to avoid signal distortion. It turns out that a sharp-cutoff response is generally incompatible with a good phase response, so the phase response of the filter must be deliberately synthetized, usually resulting in an inferior amplitude cutoff characteristic. Linear phase filters allow to achieve a maximally flat performance of the group delay.

3.2 Extra wideband filters for microwave applications

Hereafter a methodology for the design of an extra wideband microwave filter with a notch at a desired frequency has been reported [3].

Recently, a growing attention is being paid to very large bandwidth filters extending from S-band even to low Ku-band for various demanding applications such as telecommunication front-ends working in the unlicensed FCC ultra wide-band (UWB) band or radioastronomy receivers for geodetic VLBI observations [4-7].

Starting from a scientific collaboration with the IRA-INAF Radioastronomy Observatory of Noto, Italy, the need for extra wideband microwave filters has emerged and a first design has been presented [8].

Together with the need of premium performance, like very low insertion loss, high out-of band rejection and flat group delay, additional features such as the flexibility of the structure are required to fit the component to for various applications in a cost-effective way.

Besides, strong unwanted interferences are not unusual, especially with the increasing bandwidth, so that ad-hoc selective blocking sub-bands (notches) are needed for a given application.

In the scientific literature, structures depicted as extra wideband filters with multiple notches are found to be very straightforward to design. On the other hand, components having a relative bandwidth greater that 100% with only a single notch, instead of multiple blocking sub-bands, are less common to find. Indeed, the insertion of a single notch is a critical issue due to the appearance of multiple sub-bands as it is typical of distributed structures having such a wide band [9-14].

The feasibility of re-designing the notch frequency is also a frequently required characteristic, so it would be highly desirable to quickly and easily re-design maintaining the filter main structure.

This paragraph presents a CAD methodology for the design of a microstrip extra wideband filter, with a 120% fractional bandwidth (FBW) in the 5-20 GHz frequency band, equipped with a notch at a desired frequency. The main band-pass filter employing a high dielectric constant substrate, features in-band and out-of-band insertion loss of 0.4 dB and -20 dB, respectively, in-band return loss of -10 dB and very flat group delay. The overall length of the band-pass filter is less than 26 mm; the width is less than 10 mm for the notched filter, thus leading to a very compact structure. The lengths of the input and output transmission lines have been increased to allow a simpler assembly of the connectors. However, the overall dimensions can be further reduced to reach a minimum estimated length of 16.0 mm, without considering any stretching of the two access lines.

An electromagnetic (EM) analysis of the filter layout encompassing the port connectors has been included for a more complete prediction of the filter performance.

Finally, a simple relationship between the notch frequency and a single geometrical parameter has been derived. By interpolating the data, a straight-line equation has been extracted, thus allowing a fast and simple design of the notch frequency. The key strength of this filter lies in the capability of obtaining the largest bandwidth performance found in the scientific literature with a single notch inside, together with the possibility of shifting the notch frequency in a very simple way, while maintaining a cost-effective and compact structure. The effectiveness of the method and its good performance are hereafter outlined.

As a preliminary step, several structures for the filter design have been studied in order to obtain the best solution for achieving the desired bandwidth. In many cases, the main problems have been the achievement of feasible line impedance values over such a wide bandwidth, to avoid an excessively small microstrip width or gap space, together with easy tailoring features. As a final choice, the Stub Synthesis technique has been adopted as a starting point for the filter design, to meet the constraint of such a wide bandwidth [11]. Afterwards, the methodology has been adjusted to improve the performances and to insert a single notch by adjusting a single element. The microstrip technology has been selected to allow a light, compact and cost-effective realization of the device by employing our in-house prototyping system for hybrid microwave circuit realization. In order to satisfy the requisite of space saving, a high dielectric constant material has been chosen. The adopted substrate is TMM10i, ROGERS Corporation® ceramic, hydrocarbon, thermoset polymer composite ($\varepsilon r = 9.8 \pm 0.245$, $tg\delta = 0.0020$, $t = 508$ μm) with 17 μm - thick copper metallization.The ultra-wide-bandwidth of the filter extends from 5.0 to 20 GHz (FBW of 120%). The main design constraints have been as follows: in-band insertion loss less than 0.5 dB, out-of-band insertion loss higher than -10 dB and a maximally flat group delay. At the beginning, the insertion of a simple variable notch has shown to increase the complexity in the selection of the appropriate design methodology, but later on it has revealed to be a key point of the project flexibility as discussed in the next section. The basic concept of the design methodology was to create a main path from the input to the output of the component without modifying the signal at the centre frequency [5], [15]. Consequently, the length of the path was chosen to be one wavelength at the centre frequency of 12.5 GHz. A parallel type of resonance (antiresonance) can be achieved using a short-circuited transmission line of length $\lambda/4$ so that the length of the path to the ground was chosen to be exactly one-

quarter wavelength at the same frequency, [15]. The impedance values of the transmission lines were fixed to be 50 Ω. The design was carried out employing Microwave Office® by NI AWR Design Environment™. The basic structure and its performance in terms of the S_{11} and S_{21} parameters are reported in Fig. 3.4 a-b.

As a first outcome, the obtained scattering parameters have not led to satisfactory results. The transition at the band edges needed to be more abrupt and the whole band-pass required to be widened. Therefore, the basic filter section was repeated to fulfil the specifications.

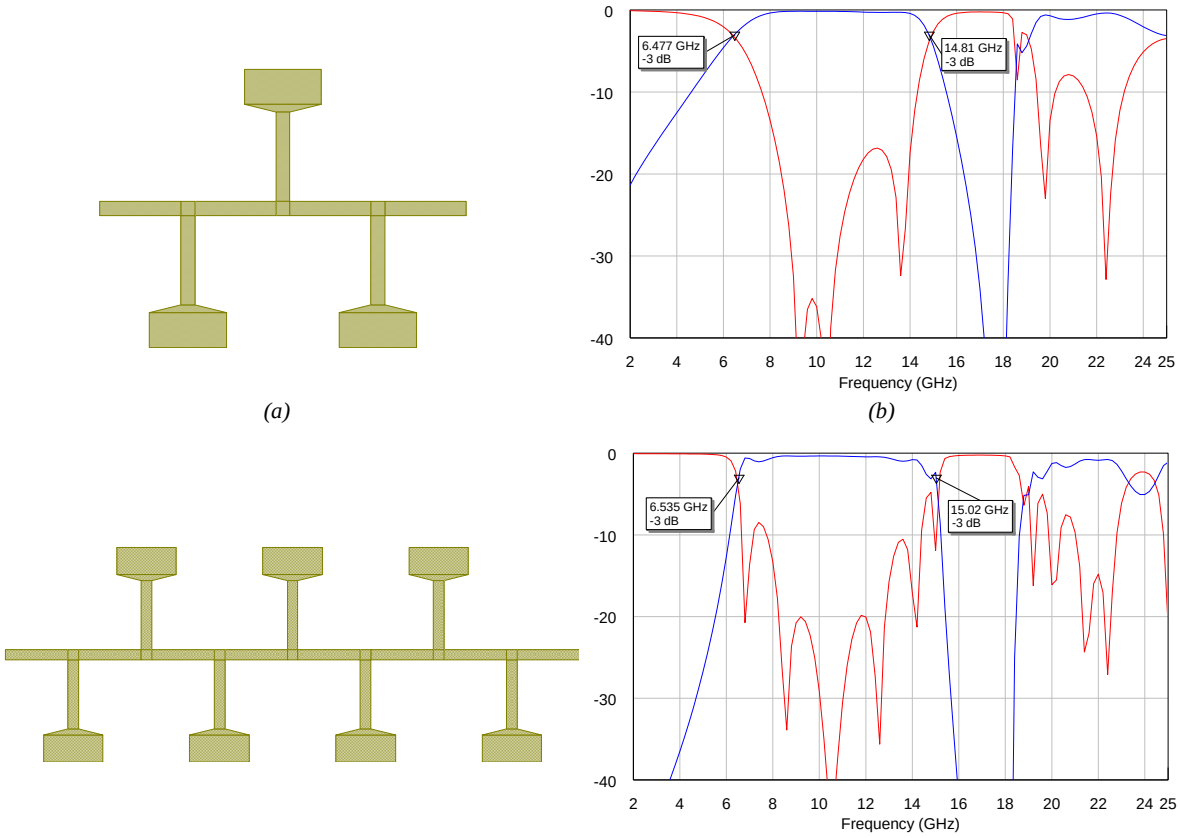

Fig. 3.4. (a) Layout of the basic filter cell; (b) scattering parameters S_{21} (blue) and S_{11} (red) of the first filter, (c) layout of the extended structure, (d) S_{21} (blue) and S_{11} (red) of the modified structure [3].

Accordingly, some adjustments have been made to improve the filter performance [16]. The extended structure and its related performance are reported in Fig. 3.4 c-d. After some attempts, it has been observed that a reduction of the width of the short-circuited stubs could have improved the performance of the component in terms of bandwidth. Therefore, this parameter was set to a minimum value, complying with reasonable fabrication constraints, to stretch out the bandwidth. Then, the lengths of either the main section and the short-circuited stub sections

have been tuned in order to shift the bandwidth towards the desired frequency range. Finally, the dimensions of the main transmission line section, from input to output, have been slightly modified by using the Microwave Office® Optimizer tool in order to reach the best performance. In order to obtain a more reliable prediction of the component behavior, an electromagnetic (EM) analysis of the layout was then performed and a tuning of the line dimensions was made. In addition, to reduce the discontinuity between the microstrip top conductor and the connector transition pin, a taper has been introduced at the edge terminals.

In Fig. 3.5, the final 3D layout, the group delay and the scattering parameters obtained by the EM simulation of the filter are shown.

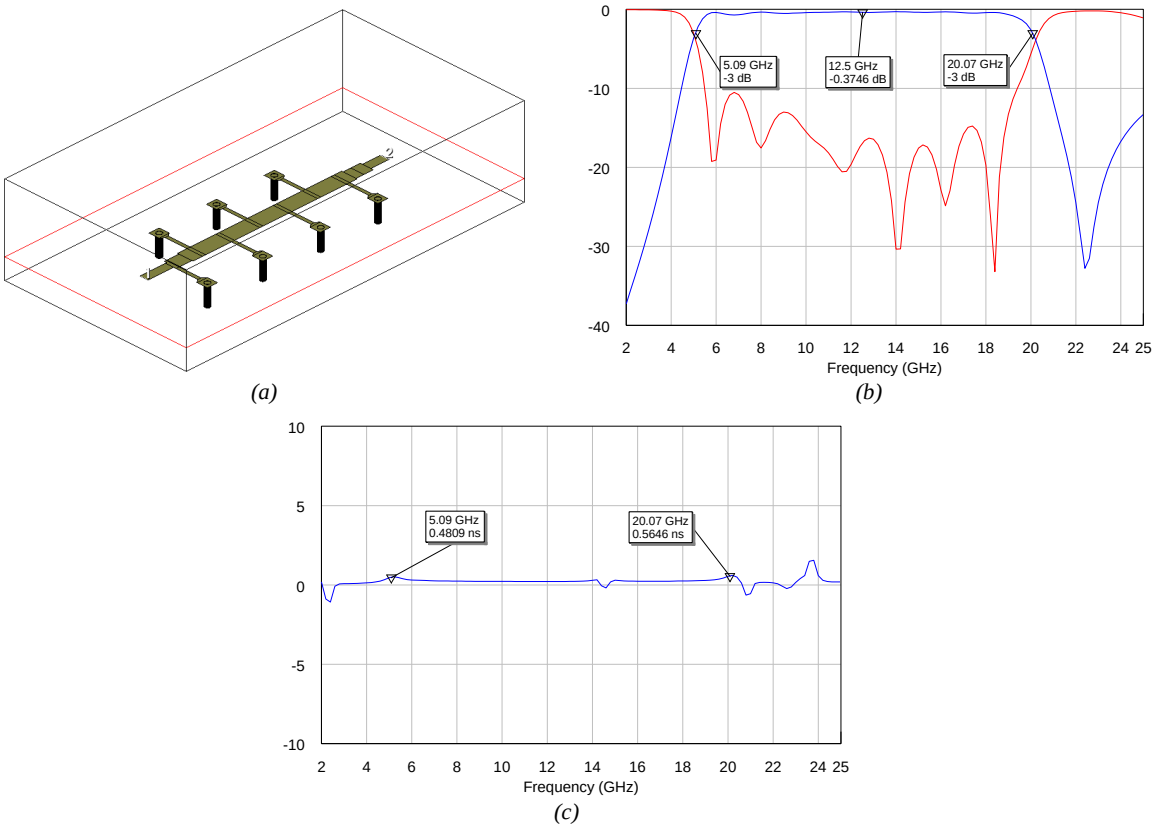

Fig. 3.5: (a) 3D layout of the filter: scattering parameters obtained by EM simulations of the structure: (b) S_{21} (blue) and S_{11} (red), (c) group delay [3].

The insertion of the notch has to fulfil two main specifications:

- The notch frequency shift must be accomplished without modifying the edges of the filter bandwidth;
- A relationship between the frequency and the line dimensions should be extracted; it has to be simple and to allow a fast re-design of the structure.

To accomplish these requirements, a properly designed open-circuit stub was then introduced (red circle in Fig. 3.6). It was observed that the optimum position changed according to either the filter bandwidth and the dielectric material.

Some simulations were made by varying the open-stub position, in order to keep the notch bandwidth as narrow as possible.

In Fig. 3.6, the final filter 3D layout is shown, whereas all element dimensions are listed in Tab. III.I. The first two stubs have been bent due to the proximity of the input connector.

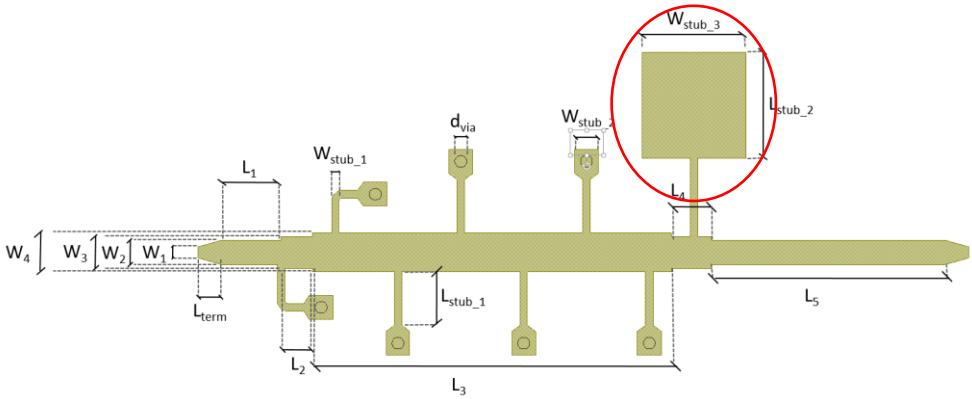

Fig. 3.6. 3D layout of the final filter with notch [3].

TABLE III.I Dimensions of the filter elements. The lengths of the four employed open stubs have been reported [3].

Element	***Value***
W_1 (μm)	381
W_2 (μm)	800
W_3 (μm)	1080
W_4 (μm)	1280
W_{stub_1} (μm)	250
W_{stub_2} (μm)	800
W_{stub_3} (μm)	3500
L_1 (μm)	1985
L_2 (μm)	1055
L_3 (μm)	12050
L_4 (μm)	1358
L_5 (μm)	7835
L_{stub_1} (μm)	1800
L_{stub_2} (μm)	2550/3050/3550/4050
L_{term} (μm)	800
d_{via} (μm)	400

As it can be observed, the notch centre frequency can be easily shifted by varying a single stub length, which is an interesting feature in order to obtain a simple relationship between the notch frequency and the line dimension.

By interpolation of the data, a well-behaved dependence of the notch frequency on the stub length can be observed as reported in Fig. 3.7 (continuous line). Furthermore, in order to obtain a flexible tool for the notch tailoring, the equation coefficients for a linear interpolation (dashed line) were extracted as follows:

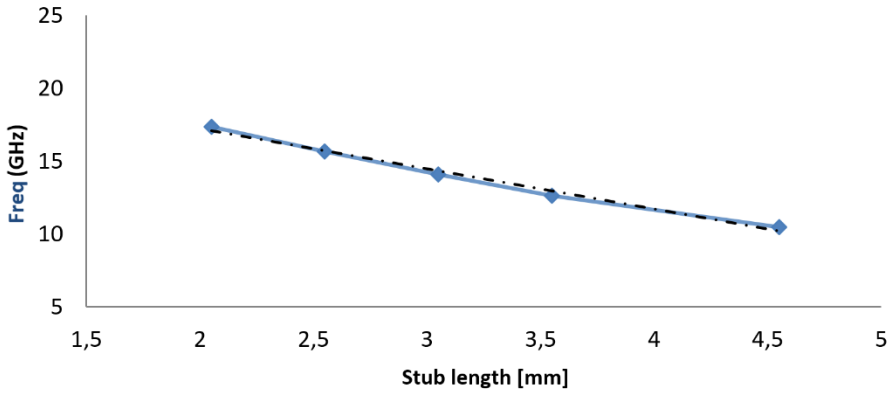

Fig. 3.7. Open-stub length vs notch frequency: comparison between simulated (blue line) and interpolated (black dashed) data [3].

The different notches, characterized by a fixed narrow band, are shown in Fig. 3.8. In the reported graphs, it is clearly recognizable that the overall band-pass cut-off frequencies of the filter are not influenced, as requested. In Fig. 3.8 c-d, a little reduction in the upper cut-off frequency seems to happen but this is simply due to the first notch repetition occurrence.

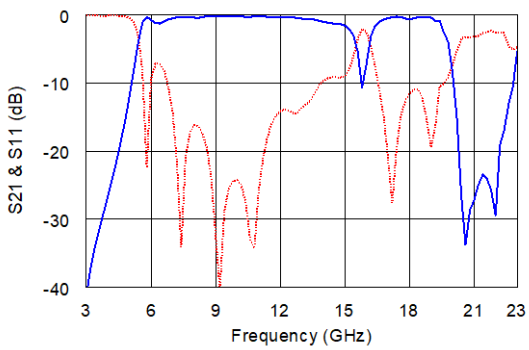

(a)

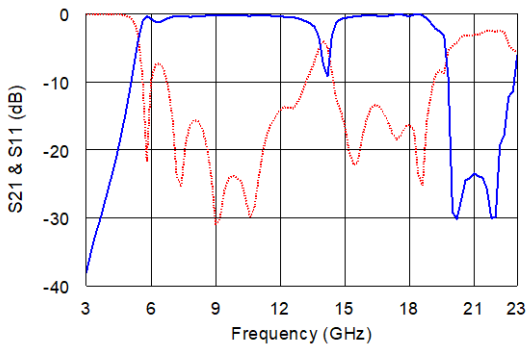

(b)

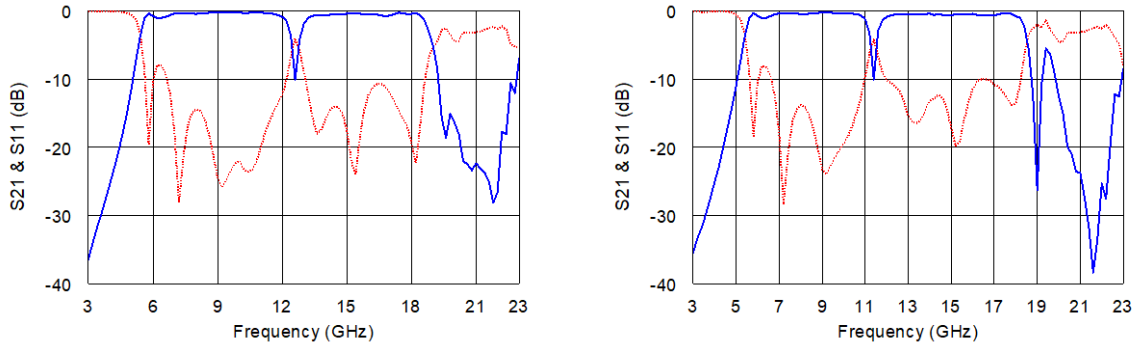

(c) *(d)*

Fig. 3.8. Scattering parameters of the structures characterized by different notches. S_{21} (blue line) and S_{11} (red dashed line) for a stub length of: (a) 2.55 mm, (b) 3.05 mm, (c) 3.55 mm, (d) 4.05 mm [3].

Following the simulation results, the reliability of the design procedure has been enhanced by performing the EM simulation of the port coaxial connectors.

The employed connectors are Southwest Microwave, Inc.® 2.92 mm JACK End Launch Connectors, that allow a fast connection of the filter ports without any bonding.

Since the heaviest discontinuity occurs in the transition between the microstrip and the central pin of the connector, the 3D model used in the simulator did not include the bulk connector structure of the transition blocks. By the preliminary simulations, a very good correlation with the expected behavior has been achieved. In Fig. 3.9, the 3D filter layout including the port coaxial connectors and the relevant scattering parameters are reported.

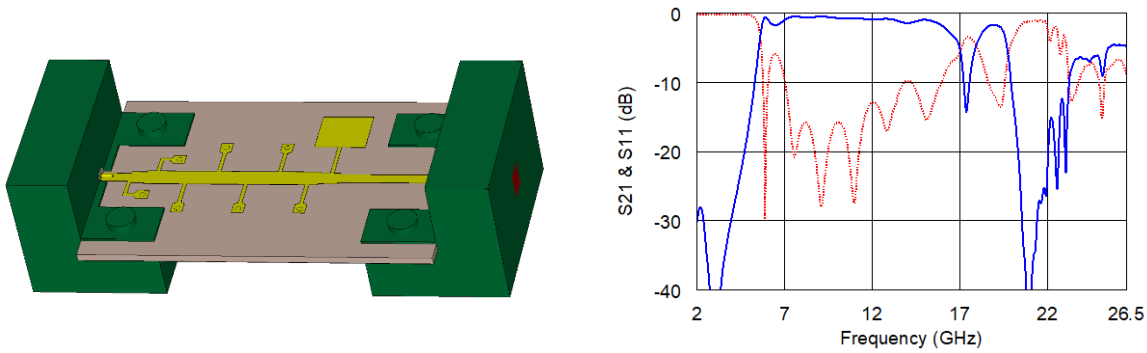

(a) *(b)*

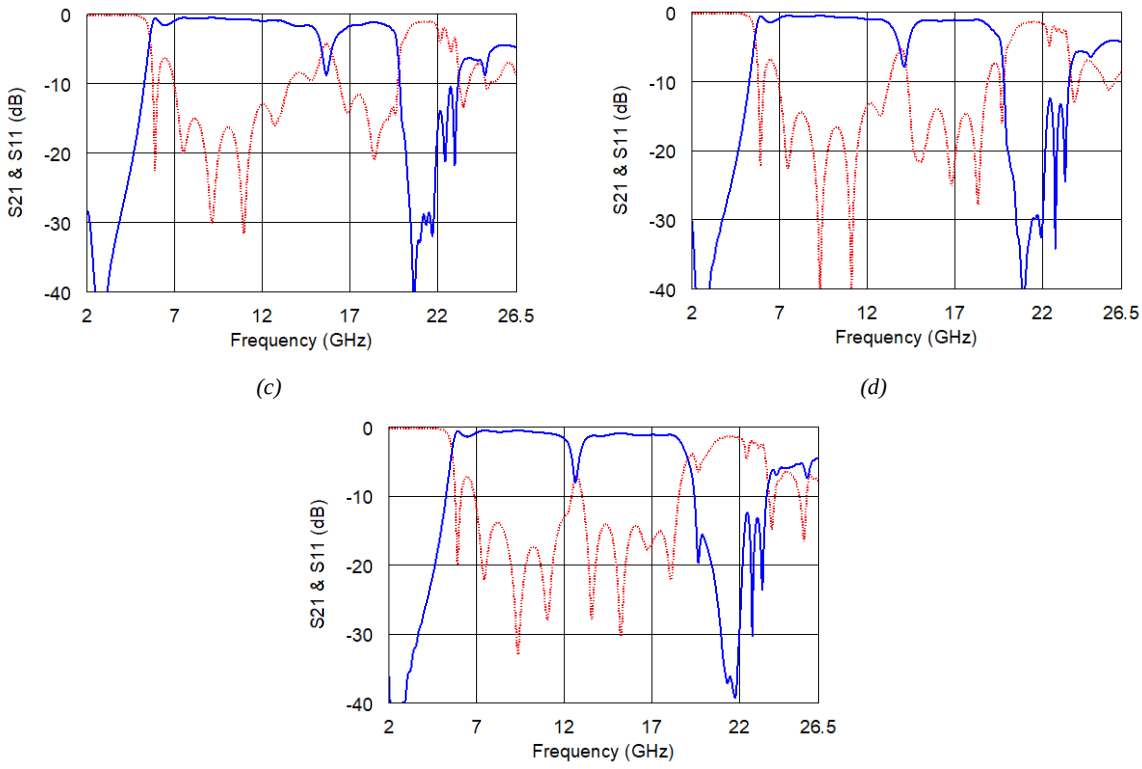

Fig. 3.9. (a) 3D filter layout including the port coaxial connectors; (b) S_{21} (blue line) and S_{11} (red dashed line) for a stub length of (a) 2.55 mm, (b) 3.05 mm, (c) 3.55 mm, (d) 4.05 mm [3].

As a second step, sample filters have been implemented to confirm the predicted performance. The components have been prototyped by using a high precision mechanical plotter S103 Protomat LPKF. The photos of three notched band-pass filters having different stub lengths are shown in Fig. 3.10.

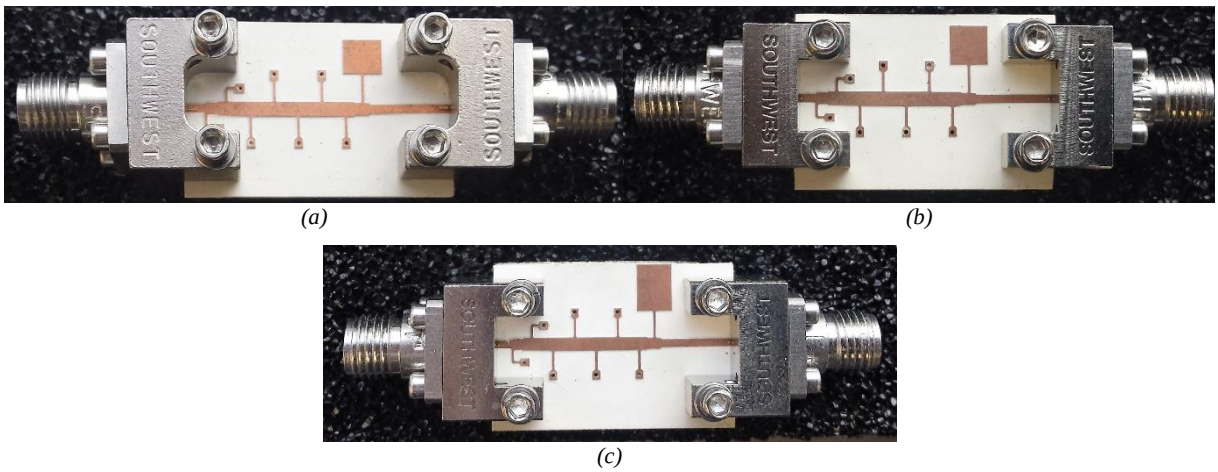

Fig. 3.10: Notched band-pass filters having different stub lengths: (a) 3.05 mm; (b) 3.55 mm; (c) 4.55 mm [3].

The scattering parameters of the filters prototypes have been measured by an Agilent PNA E8364A from 2 to 26.5 GHz. The comparisons between measured and EM simulated data for the S21, S11 and group delay parameters are shown in Figs. 3.11-3.12 for the samples in Fig. 3.10 b-c.

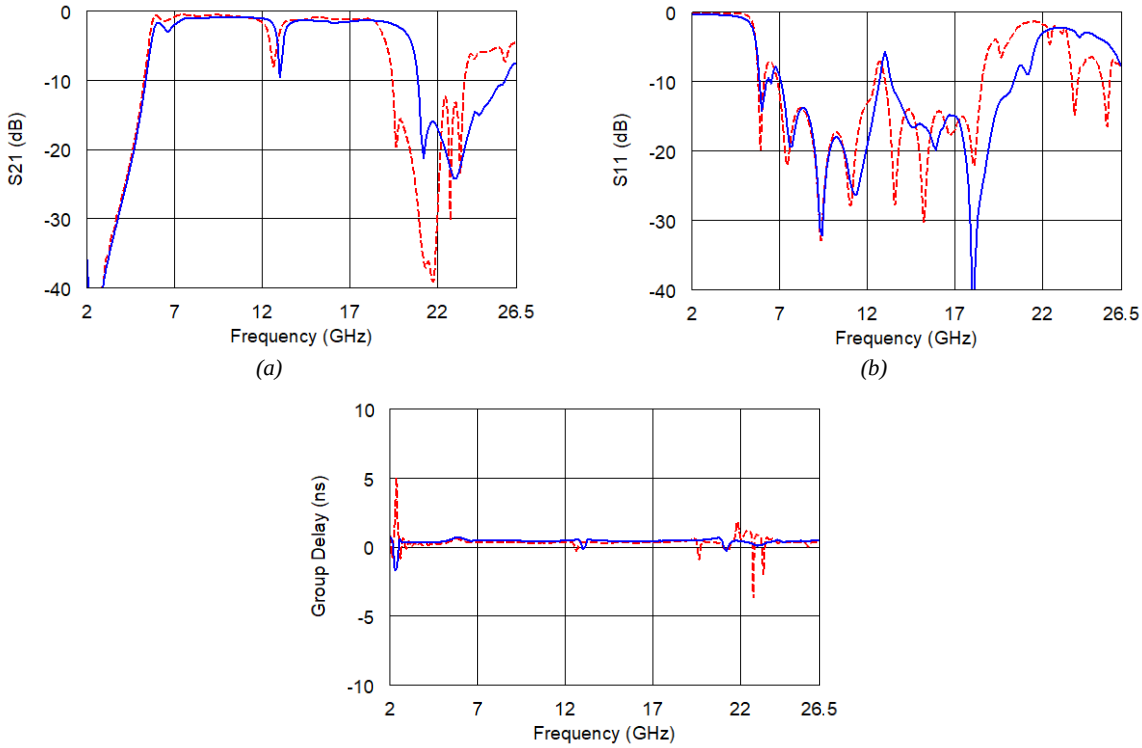

Fig. 3.11: Comparison between measured (blue line) and simulated (red dashed line) (a) S_{21}, (b) S_{11} and (c) group delay for a stub length of 3.55 mm [3].

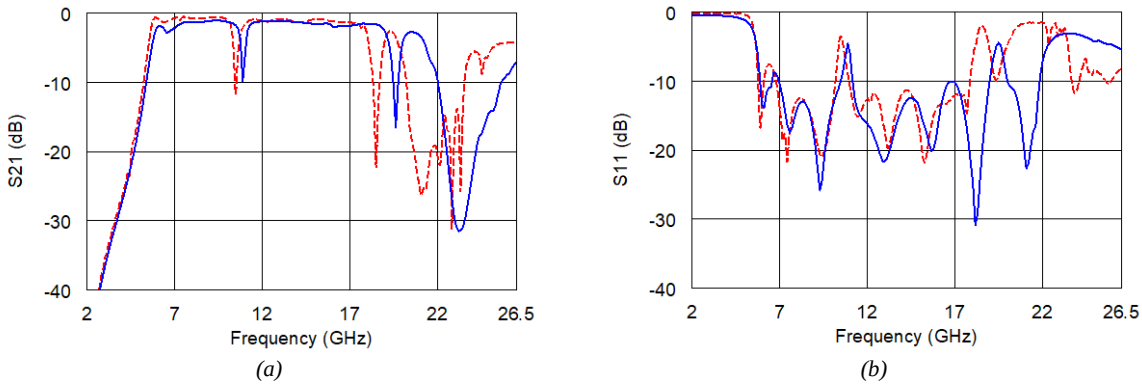

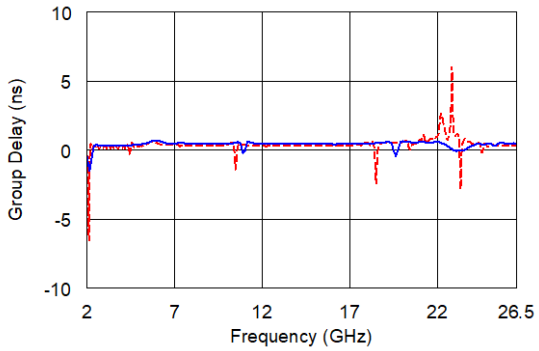

(c)

Fig. 3.12: Comparison between measured (blue line) and simulated (red dashed line) (a) S_{21}, (b) S_{11} and (c) group delay for a stub length of 4.55 mm [3].

The straight correspondence between the notch frequency and the open-stub length has been confirmed by the experimental data.

The measured performance have exhibited a good agreement, except for an upper band widening not exceeding 5% of the higher cut-off frequency. This behavior might be related to the close proximity of the two connectors that are large if compared with the total dimension of the circuit. Each connector is 18.92 mm long whereas the total dimension of the board with connectors is 45.68 mm.

Another aspect might be an excessive sensitivity of this design methodology to the technology uncertainties, as elsewhere observed in the literature [5].

Others minor discrepancies might have been caused by specific tolerances of the mechanical plotter. The employed plotter has a x/y resolution of 0.25 μm and a z resolution of 0.5 μm.

In Fig. 3.13, the comparison between measured and EM simulated open-stub length versus frequency relationship is reported.

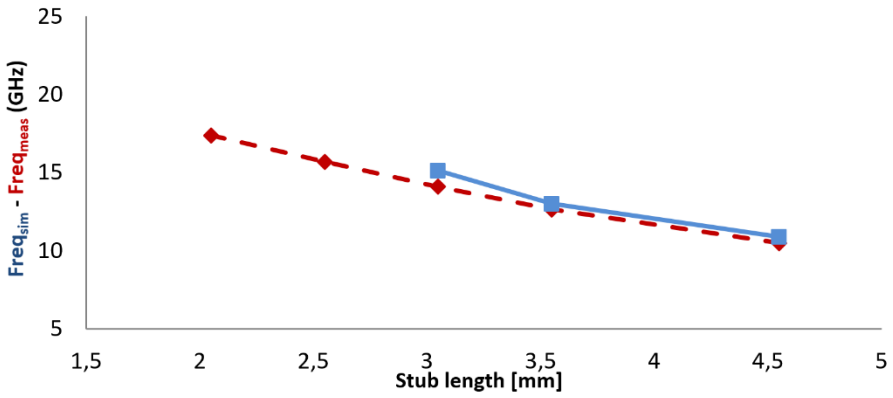

Fig. 3.13. Open-stub length vs frequency relationship: measured (line) and simulated (dashed) data [3].

3.3 References

[1] G. L. Matthaei, “Microwave Filters, Impedance-Matching Networks, and Coupling Structures,” Artech House, 1980.

[2] J. Hong, “Microstrip Filters for RF/Microwave Applications,” Wiley, Inc., 2011.

[3] A. Caddemi, and E. Cardillo, “A straight-line equation for the notch tailoring of a microwave extra wideband filter,” *Journal of Electromagnetic Waves and Applications*, Sept. 2016.

[4] H. Shaman, J.-S. Hong, “Ultra-Wideband (UWB) Bandpass Filter With Embedded Band Notch Structures,” *IEEE Microw. Wirel. Compon. Lett.,* Mar. 2007.

[5] J. B. M. Mokhtaari, J. Bornemann, “Microstrip Ultra-Wideband Filter with Flexible Notch Characteristics,” *Wirel. Engin. Tech.,* Jan. 2012.

[6] G.-M. Yang, R. Jin, C. Vittoria, V. G. Harris, N. X. Sun, “Small ultra-wideband (UWB) bandpass filter with notched band,” *IEEE Microw. Wirel. Comp. Lett.,* Mar. 2008.

[7] R. Gómez-García, A. C. Guyette, “Reconfigurable Multi-Band Microwave Filters,” *IEEE Trans. on Microw. Theory Tech.,* Apr. 2015

[8] A. Caddemi, E. Cardillo, and G. Tuccari, “Ultra Wide-Band HTS filter for new geodetic VLBI front-ends,” *European VLBI Group for Geodesy and Astronomy (EVGA),* Azores, Portugal, May 2015.

[9] J. Wang, J. Zhao, and J.-L. Li, "Compact Microstrip UWB Bandpass filter with triple-notched bands using parallel U-shaped defected microstrip structure," *Electronics Lett.*, Jan. 2013.

[10] W.-H. Tu, K. Chang, "Compact Second Harmonic-Suppressed Bandstop and Bandpass Filters Using Open Stubs," *IEEE Tran. on Microw. Theory Tech,* Jun. 2006.

[11] K. Song, Q. Xue, “Compact Ultra-Wideband (UWB) Bandpass Filters With Multiple Notched Bands,” *IEEE Microw. Wirel. Comp. Lett.,* Aug. 2010.

[12] V. Sekar, K. Entesari, "*Miniaturized UWB Bandpass Filters With Notch Using Slow-Wave CPW Multiple-Mode Resonators," IEEE Microw. Wirel. Comp. Lett.*, Feb. 2011.

[13] S. Pirani, J. Nourinia, C. Ghobadi, "Band-notched UWB BPF design using parasitic coupled line," *IEEE Microw. Wirel. Compon. Lett.*, Aug. 2010.

[14] W. J. Feng, W. Q. Che, Q. Xue, "Compact ultra-wideband bandpass filters with narrow notched bands based on a ring resonator," *IET Microw. Antennas Propag.*, Nov. 2013.

[15] D. M. Pozar, Microwave Engineering, Wiley, Inc., 1998.

[16] E. Cardillo, A. Caddemi, "Flexible CAD methodology for UWB filter with a tailored notch," *Proceedings of the IEEE Mediterranean Microwave Symposium (MMS)*, Lecce, Dec. 2015.

Conclusions

In the first Chapter of this thesis, the applications, technologies and circuital topologies for short-range radars have been studied and the technique for improving the digital signal processing has been presented. After the prototype realization allowed by internal laboratory facilities, the radar system has been tested for a special application in the field of assistive devices for visually impaired people.

Thereafter, the problem of noise in receivers has been considered and, an in-depth investigation on the noise in microwave transistors has been carried out. GaAs- and GaN- based devices have been characterized not only in standard conditions but also under the special condition of monochromatic light exposure. A microwave low-noise amplifier has been designed, realized and tested with the aim of exposing the active device to a laser beam to confirm the theoretical analysis performed. Its behavior has been analyzed under light exposure for different wavelengths and radiation power levels.

Finally, aspects related to filter in microwave receivers have been considered and a microwave filter with an extra wide bandwidth has been designed, realized and tested.

This thesis work has benefited from several scientific collaborations both with companies and research groups. The most relevant have been listed below:

- ✓ Infineon Technologies Italia S.r.l. (Ref. Dr. Laurita D'Ambrosio), Milano, Italy.
- ✓ Electromagnetism Research group (Ref. Prof. Graziano Cerri), Università Politecnica delle Marche, Ancona, Italy
- ✓ Istituto di Radioastronomia IRA INAF (Ref. Dr. Gino Tuccari), Noto, Italy
- ✓ Microwave Engineering Research group (Ref. Prof. Vera Markovic), Faculty of Electronic Engineering - University of Nîs, Serbia
- ✓ U.S. Naval Research Laboratory (Ref. Dr. Luciano Boglione), Washington D.C., USA.

Moreover, the contribution to two research studies in the field of the physical DC and microwave modeling of AlGaAs/GaAs HEMT (in collaboration with Dr. Nour El Islam Boukortt, Department of Electrical Engineering, University of Mostaganem, Algeria) and in the field of the optimum load search for achieving the linearity of E-band pHEMTs (in

collaboration with SIAE Microelettronica of Milan, Italy, Ref. Dr. Giuseppe Sivverini) has not been cited in the text.

I believe that the research activity depicted in Chapter 1 can be further extended by integrating all the radar sub-units over the same circuit board for being easy attachable to the handle of the white cane and to be tested on the field by visually impaired people. The experimental tests could also enlighten data processing features to be improved or changed.

With regard to research work concerning the analysis of the influence of UV light upon GaN HEMT's noise properties, due to the great scientific interest about this material, a more powerful light source is required for a better tracing of the effects. For this analysis, the availability of on wafer GaN LNA's at the ELEMIC laboratory would also allow a prompt comparison between expected behavior and tested performance.

Abbreviations and Symbols

(Citation order)

P_t	peak transmitted power
G_t	transmitting antenna gain
G_r	receiving antenna gain
λ	wavelength of a signal
σ	radar cross section of the target
R	distance from the radar to the target
L_s	sum of transmitting, atmospheric, receiving and signal processing losses
k	Boltzmann's constant
T_0	standard temperature
F	noise factor
B	bandwidth
RCS	radar cross section
IF	intermediate frequency
SNR	signal-to-noise ratio
MDS	minimum detectable signal
R_{max}	maximum detectable range
CW	continuous wave
f_d	Doppler frequency
v_r	velocity of target
R_{max}	maximum detectable range
τ	pulse width
EM	electromagnetic
PRI	pulse repetition interval
PRF	pulse repetition frequency
c	speed of light in vacuum
ΔT	time delay
δ_R	spatial resolution
CW	continuous wave

$FMCW$	frequency modulated continuous wave
ΔF	frequency bandwidth
T_m	modulation period
f_b	beat frequency
f_{bUP}	upsweep beat frequency
f_{bDWN}	downsweep beat frequency
RF	radio frequency
LNA	low-noise amplifier
LO	local oscillator
PDF	probability density function
P_{FA}	probability of false alarm
P_D	probability of detection
T_Λ	unknown threshold value
Λ	likelihood ratio
LRT	likelihood ratio test
$MMIC$	monolithic microwave integrated circuit
$HMIC$	hybrid microwave integrated circuit
FFT	fast Fourier transform
$Freq_m$	measured frequency
V_m	tuning voltage
V_{lin}	desired tuning voltage
ETA	electronic travel aids
MCU	microcontroller unit
TX	transmitted
RX	received
S_i	input available signal
N_i	input available noise power
N_o	output available noise power
S_o	output available signal
N_e	equivalent noise temperature
i_s	noise current due to noise source
e_n	voltage noise source

i_n	current noise source
Y_S	source admittance
i_{tot}	output noise current
F_{min}	minimum noise figure
R_n	noise resistance
Z_0	characteristic impedance
Γ_s	source reflection coefficient
Γ_{opt}	optimum noise reflection coefficient
$VSWR$	voltage standing wave ratio
NF_{min}	minimum noise figure expressed in dB
DUT	device under test
ENR	excess noise ratio
$P_{out,hot}$	output power in the hot state
$P_{out,cold}$	output power in the cold state
G_a	available gain
T_{hot}	temperature in the hot state
T_{cold}	temperature powers in the cold state
Y	Y factor
F_i	noise figure of the i-th stage
G_i	gain of the i-th stage
F_m	measured noise figure
$F_r(\Gamma_{out})$	noise figure of the receiver having at its input the reflection coefficient Γ_{out}
Γ_{out}	output reflection coefficient
Γ_{in}	input reflection coefficient
a_i	incident travelling voltage wave at port i (i = 1, 2)
b_i	reflected travelling voltage wave at port i (i = 1, 2)
S_{ij}	Scattering parameter matrix coefficients (i = 1, 2; j = 1, 2)
$HEMT$	high electron mobility transistor
$pHEMT$	pseudomorphic high electron mobility transistor
$MESFET$	metal–semiconductor field-effect transistor
2DEG	2-D electron gas

KGCR	K_g, K_r and K_c coefficients-based model
DC	direct current
AC	alternating current
i_g	gate noise current
i_d	drain noise current
ANN	artificial neural network
PNA	precision network analyzer
NFA	noise figure analyzer
K	Rollet's stability factor
$\tan\delta$	dissipation factor
ε_r	dielectric constant
h	dielectric thickness
t	conductor thickness
MSG	maximum stable gain
$E(\lambda)$	energy of a single photon at the optical wavelength λ
ε	filter ripple constant.
$F_n(\Omega)$	filtering or characteristics function
Ω	angular frequency
$L_A(\Omega)$	filter insertion loss
$L_R(\Omega)$	filter return loss
FBW	fractional bandwidth

List of publications

[1] A. Caddemi, E. Cardillo, and G. Crupi, "HEMT Sensitivity to Optical Radiation: Distinguishing Microwave Noise Aspect," accepted for publication and presentation as a keynote speaker in *The 12th International Symposium on SiO2 Advanced Dielectrics and Related Devices*, Jun. 2018

[2] E. Cardillo, V. Di Mattia, G. Manfredi, P. Russo, A. De Leo, A. Caddemi, and G. Cerri, "An electromagnetic sensor prototype to assist visually impaired and blind people in autonomous walking," *IEEE Sensors Journal*, Mar. 2018.

[3] A. Caddemi, E. Cardillo, and G. Crupi, "Light activation of noise at microwave frequencies: a study on scaled gallium arsenide HEMT's," *IET Circuits, Devices and Systems*, Nov. 2017.

[4] V. Đorđević, E. Cardillo, Z. Marinković, O. Pronić-Rančić, A. Caddemi, and V. Marković, "Wave Approach to Noise Modeling of Scaled On-Wafer GaAs HEMTs," *IEEE International Conference on Advanced Technologies, Systems and Services in Telecommunications (TELSIKS)*, Niš, Serbia, Oct. 2017.

[5] E. Cardillo, and A. Caddemi, "A novel approach for crosstalk minimization in FMCW radars," *Electronics Letters*, Vol. 53, Issue 20, pp. 1379-1381, Sept. 2017.

[6] A. Caddemi, and E. Cardillo, "Optical control of gain amplifiers at microwave frequencies," *Computing and Electromagnetics International Workshop (CEM)*, Barcelona, Spain, Jun. 2017.

[7] A. Caddemi, and E. Cardillo, "A study on dynamic threshold for the crosstalk reduction in frequency-modulated radars," *Computing and Electromagnetics International Workshop (CEM)*, Barcelona, Spain, Jun. 2017.

[8] A. Caddemi, E. Cardillo, G. Salvo, and S. Patanè, "Microwave effects of UV light exposure of a GaN HEMT: Measurements and model extraction," *Microelectronics Reliability*, Vol. 65, pp. 310-317, Oct. 2016.

[9] A. Caddemi, and E. Cardillo, "A straight-line equation for the notch tailoring of a microwave extra wideband filter," *Journal of Electromagnetic Waves and Applications*, Vol. 30, Issue 16, Nov. 2016.

[10] V. Di Mattia, A. Caddemi, E. Cardillo, G. Manfredi, A. De Leo, P. Russo, L. Scalise, and G. Cerri, "A Feasibility Study of a Compact Radar System for Autonomous Walking of Blind People," *2016 IEEE 2nd International Forum on Research and Technologies for Society and Industry Leveraging a better tomorrow* (RTSI), Bologna, Italy Sept. 2016, 3 p.

[11] A. Caddemi, E. Cardillo, and G. Crupi, "Comparative Analysis of Microwave Low-Noise Amplifiers under Laser Illumination," *Microwave and Optical Technology Letters*, Vol. 58, No. 10, Oct. 2016.

[12] N. Boukortt, B. Hadri, S. Patanè, A. Caddemi, G. Crupi, and E. Cardillo, "Electrical characteristic of SOI TG n-FinFET," *Materials for Advanced Metallization (MAM)*, Leuven, Belgium, Mar. 2016.

[13] A. Caddemi, E. Cardillo, and G. Crupi, "Microwave Noise Parameter Modeling of a GaAs HEMT under Optical Illumination," *Microwave and Optical Technology Letters*, Vol. 58, No. 1, Jan. 2016.

[14] E. Cardillo, and A. Caddemi, "Flexible CAD methodology for UWB filter with a tailored notch," *IEEE Mediterranean Microwave Symposium (MMS)*, Lecce, Italy, Dec. 2015.

[15] N. Boukortt, A. Caddemi, E. Cardillo, G. Crupi, B. Hadri, and S. Patanè, "Inverse Modeling of an AlGaAs/GaAs HEMT from DC and Microwave Measurements Illumination," *IEEE International Conference on Advanced Technologies, Systems and Services in Telecommunications (TELSIKS)*, Niš, Serbia, Oct. 2015.

[16] A. Caddemi, E. Cardillo, G. Crupi, and G. Salvo, "Performance Analysis of a Microwave Low-Noise Amplifier under Laser Illumination," *IEEE International Conference on Advanced Technologies, Systems and Services in Telecommunications (TELSIKS)*, Niš, Serbia, Oct. 2015.

[17] A. Meazza, G. Sivverini, A. Colzani, M. Fumagalli, A. Traversa, and E. Cardillo, "A New Methodology to Estimate E-band pHemt Linearity Optimum Load from Low Microwave Frequency Load Pull Measurements" *IEEE International Workshop on Integrated Nonlinear Microwave and Millimeter-wave Circuits (INMMiC)*, Taormina, Italy, 3 p., Oct. 2015.

[18] A. Caddemi, E. Cardillo, and G. Tuccari, "Ultra Wide-Band HTS filter for new geodetic VLBI front-ends," *European VLBI Group for Geodesy and Astronomy (EVGA)*, Azores, Portugal, 3 p. May 2015.

Publications under review

[19] A. Caddemi, and E. Cardillo, "A Systematic Experimental Analysis of an Optical Sensing Low-Noise Amplifier," submitted for publication in *IEEE Microwave and Wireless Components Letters*, Feb. 2018.

[20] V. Đorđević, E. Cardillo, Z. Marinković, O. Pronić-Rančić, A. Caddemi, and V. Marković, "Wave approach to the noise modeling of the GaAs HEMT under optical illumination," submitted for publication in *Electrical Engineering*, Feb. 2018.

[21] A. Caddemi, E. Cardillo, S. Patanè, and C. Triolo, "Low-noise amplifier under optical illumination: a complete experimental investigation of microwave and noise performance," submitted for publication in *IEEE Sensors Journal*, Jan. 2018.

[22] A. Caddemi, and E. Cardillo, "A Low-Cost Smart Microwave Radar for Short Range Measurements," submitted for publication in *Lecture Notes in Computer Science*, Nov. 2017.